New light on hidden surfaces

New light on hidden surfaces

PROEFSCHRIFT

DOOR

SYLVIE ROKE

GEBOREN TE DE BILT
IN 1977

Promotiecommissie

Promotor:	Prof. Dr. A. W. Kleyn
Co-promotor	Dr. M. Bonn
Referent	Prof. Dr. H. J. Bakker
Overige leden:	Prof. Dr. J. Reedijk
	Prof. Dr. J. W. M. Frenken
	Prof. Dr. G. J. Kroes
	Prof. Dr. A. van Blaaderen
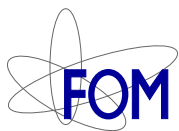
">...There is no problem known to science that cannot be cured by the liberal application of chocolate."

<div align="right">RICHARD BUTTERWORTH</div>

Contents

x

Chapter 1

Introduction

1.1   Surfaces

A surface is the end of a bulk. It is the membrane in a cell, the active area in a catalyst, the exterior of an ice particle in the stratosphere, the place where oxygen becomes part of the human body. It is at these places that proteins, enzymes and other active molecules are selectively permitted into the cell, reactions are accelerated, the place where ozone is destroyed and the blood cell takes up oxygen from the blood.

Surfaces or interfaces are also the place to find interesting and complex physics, because the endless repetition of atoms and molecules of the bulk comes to a halt and in some way makes the transition to another bulk medium. This asymmetry offers a great challenge to physicists in describing surface phenomena [1]. It is illustrative to quote the famous physicist Enrico Fermi (Nobel Prize 1938) who said: "God made the solid state. He left the surface to the Devil."

Important physical, chemical and biological processes occur at surfaces. Often these surfaces are hidden, because they are masked by the two bulk media that they separate [2]. The number of molecules residing on the surface of a (spherical) 1 ml drop of water is in the order of 10^{15}, whereas the bulk is composed of 10^{22} molecules. Since the importance of surface processes became clear in the early years of the 20th century, many techniques have been developed successfully to characterize and understand surface processes.

The exploration of solid-gas interfaces matured with the introduction of ultra high vacuum (UHV) in the 1960's, which made it possible to investigate atomically clean surfaces. The techniques used employ the interaction of ions, electrons and x-rays with surfaces [3, 4]. This research is mainly motivated by the development of heterogeneous catalysts, the understanding of surface processes in material sciences like corrosion and the construction of semiconductor devices.

To study buried interfaces one needs to make use of interactions that are not

hindered by the presence of intervening solids or liquids. One means is to distort the surface region and measure its reaction using either the restoring thermo-dynamic forces or the restoring proximal forces. Restoring thermodynamic forces generate a picture that reflects changes on a macroscopic scale and can be measu-red by, e.g., recording the surface tension. Proximal forces can be used to display the surface on a microscopic scale. This method is applied in, e.g., the atomic force microscope.

A different, non-invasive, approach is to probe the surface with photons. If these photons have the same energy as the energy difference between energy lev-els of the surface molecules one can obtain information on the molecular level. The vibrational modes of molecules are sensitive to the local environment. Prob-ing these modes with infrared photons thus generates a molecular picture of the molecule and its local surroundings. This type of spectroscopy is called vibrational
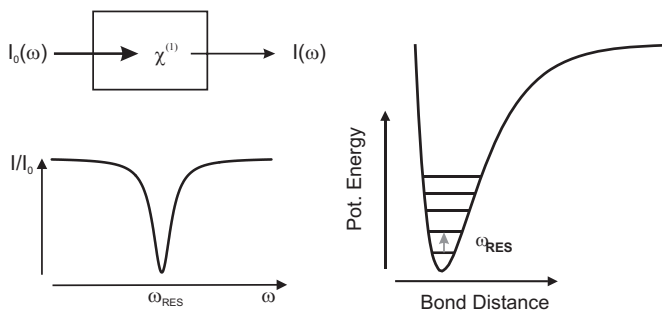
Figure 1.1: Schematic illustration of the optical processes involved in vibrational spectroscopy. It shows the potential energy surface of a vibrational mode with a number of possible energy states. The infrared light interacts resonantly with a vibrational mode. At parts of the spectrum where the frequency is resonant the light is absorbed. In the spectrum this appears as a dip.

spectroscopy and is illustrated in Fig. 1.1. The electromagnetic infrared field ($\mathbf{E}$) drives the oscillations in the molecules and creates a polarization ($\mathbf{P}$) that is given by:

$$\mathbf{P}(r,t) = \chi^{(1)}(r,t)\mathbf{E}(r,t). \tag{1.1}$$

The amount of polarization that is built up is determined by the first order sus-ceptibility ($\chi^{(1)}(r,t)$). If the infrared field becomes resonant with the vibrational mode, the first order susceptibility becomes large, resulting in a large polariza-tion. The polarization radiates an electric field that interferes destructively with

the incoming field. These destructive interferences show up as dips in the resulting intensity spectrum (see Fig. 1.1). As there is no specific surface sensitivity in the light-matter interactions other than the one imposed by the experimental geometry, both the bulk and the surface are measured simultaneously.

1.2 Second-order sum frequency generation

This lack of surface sensitivity can to a large extent [5] be overcome by the application of second-order vibrational sum frequency generation (SFG). In a second-order vibrational sum frequency experiment an infrared photon (with a wavelength of (e.g.) ~ 3333 nm=3000 cm^{-1}) and a visible photon (with a wavelength of (e.g.) ~ 800 nm=12500 cm^{-1}) interact with the molecules on the surface (see Fig. 1.2). The sum frequency polarization that is created due to interaction with
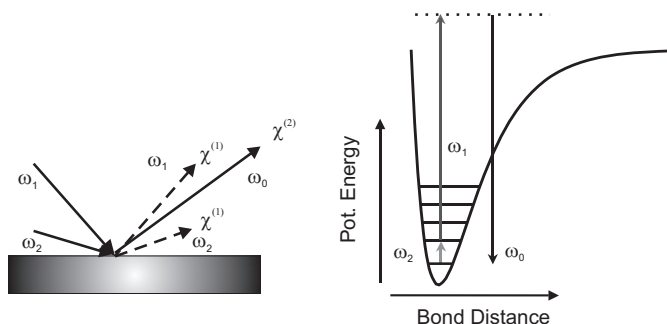
Figure 1.2: Schematic illustration of the optical processes involved in a sum frequency generation experiment on a flat surface. It shows the infrared (with frequency ω_2) and visible laser beams (with frequency ω_1) reflecting from the surface. This reflection is governed by the first order susceptibility. At the surface, a photon with the sum of the frequencies ($\omega_0 = \omega_1 + \omega_2$) is formed through nonlinear interaction (mediated by the second-order nonlinear susceptibility). The right panel illustrates the process of sum frequency generation on a molecular level. It shows a potential energy surface of a vibrational mode with a number of possible energy states. The infrared photon is resonant with the vibrational mode leading to an excitation of the molecular vibration. Non-resonant interaction with a visible photon leads to upconversion to a virtual, non-resonant state. Subsequently, the molecule returns to its ground state and emits a sum frequency photon.

fields $\mathbf{E}_1$ and $\mathbf{E}_2$ takes the form:

$$\mathbf{P}^{(2)}(r,t) = \chi^{(2)}(r,t) : \mathbf{E}_1(r,t)\mathbf{E}_2(r,t), \qquad (1.2)$$

where $\chi^{(2)}(r,t)$ is the second-order (sum frequency) susceptibility, which is a measure of how much nonlinear polarization is built up. The polarization radiates an electric field at the sum of the frequency of the incoming fields. This field is only large if the second-order susceptibility is large, which occurs only at those frequencies at which the infrared field becomes resonant with the vibrational modes, resulting in an upconverted vibrational spectrum. This results in a background free signal in the visible region (with the previously mentioned frequencies it becomes: 3000 cm^{-1}+12500 cm^{-1}=15500 cm^{-1} (=645 nm)).

Because $\chi^{(2)}(r,t)$ is a material property it reflects the intrinsic properties of the substrate under study. To illustrate the surface specificity of this technique, let us assume for a moment that the incident fields are (plane) cosine waves. If we now invert all the fields, $\mathbf{E}_1$, $\mathbf{E}_2$ and $\mathbf{P}^{(2)}$ must change sign. However if we are dealing with a material having inversion symmetry, $\chi^{(2)}$ does not change sign and we have:

$$-\mathbf{P}^{(2)}(r,t) = \chi^{(2)}(r,t) : \mathbf{E}_1(r,t)\mathbf{E}_2(r,t), \qquad (1.3)$$

Eqs. 1.2 and 1.3 can only be true simultaneously if $\chi^{(2)} = 0$. A surface does not possess inversion symmetry. This means that sum frequency generation is surface specific if it is applied to media with an intrinsic inversion symmetry (like most crystalline metals) or when there is averaged inversion symmetry on the time scale of the measurement (like bulk water at room temperature).

Fig. 1.2 shows a schematic illustration of second-order vibrational sum frequency generation in the most commonly employed reflection mode, displaying both the linear and second-order interactions that are mediated by respectively $\chi^{(1)}(r,t)$ and $\chi^{(2)}(r,t)$. The right panel shows the resonant interaction of an infrared photon with the molecular vibration and the subsequent upconversion by a visible pulse, resulting in an emitted sum frequency photon.

1.3   Femtosecond sum frequency generation

To be able to acquire a significant signal in a second-order vibrational sum frequency experiment, intense electric fields with sufficient spectral brightness are necessary. Hence, surface sum frequency experiments are performed with pulsed lasers. First setups were build in the late 1980's [6, 7, 8, 9] and early 1990's [10, 11, 12, 13, 14] using nanosecond and picosecond laser pulses. Later on with the introduction of titanium sapphire laser systems, pulses with a duration of typically one hundred femtoseconds (fs) could routinely be generated. As these femtosecond pulses have a short time duration their frequency content is broad (~200 cm^{-1}), allowing for the simultaneous sampling of all the vibrational modes
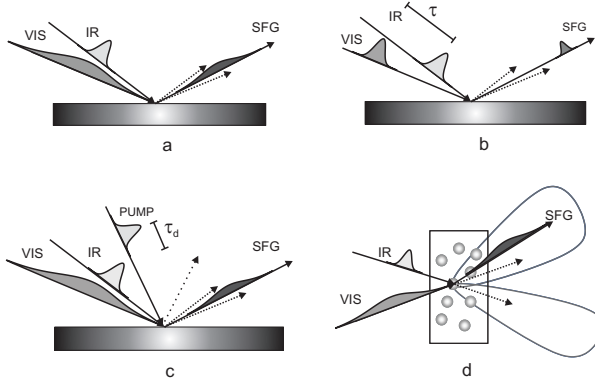
Figure 1.3: Illustration of the four modes of broadband vibrational sum frequency generation. The pulses represent the time domain envelopes. Schemes for: (a) frequency domain sum frequency generation, employing a temporally short infrared pulse and a temporally long visible pulse, (b) time domain sum frequency generation, with both pulses temporally short, (c) time resolved vibrational sum frequency generation, using the probe pair as in (a) in combination with a temporally short pump pulse, and (d) sum frequency generation scattering, using the probe pair as in (a) and detecting the inelastically scattered light.

present in the bandwidth of the pulse. This way of employing SFG is termed broadband sum frequency generation and it is the method used in this thesis.

Broadband vibrational sum frequency generation can be used as a surface probe in a few modes. The most widely applied mode is the frequency domain mode (Fig. 1.3(a)), in which the infrared pulse has a broad frequency content and the visible pulse a narrow one. Only the frequency components of the pulse that interact resonantly with the vibrational modes are enhanced and result in a sum frequency signal. Hence the spectral resolution is determined by the spectral width of the visible pulse. Using visible pulses with a narrow spectral bandwidth results in a high spectral resolution (but a low temporal resolution). In the time domain mode (Fig. 1.3(b)) both infrared and visible pulses have a short time duration, resulting in a low spectral resolution, but a high temporal resolution. The sum frequency intensity is recorded as a function of the delay time (τ) between the infrared and the visible pulse. These two modes will be discussed more thoroughly in Chapter 3. To obtain both spectral and temporal resolution it is possible to use sum frequency generation in a pump probe experiment (Fig. 1.3(c)). In this type of experiment the surface is distorted by a temporally short pump pulse and probed with sum frequency generation, at various time delays (τ_d). This will be discussed in more detail in Chapter 4. In the above described modes the sum frequency field needs to be reflected from a surface. This limits the use of sum

frequency generation to flat surfaces. In the fourth mode, newly developed in this thesis, this is not the case. In this mode the sum frequency field can be generated from surfaces of particles dispersed in a solvent and scattered off in various direction. The development and application of sum frequency scattering is the topic of Chapters 6-8.

1.4   This thesis

It is the goal of this thesis to shed some new light on a few selected hidden interfaces using femtosecond vibrational sum frequency generation. Along the way new aspects of the experimental technique and theoretical understanding are developed.

Chapter 2 will deal with the details of the experimental technique that are necessary to perform a femtosecond vibrational sum frequency experiment. In Chapter 3, time- and frequency domain sum frequency generation will be used to study the interaction of a liquid (acetonitrile) with a thin metal (gold) film. The influence of the metal surface on the vibrational dynamics will be investigated as well as the adsorption behavior of acetonitrile molecules. It is shown that although time- and frequency domain measurements are theoretically equivalent, the time domain experiments are more clearly influenced by the inhomogeneity of adsorption sites.

In Chapter 4, femtosecond time-resolved vibrational sum frequency generation will be examined as a probe to study surface dynamics. By modeling the SFG spectra as a function of visible pump-SFG probe delay time and taking the surface distortions into account, one finds that SFG spectra cannot be analyzed in the same way as linear vibrational spectra. The appearance of new spectral features does not necessarily point towards the appearance of new chemical species. Also, pump-SFG probe spectroscopy appears to be a suitable tool to observe transition states and to determine their lifetimes.

In Chapter 5, frequency domain sum frequency generation is used to investigate the phase behavior of phospholipid molecules on water. SFG is a sensitive tool to study order-disorder transitions on the molecular level. At high phospholipid densities there exists an ordered layer in which all the alkyl chains are fully stretched and oriented along the surface normal. At lower density there is a continuous order-disorder transition in the coexistence region of the liquid expanded and liquid condensed phase of the phospholipids. This transition can be modeled by calculating the density dependent SFG intensity. This model indicates that –on average– only four chain defects are sufficient to change the SFG signal dramatically. At very low densities all order is lost in a sudden phase transition in which the molecules form a novel, contracted phase.

In Chapter 6 the technique of sum frequency scattering is developed to study the molecular properties of the surface of sub-micron particles in suspension. By extending the late 19th century theory of Rayleigh and Debye for linear scatter-

ing, the scattering pattern can be described and the local molecular response can be extracted from the macroscopic nonlinearly scattered spectral intensity. These results demonstrate the use of vibrational sum frequency generation to investigate quantitatively the surface molecular properties of sub-micron particles of varying sizes, dispersed in solution.

Further drawing upon these results, in Chapter 7, a general theoretical method is presented to describe (non)linear optical scattering processes of arbitrary order using the reciprocity principle. By introducing an effective susceptibility that contains the properties of the scattering particles in combination with the experimental geometry, one can deduce selection rules independent of the precise mechanism of light-matter interaction. This approach is specified to second-order sum frequency scattering from an inhomogeneous medium. The limiting cases of small particle scattering, refractive index matched (Rayleigh-Gans-Debye) scattering, small refractive index contrast (Wentzel-Kramers-Brillouin) scattering and correlated scattering are considered.

Finally, in Chapter 8, sum frequency generation scattering is used to study the phase behavior of a colloidal dispersion at the molecular level. Here, the sensitivity of sum frequency generation to probe order/disorder transitions is utilized. The scattering theory of Chapter 6 and 7 is expanded to selectively monitor the order and orientation of the molecular stearyl ($C_{18}H_{37}$) groups that terminate the surfaces of the sub-micron sized silica colloids dispersed in hexadecane. In the highly viscous gel state, at low temperatures, the alkyl chains are very well ordered and oriented. In contrast, in the suspension at higher temperatures, the surface molecules are disordered. By simultaneously monitoring the SFG spectrum and the phase behavior (through turbidity and calorimetric measurements) of the colloidal dispersion with varying temperature direct evidence can be obtained that the surface-solvent interactions play a key role in the phase transition. Furthermore, the molecular nature of aging is investigated. It is observed that (slow) ordering of the alkyl chains occurs over time periods ranging from minutes to days.

The work described in this thesis is based on a number of scientific publications. A list can be found at the end of this thesis.

Chapter 2

Experimental

2.1   Introduction

To perform a broad band time-resolved vibrational sum frequency generation experiment one needs short pulses with high intensity in both the visible and infrared region. Such pulses –with a typical duration of 100 fs– can be produced using an amplified Ti:Sapphire oscillator that is pumped by a continuous wave laser. These pulses can be used both as the visible pulse in the sum frequency generation process and as the seed for producing infrared pulses. Below, a short outline of our laser system will be given (section 2.2). The next sections will be devoted to a short description of the physical processes involved in the generation of infrared laser pulses. Section 2.5 contains an outline of the sum frequency experiment.

2.2   The laser system

High intensity 800 nm pulses are created by amplifying the output of a Ti:Sapphire oscillator (Coherent, Mira 900-F). The oscillator is pumped by an 8 W CW Ar$^+$ laser (Coherent Innova 300) (Chaps. 3, 5) or a 6 W diode pumped CW solid state laser (Coherent Verdi V-6) (Chaps. 6, 7 and 8). The oscillator output consists of a 76 MHz pulse train, with a typical intensity pulse duration of ~ 115 fs. An example of the output spectrum is shown in Fig. 2.2.

To amplify the oscillator output the pulses are stretched in a single grating stretcher up to a few hundred ps and amplified in a 1 kHz regenerative amplifier (BMI alpha 1000-S). The amplifier is pumped by an intra cavity doubled 10 W Nd:Ylf laser, which delivers 280 ns pulses with a wavelength of 523 nm and a 1 kHz repetition rate. After amplification, the 800 nm pulses have a typical energy of 1.1 mJ and are compressed back to ~ 150 fs (intensity autocorrelate). This results in a system output of ~650 μJ visible pulses. Some 80 % of the output
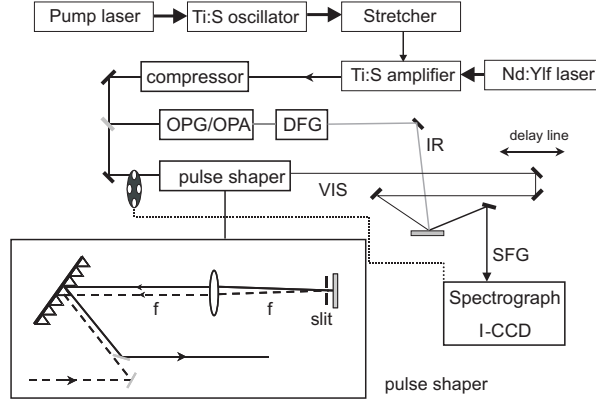
Figure 2.1: Illustration of the experimental setup, consisting of a schematic of the laser system, the pulse shaper and an example of the experimental geometry to obtain SFG in reflection mode. In the pulse shaper, the grating and the end mirror are both placed in the focal plane of the lens.

power is used to produce tunable IR pulses from 2 to 10 μm with a maximum pulse energy of 10 μJ. The remaining 20 % of the 800 nm pulse is used as the visible pulse in the sum frequency generation experiment.

2.3   Second-order processes

Second-order nonlinear optical processes are often used in the generation and amplification of new colors of light. As discussed in Chapter 1, the interaction of intense laser pulses with a surface or a bulk-medium with a nonlinear response can lead to the generation of a field with the sum of the input frequencies. In fact, the differences can also be generated and the total second-order polarization for the interaction of two plane wave fields with amplitudes $\mathcal{E}_i$, wave vector $\mathbf{k}_i$ and frequency ω_i, $E_i(t) = \mathcal{E}_i e^{i(\mathbf{k}_i \cdot \mathbf{r} - \omega_i t)} + c.c, i = 1, 2$ with $|\mathbf{k}_i| = \frac{n(\omega_i)\omega_i}{c} = \frac{\epsilon(\omega_i)^2 \omega_i}{c}$ is given by,

$$
\begin{aligned}
\mathbf{P}^{(2)}(\mathbf{r}, t) = \; & \chi^{(2)}[\mathcal{E}_1{}^2 e^{i2(\mathbf{k}_1 \cdot \mathbf{r} - \omega_1 t)} + \mathcal{E}_2{}^2 e^{2i(\mathbf{k}_2 \cdot \mathbf{r} - \omega_2 t)}] && \text{(SHG)} \\
+ \; & \chi^{(2)}[2\mathcal{E}_1 \mathcal{E}_2{}^* e^{i((\mathbf{k}_1 - \mathbf{k}_2) \cdot \mathbf{r} - (\omega_1 - \omega_2)t)}] && \text{(DFG)} \quad (2.1) \\
+ \; & \chi^{(2)}[2\mathcal{E}_1 \mathcal{E}_2 e^{i((\mathbf{k}_1 + \mathbf{k}_2) \cdot \mathbf{r} - (\omega_1 + \omega_2)t)}] && \text{(SFG)} \\
+ \; & 2\chi^{(2)}[\mathcal{E}_1 \mathcal{E}_1{}^* + \mathcal{E}_2 \mathcal{E}_2{}^*] && \text{(OR)},
\end{aligned}
$$

where $*$ refers to the complex conjugate (c.c). This means that in principle the sum (SFG) and difference (DFG) of all the input frequencies can be generated. If the sum of the same frequency is produced the nonlinear optical process is
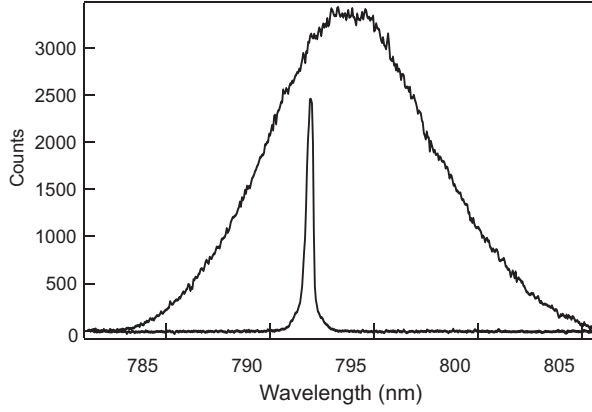
Figure 2.2: Typical spectrum of the oscillator output (FWHM: 9.5 nm (149 cm^{-1})) and a typical spectrum of a 2 μJ pulse-shaped visible pulse as used in frequency domain measurements (FWHM: 0.4 nm (6.5 cm^{-1})).

called second harmonic generation (SHG). If the difference of two fields with the same frequency (OR, optical rectification) is generated the process results in a strong DC field. Throughout this thesis the convention will be adopted that ω_0 denotes the highest frequency of the nonlinear optical process under study. Lower frequencies will be numbered in order of decreasing frequency.

As mentioned in Chapter 1 the magnitude of the generated fields is determined by the second-order susceptibility, which reflects the properties of the material. Also, the generated light is highly directional. This directionality is a consequence of the phase matching condition. It requires that light is only generated if momentum is conserved ($\Delta\mathbf{k} = 0$). For colinear beams it means that $\frac{n(\omega_0)\omega_0}{c} = \frac{n(\omega_1)\omega_1}{c} + \frac{n(\omega_2)\omega_2}{c}$ must hold, which simply states that the phase velocity of the sum of the two incoming beams must be identical to the phase velocity of the light that is generated. (If this is not the case there will be no constructive interference.) For all processes the conservation of energy must hold as well. In difference frequency generation ($\omega_3 = \omega_1 - \omega_2$ with $\omega_1 > \omega_2$) this means that for every photon that is created at frequency ω_3 one at frequency ω_1 is destroyed and one at ω_2 is created. Effectively, the field at frequency ω_2 is amplified. This is also known as optical parametric amplification (OPA).

In most materials the refractive index increases with frequency and the phase matching condition is not fulfilled. However, In certain types of crystals, known as birefringent crystals, phase matching can be achieved by changing the polarization direction of the interacting waves [15, 16]. Also, by tuning the angle of the crystal with respect to the propagation direction of the incoming light the refractive index can be chosen such that only certain frequencies can be generated. By scanning this angle it is possible to selectively tune the generated light over a

wide range of frequencies.

2.4 Generating infrared pulses

To generate infrared pulses with a high energy a widely used approach is to apply optical parametric generation (OPG)/amplification (OPA) of near-infrared pulses followed by difference frequency generation. In the first step of this process the 800 nm beam is used as a seed in optical parametric generation or optical parametric super-fluorescence in a β-BBO$_3$ crystal. The result is a broad spectrum with low intensity. Optical parametric generation is only possible at high pulse energy, because it is the noise photons, or vacuum fluctuations, that are amplified [16]. The origin of optical parametric generation lies in the quantum mechanical nature of the process and is beyond the scope of this concise description. The optical parametric generation is followed by optical parametric amplification (using the 800 nm beam as the second frequency) of a selected range of frequencies from the broad spectrum generated in the first step. The range of frequencies is chosen by angle tuning the β-BBO$_3$ crystal. In our system we use a commercial device to generate infrared pulses (TOPAS, Light Conversion Inc.) and from the OPG/OPA process we have access to pulses with a wavelength range of 1-2.6 μm. The infrared pulses are produced by non-colinear difference frequency mixing of the near-infrared pulses in a AgGaS$_2$ crystal, resulting in infrared pulses with a wavelength range of 2.6-10 μm. The peak output power is ∼ 10 μJ achieved at a wavelength of ∼ 3 μm with a 500 μJ 800 nm input. Conversion efficiency of the 800 nm in the OPG/OPA stage is approximately 30 %.

Fig. 2.3 shows a typical infrared spectrum of the TOPAS output focused into a spectrograph with a 150 grooves/mm infrared grating and collected with a liquid nitrogen cooled MCT detector.

2.5 The sum frequency experiment

The sum frequency experiments were performed in either a time domain (TD) or a frequency domain (FD) mode (as illustrated in Figs. 1.3 and 3.1). In the time domain mode, both the infrared and visible pulses have a short time duration on the order of 100 fs and as a consequence a high time resolution can be achieved that allows one to observe the vibrational dynamics at the interface, which usually occurs on the time scale of a few picoseconds. The time resolution is determined by the intensity cross-correlate of the incoming fields:

$$I_0(\tau) = \int_{-\infty}^{\infty} I_1(t - \tau)I_2(t)dt. \tag{2.2}$$

In the frequency domain mode the spectrum of the visible pulse is modified with a pulse shaper, such that its frequency content becomes narrow. The pulse shaper
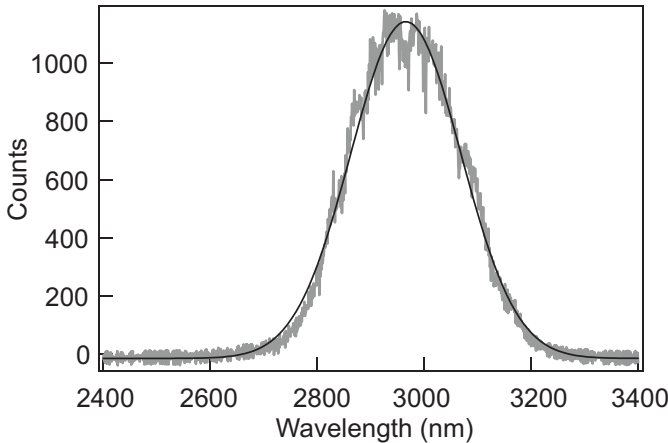
Figure 2.3: Typical infrared spectrum of the TOPAS output centered around 3000 nm. The black line is a Gaussian fit with a FWHM of 243 nm.

consists of a grating (Spectrogon, high intensity 1200 gr/mm blazed at 800 nm) which spatially disperses the 800 nm pulse. The first order reflection is collimated by a lens, which is placed such that the beam path is slightly below its center. The light reflects onto a mirror, placed in the focal plane of the lens and is sent back through the lens onto the grating, from where it is reflected back slightly higher than the original incoming beam (see Fig. 2.1). By placing a slit in front of the reflecting mirror the spectral content of the pulse can be controlled (see Fig. 2.2 for a typical example of a shaped spectrum). Without the slit the original pulses are recovered for time domain measurements.

In an SFG experiment the frequency width of the measured signal is determined by the spectral width of the response of the molecule/surface system in combination with the spectral width of the visible pulse. For experiments in which the (frequency) width of the response (represented by $\mathrm{chi}^{(2)}$) is much larger than the line width of the visible pulse the latter can be neglected. In general the frequency response is given by a convolution of the susceptibility with the visible field:

$$I_0(\omega) \propto |\sum_n \int_{-\infty}^{\infty} \chi_n^{(2)}(\omega')E_1(\omega'-\omega)d\omega'|^2. \qquad (2.3)$$

The sum frequency light is focused onto the entrance slit of a spectrograph (Acton, having 3 different gratings with 150, 1200, 1800 gr/mm) and dispersed onto an intensified, gated Charge Coupled Device (CCD) detector. In such a device the photons are converted to electrons on a photocathode (type Gen IV, 500-900 nm, QE 45 %, GaAs), multiplied in a multi-channel plate (MCP) and regenerated on a phosphor screen (the intensifier). The intensified photons are coupled onto a

CCD chip. On the chip the photons generate electrons as long as their energy is larger than the band gap of Si. These free electrons are captured and counted. The camera is gated by switching the voltage on the photocathode. If it is more negative (positive) than that on the MCP (no) electrons are generated. The gate of the camera has a duration of ~ 40 ns and is phase locked with respect to the visible pulse. The spectral resolution of the spectrometer camera system is 1.4 cm^{-1} .

Chapter 3

Time vs. frequency domain sum frequency generation

We present a study of the C-H and C-N vibrational modes of acetonitrile molecules at the interface between bulk liquid and a gold film using both time- and frequency-domain femtosecond sum frequency generation. Acetonitrile is adsorbed on the gold surface with the N atom towards the interface. Due to the surface roughness there are different adsorption sites, leading to an inhomogeneous distribution of vibrational frequencies of the C-N stretch vibration of different molecules. This is observed most clearly in the time-domain SFG measurements, while the frequency-domain measurements are much less sensitive to the inhomogeneity. In contrast to the C-N stretch mode, the C-H stretching modes are unaffected by the surface and display homogeneous line broadening.

3.1   Introduction

Interfaces and surfaces play an important role in many chemical and physical processes occurring, for example, in heterogeneous catalysis and electrochemistry [4, 17, 18]. In many of these processes, the vibrational degrees of freedom of the molecules involved play a key role. The study of vibrational dynamics of molecules at surfaces requires a technique that specifically probes vibrations of molecules at the interface, with sufficient time resolution to resolve the dynamics (occurring typically on a sub-picosecond time scale). As a second-order nonlinear optical tool, femtosecond vibrational Sum Frequency Generation (SFG) is ideally suited for this purpose [16].

In a vibrational SFG experiment an interface is probed by simultaneous (nonlinear) interaction of an infrared (IR) and a visible (VIS) photon with the surface region. This results in the generation of a third photon, with the sum of the two frequencies (as described in Chapter 1). When the infrared field is resonant with a vibrational mode of a molecule at the surface a resonant infrared polarization ($\mathbf{P}_{IR}$) is created, with a magnitude determined by the transition dipole moment ($\overset{\leftrightarrow}{\mu}$) and the infrared field. The infrared polarization decays exponentially (and is called the Free Induction Decay, (FID)) and is upconverted by the visible field. The resulting sum frequency field is resonantly enhanced and contains information about the surface molecular vibrations.

In the experiments described in this Chapter, we have used two different ways of performing SFG using femtosecond pulses, one to obtain time resolution and one to obtain frequency resolution. The first is performed using temporally short infrared and visible pulses ($\sim$100 fs). By delaying the pulses with respect to each other (see Fig. 3.1), the temporal decay of the resonant vibrational polarization can be followed in real-time. The decay occurs typically on a $\sim$1 ps time scale. Although very high time resolution can be obtained in this approach, no frequency resolution can be achieved because both pulses have a broad frequency content. The second way – with very good frequency resolution – relies on combining a short infrared pulse with a long visible pulse (with a narrow frequency spectrum). As a consequence, the frequency distribution of the vibrationally enhanced SFG light is determined by the vibrational distribution, so that high frequency resolution is achieved. These two complementary approaches allow us to obtain information about the binding site (through the resonance frequency) and follow the vibrational dynamics of the polarization in real time.

In this Chapter, we use time and frequency domain sum frequency generation to study acetonitrile (CH_3CN) molecules from the liquid phase adsorbed on a very thin gold film. We show that although both time- and frequency domain measurements are theoretically equivalent, the time domain experiments are more clearly influenced by the inhomogeneity of adsorption sites, since the decay of the vibrational polarization can be mapped directly. We start (in section 3.2) with a theoretical background necessary to model time and frequency domain sum fre-
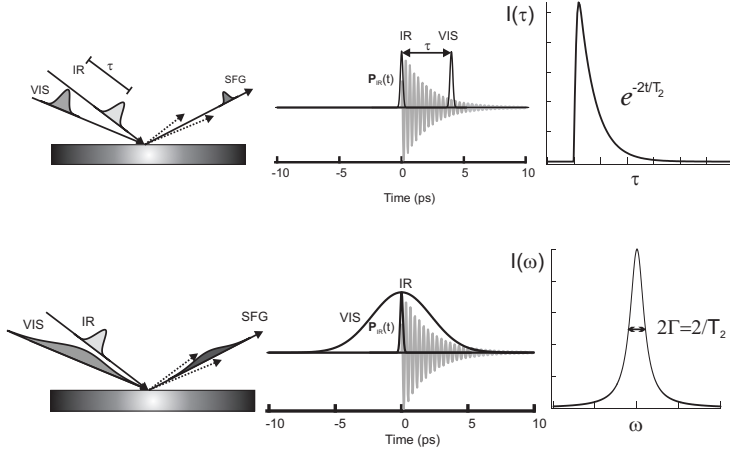
Figure 3.1: Schematic illustration of a time-domain (top) and a frequency-domain (bottom) SFG experiment. In the time domain experiment, short pulses are employed, delayed by τ and the frequency-integrated SFG signal is recorded as a function of delay time between the infrared and visible pulses. In a frequency domain experiment, temporally long (spectrally narrow) visible pulses are used to upconvert the infrared-induced polarization at the surface and the time integrated signal is recorded as a function of frequency. The pictures in the middle panel illustrate the sequence of events in the time domain, showing the induced infrared polarization ($\mathbf{P}_{IR}(t)$) that decays with a time constant T_2 and is upconverted by the visible pulse. The right panel displays the measured intensity in both scenarios.

quency generation. From analysis of the vibrational CH_3 (in section 3.4) and C-N stretch modes (in section 3.5) we find that the surface roughness initiates inhomogeneity in the vibrational C-N stretch mode, which is found to be closest to the surface. A generalization of the existing models allows for the simultaneous description of both frequency and time-domain measurements.

3.2 Theoretical background

In a broad-band SFG experiment a broad-band femtosecond infrared pulse ($\mathbf{E}_2$, containing frequencies ω_2) interacts resonantly with a vibrational mode of the adsorbed molecules. This induces a vibrational polarization ($\mathbf{P}_{IR}$) at the interface, which subsequently decays with a typical time constant T_2, the dephasing time. This infrared polarization is upconverted by the visible field (containing frequencies ω_1) to create a second-order nonlinear polarization $\mathbf{P}^{(2)}$ that oscillates at the sum frequency ($\omega_0 = \omega_1 + \omega_2$). The emitted electric field can be calculated

by solving the Maxwell equations using $\mathbf{P}^{(2)}$ as a source term.

In a time domain experiment both IR and VIS pulses are short ($\sim$100 fs) and the SFG intensity (I_0) is recorded as a function of delay time (τ) between the two pulses (see the illustration in fig. 3.1). The intensity is given by the following expression:

$$I_0(\tau) \propto \int_{-\infty}^{\infty} dt \left| \mathbf{P}^{(2)}(t,\tau) \right|^2 = \int_{-\infty}^{\infty} dt \left| \mathbf{P}_{RES}^{(2)}(t,\tau) + \mathbf{P}_{NR}^{(2)}(t,\tau) \right|^2, \qquad (3.1)$$

in which the second-order nonlinear polarization, $\mathbf{P}^{(2)}$, consists of the resonant response of the molecules, $\mathbf{P}_{RES}^{(2)}$, and the non-resonant response of the metal, $\mathbf{P}_{NR}^{(2)}$. The second-order nonlinear polarization for a single resonance and a given polarization combination of fields can be written as follows [13]:

$$P^{(2)}(t,\tau) = \overline{E}_1(t-\tau)\{\int_{-\infty}^{t} A_{RES}\overline{E}_2(t')\chi_{RES}^{(2)}(t-t')dt' + A_{NR}\overline{E}_2(t)e^{i\phi}\}e^{i(\omega_1+\omega_2)t},$$
$$(3.2)$$

where $\overline{E}_1$ and $\overline{E}_2$ are the envelopes of the visible and infrared fields. The first term of $P^{(2)}(t,\tau)$ describes the resonant response (with amplitude A_{RES}) of the adsorbate to the IR field. Integration in Eq. (3.2) over the dummy variable t' is necessary to incorporate the non-instantaneous response of the molecules to the incoming IR field. The second term in Eq. (3.2) describes the non-resonant (instantaneous) contribution from the metal with amplitude A_{NR}. The value of A_{RES} is determined by the magnitude of the infrared transition dipole moment and the Raman polarizability and A_{NR} is governed by the magnitude of the non-resonant hyperpolarizability. ϕ is the phase difference between the resonant and the non-resonant field and is modeled as a constant [19, 20]. $\chi_{RES}^{(2)}(t)$ is usually [8, 9, 21] modeled as:

$$\chi_{RES}^{(2)}(t) = e^{-t/T_2} e^{i\omega_{0n}} \qquad (3.3)$$

where ω_{0n} is the resonance frequency and T_2 is the dephasing time corresponding to vibrational mode n. This implies that all the molecules in the ensemble momentarily behave as one and oscillate in phase at frequency ω_{0n}, until they decay. Such a distribution is called an homogeneous distribution [22]. Until now, the above description has proven sufficient to model the SFG spectra for an ensemble of molecules on a metal surface.

In a frequency domain experiment the IR polarization is the same as for a time domain experiment, but the upconversion occurs with a temporally long (and spectrally narrow) visible pulse to achieve high frequency resolution [23, 24]. The measurement is performed in the frequency domain and the SFG intensity is more conveniently expressed in terms of the frequency domain polarization. The latter is simply the Fourier transform of the time domain second-order nonlinear polarization. Thus, time and frequency domain SFG experiments are in theory equivalent. This leads to the following equation to model frequency domain SFG

measurements:

$$I_0(\omega) \propto \left| \frac{1}{\sqrt{2\pi}} \int_{-\infty}^{\infty} dt\, e^{i\omega t} P^{(2)}(t, \tau = 0) \right|^2 = \left| P^{(2)}(\omega) \right|^2 \qquad (3.4)$$

with $P^{(2)}(t, \tau = 0)$ given by Eq. (3.1). Assuming a δ-function distribution (in the time domain) for the IR field, we have for the polarization [13]:

$$P^{(2)}(\omega) = \chi^{(2)}(\omega) E_1(\omega) E_2(\omega) \qquad \text{with} \qquad (3.5)$$

$$\chi^{(2)}(\omega) = A_{RES} \chi_{RES}^{(2)}(\omega) + A_{NR} \chi_{NR}^{(2)}(\omega) = \frac{A_{RES}}{(\omega - \omega_{0n}) + i\Gamma} + A_{NR} e^{i\phi}$$

where $\Gamma = 1/T_2$. For a zero non-resonant contribution this results in a Lorentzian line shape with a FWHM of 2Γ (see Fig. 3.1). However, if there is both a resonant and a non-resonant contribution to the signal the line shape becomes distorted and critically depends on the phase factor ϕ. This can result in a large variety of line shapes (see e.g. [19]).

   If the duration of the visible pulse is comparable to or shorter than the decay time of the polarization (i.e. the line widths of the visible pulse and the resonant intensity are comparable), the spectral lines can appear broader than the actual vibrational resonance [19, 25]. To account for this, the second-order nonlinear susceptibility may be convoluted with the visible field.

3.3   Experimental

The SFG experiments are performed using 120 fs FWHM Gaussian pulse duration infrared pulses (10 μJ energy FWHM spectral bandwidth of 220 cm^{-1}) centered at 2940 cm^{-1} and 2250 cm^{-1} for investigating the C–H and C–N stretch mode of acetonitrile, respectively. The temporal and spectral profile of the 800 nm visible pulse (2.3 μJ, repetition rate reduced from 1 kHz to 83 Hz) was varied using a pulse-shaper: frequency domain-SFG spectra are recorded with a 3 cm^{-1} FWHM bandwidth (>10 ps auto-correlate width) upconversion pulse and time domain-FID's are measured with 120 fs visible pulses. As discussed in Chapter 2, switching from time domain to frequency domain measurements only requires the insertion of a slit in the pulse-shaper, leaving the alignment unchanged. For a meaningful comparison, we have used identical energies of the visible pulse in the frequency domain and time domain experiments. Note that it is straightforward to increase the signal in the time-domain measurement, by increasing the pulse energy. In the frequency domain measurement, increasing the pulse energy cannot be done without sacrificing spectral resolution, for our type of experimental set-up. The measurements were done in a co-propagating total internal reflection geometry (after [20, 26]) in which the reflected SFG field is detected (see Fig. 3.2). In this geometry, consisting of a rough metal surface on top of a dielectric prism, the fields at the interface become enhanced, leading to a large SFG signal [19, 26].

The p-polarized IR and VIS pulses are incident under angles of 57° and 61° with respect to the surface normal, respectively. Infrared spectra of liquid acetonitrile (spectroscopic grade) are taken (at 2 cm^{-1} resolution) with a Biorad FTS 175 FTIR spectrometer.
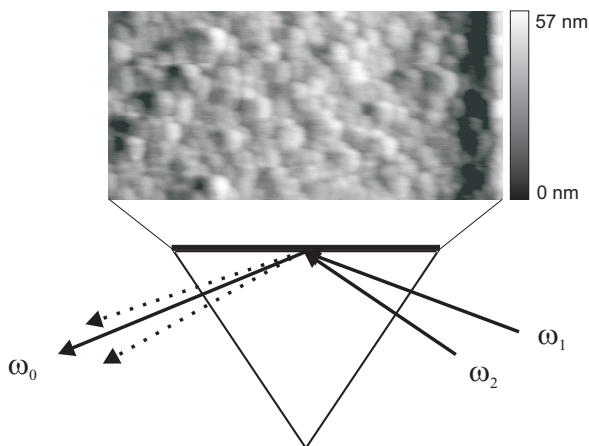
Figure 3.2: Schematic illustration of the co-propagating optical geometry with an AFM picture (400 nm x 200 nm) of a 3 nm thick gold film on the back of the CaF$_2$ prism. The r.m.s. roughness is 6.6 nm.

Gold films of ~3 nm thickness are prepared by evaporating gold from a filament on the back of a 60° CaF$_2$ prism. This produces films with a roughness determined by the substrate. Fig. 3.2 shows an AFM picture of a freshly evaporated 3 nm thick gold film on the back of a CaF$_2$ prism. This picture clearly shows the roughness of the gold surface. By reducing the repetition rate (with a phase-locked optical chopper) to 83 Hz, the heat load was kept sufficiently low in order to avoid damage. The absorbed fluence was kept well below the ablation threshold (~1.7 mJ/cm^2, as determined both experimentally and from a two temperature model calculation see e.g. [27]). Prior to each measurement the signal of the non-resonant CaF$_2$/gold/air interface was checked to make sure that the layer was not damaged. The signal of a purposely damaged gold layer is dramatically (more than 2 orders of magnitude) lower. Thus it was ensured that the experiments presented here were performed on intact gold layers. The morphology of our gold surface closely resembles that used by Williams *et al.* [20] in their SFG study of adsorbates on gold. They were not able to perform total internal reflection measurements on layers with a thickness less than 5 nm, due to single-pulse damage. It is possible in our experiments to use films as thin as 3 nm, however, because our visible pulses are appreciably shorter than 4 ns. These short pulses can deliver high intensities in combination with a relatively small heat load.

3.4   Homogeneous broadening

Fig. 3.3 depicts frequency domain SFG spectra in the C-H stretch region of ace-
tonitrile, for the bare gold surface and for the surface in contact with acetonitrile.
Two resonant features can be observed for the latter, one at 2939 cm^{-1} corre-
sponding to the symmetric stretch vibration and a weak, but clearly visible, fea-
ture at 3000 cm^{-1}, which can be attributed to the antisymmetric stretch vibration.
The fit in the frequency domain data in Fig. 3.3 is obtained by employing Eqs. 3.4
and 3.5 using the non-resonant contribution from the gold/air SFG spectrum and
results in a dephasing time of of 0.66 ps (Γ=8.0 $\pm$ 0.2 cm^{-1}) for the symmetric
stretch vibration and a dephasing time of 0.30 ps (Γ=18 $\pm$ 0.7 cm^{-1}) for the an-
tisymmetric stretch vibration. Such a fast dephasing of the C-H symmetric stretch
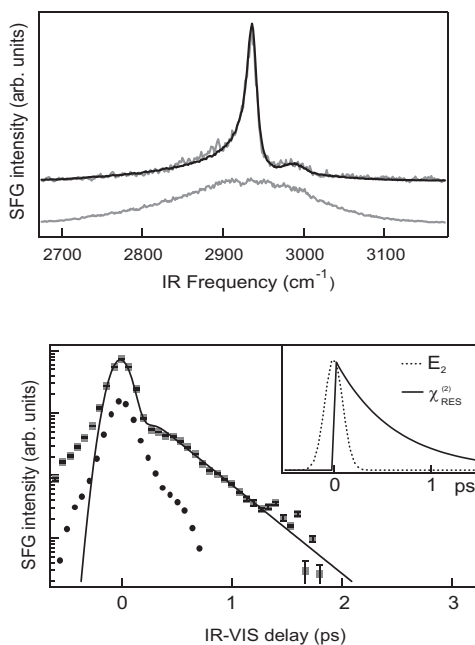
Figure 3.3: Top panel: SFG spectra in the C–H stretch region of a gold film in
contact with acetonitrile. The dashed line is a fit using Eqs. 3.4 and 3.5. The
gold/air SFG spectrum is also shown. Bottom panel: Free induction decay (on a
log-normal scale) of the C-H stretch vibration. A cross-correlate generated at the
gold/air interface is also shown. The solid line is a fit using Eqs. 3.1-3.3 (assum-
ing a single resonance frequency for the entire ensemble). The inset shows the
functional form of the IR field envelope in combination with the envelope of the
resonant second-order susceptibility used in the fit procedure.

is comparable to the dephasing time of the same mode in other systems, like a

self assembled monolayer of ferric stearate on CaF_2 (0.59 ps) [28], acetonitrile on YAG (0.42 ps) [29] or acetonitrile on ZrO_2 [26] (Γ= 5.7 cm^{-1}, corresponding to T_2=0.93 ps). The bottom panel of Fig. 3.3 shows the time domain SFG measurements (the Free Induction Decay (FID)) of the symmetric C-H stretch vibration. Also shown is a measurement of the gold/air interface, which is the cross-correlate of the IR and VIS pulses. It allows for the determination of the time resolution in the measurements (FWHM: 220 fs). From the linear decay on the log-normal scale, it is clear that the vibrational polarization of the C-H stretch mode decays exponentially. Thus, the C-H stretch mode is homogeneously broadened. The fit was obtained using Eqs. 3.1, 3.2 and 3.3 with a dephasing time of 0.61 ps. This value compares favorably to the value of 0.66 ps deduced from frequency domain data. It shows that both time and frequency domain data are in good correspondence with each other. This is required, since in both schemes the polarization decay is detected. (Note that the relative phase ϕ can be different however, as the visible pulse passes through some filters in the time domain experiments to achieve an equivalent pulse energy.) A clear difference in the time and frequency domain data is the way in which the interference of the resonant and non-resonant contribution manifests itself. As can be seen from Fig. 3.3 in the frequency domain data the whole spectral region is affected, whereas in the time domain measurement interference occurs over a limited time only.

In the time domain experiments, super-imposed on the exponential decay, small oscillations in the amplitude can be observed. The period of these oscillations is 500 ± 50 fs, which corresponds to a frequency difference of 64 ± 6 cm^{-1}. These oscillations can be attributed to interference between the vibrational coherence of the symmetric C-H stretch mode and the vibrational coherence of the antisymmetric stretch vibration (the difference in frequency is 61 cm^{-1}, see Fig. 3.3) in agreement with previous observations [28].

The shape of the frequency domain spectrum shows that the resonant and non-resonant sum frequency fields are comparable in size and that interference seems to be constructive. In other studies, in particular experimental [30] and theoretical [31] sum- and difference frequency generation studies of CN$^-$ ions adsorbed on a gold electrode, it was observed that the non-resonant signal is much larger than the resonant signal and that interference is destructive for SFG measurements (causing the signal to appear as a dip) and constructive for DFG measurements (causing the signal to appear as a positive peak). This discrepancy can be explained by noting that in our case both resonant and non-resonant signal are of comparable size. An apparent constructive interference might also be a destructive one in which the magnitude of the resonant signal is larger than the non-resonant one. The reason for such a small non-resonant signal lies in the fact that the non-resonant signal from the gold film has its origin in two types of source currents: a surface current that is generated in the first few Ångstroms of the film and a bulk current that extends into the metal for approximately one optical skin depth (~10 nm) [32, 33]. In our case the film thickness is well below the skin depth, so that the second current source contributes only slightly to the

emitted non-resonant SFG field.

3.5 Inhomogeneous broadening

In the previous section we have established that for the methyl (CH_3) stretch vibration of acetonitrile the SFG formalism as outlined in section 3.2 works well and that there is a homogeneous distribution of resonance frequencies. Very contrasting behavior is observed for the C–N stretch vibration of acetonitrile on gold.
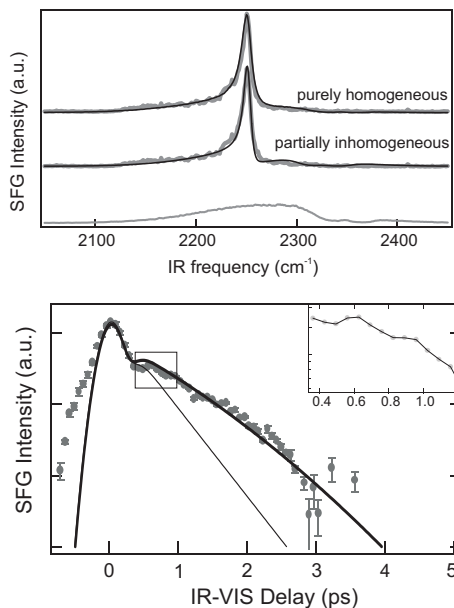
Figure 3.4: Top panel: SFG spectra in the C–N stretch region of a gold film in contact with acetonitrile. The fit in the upper trace is a fit using Eqs. 3.4 and 3.5. The fit in the middle trace incorporates inhomogeneous broadening and is described in the text. The gold/CaF_2/air spectrum is also shown, in which the degenerate antisymmetric stretch vibration of CO_2 appears clearly. Bottom panel: Free induction decay (on a log scale) of the C–N stretch vibration on a log scale. The solid lines are calculations assuming homogeneous (decaying exponentially) and partial inhomogeneous broadening (the fit through the data) using the same parameters as in the top panel. The inset shows the oscillations in the free induction decay (obtained by subtracting a fit) in the region highlighted by the box.

Fig. 3.4 shows both the SFG spectrum (top panel) and the FID (bottom panel) of the CN stretch vibration. The SFG spectrum shows one vibrational resonance

at 2250 cm^{-1}, which corresponds to the C-N stretch vibration. The non-resonant gold/air spectrum is also shown. It shows two absorption lines that are caused by absorption of IR by CO_2 present in ambient air.

The free induction decay of the C-N stretch mode displays oscillations at small delay times (between 0 and 1 ps, see the inset in the lower panel). These weak oscillations have a period of ~ 320 fs corresponding to a frequency difference of 104 cm^{-1}. A frequency difference of 104 cm^{-1} with respect to the C-N resonance frequency does not correspond to any known vibrational resonance of acetonitrile. It does correspond however, to the difference between the frequency of the C-N stretch vibration and the frequency of the antisymmetric degenerate CO_2 stretch vibration. As part of the IR field is resonant with the antisymmetric degenerate CO_2 stretch vibration, it sets up an IR polarization in air (before arriving at the sample) that radiates an IR electromagnetic field and interferes with the original field which then becomes slightly modulated, resulting in modulations of the non-resonant SFG field. Between approximately 0 and 1 ps there is significant interference between the resonant and non-resonant sum frequency field and hence oscillations will appear in the signal (without affecting the overall decay of the resonant contribution).

The frequency domain spectrum can be reproduced very well with Eqs. 3.4 and 3.5, using $\omega_{0n} = 2250$ cm^{-1} and $\Gamma = 7.6$ cm^{-1} ($T_2 = 0.68$ ps). As mentioned in section 3.2, both the SFG spectrum and the FID are a measurement of the same polarization, so that the FID should be described with the time domain equivalent (Fourier transform) of the frequency domain response. However, an exponentially decaying $\chi_{RES}^{(2)}(t)$ with $T_2 = 0.68$ ps (the exponentially FID, shown in the lower panel of Fig. 3.4) clearly does not describe the measured FID. Inversely, an exponential fit to the time domain measurement results in a frequency domain FWHM linewidth of 6.6 cm^{-1}, which is significantly too narrow. Apparently, obtaining a good fit with the commonly employed Eq. 3.3 is not a guarantee for homogeneous dephasing behavior.

The clearly non-exponential decay of the FID seems to suggest a partially inhomogeneous scenario, in which the resonance frequency is not the same for all molecules but varies with the adsorption site. Following Refs. [11, 34, 35], such a partially inhomogeneous distribution of adsorption sites can be characterized by a Gaussian distribution, $g(\omega_{0n}')$, of resonance frequencies (ω_{0n}') centered around ω_{inh} with a width $\Delta\omega$, i.e. $g(\omega_{0n}') = \frac{2}{\Delta\omega\sqrt{\pi}} e^{-\frac{(\omega_{0n}' - \omega_{inh})^2}{(\Delta\omega)^2}}$. The time domain resonant response can then be written as:

$$\chi_{RES}^{(2)}(t) = \sum_{\omega_{0n}'} \chi_{RES}^{(2)}(t, \omega_{0n}') = \int_0^\infty d\omega_{0n}' g(\omega_{0n}') e^{-t/T_2} e^{i(\omega_{0n}' + \omega_1)t}$$
$$\equiv \overline{\chi}_{RES}^{(2)}(t) \cos(\omega_{inh} + \omega_1)t, \tag{3.6}$$

which consists of a time dependent envelope $\overline{\chi}_{RES}^{(2)}(t)$ and an oscillating term with

frequency $\omega_{inh} + \omega_1$. Around the sum frequency the envelope can be approximated by:

$$\overline{\chi}_{RES}^{(2)}(t) = e^{-t/T_2} e^{-t^2(\Delta\omega/2)^2}, \tag{3.7}$$

as long as $\frac{\Delta\omega}{\omega_{inh}} \ll 1$. This is a generalized version of the commonly used equations to fit SFG spectra. If we insert a δ-function distribution of resonance frequencies, $g(\omega_0') = \delta(\omega_0' - \omega_0)$, the homogeneous scenario is retrieved with the response as given by Eg. 3.3. The amount of inhomogeneity is determined by the product $\Delta\omega T_2$; $\Delta\omega T_2 \ll 1$ describes a homogeneous scenario, whereas $\Delta\omega T_2 \gg 1$ yields a totally inhomogeneous distribution of sites. To obtain the frequency domain polarization, we take the Fourier transform of $P^{(2)}(t, \tau = 0)$ and regard the visible field as a CW field again. Applying Eqs. 3.1-3.2 to calculate the FID and the upper part of Eq. 3.4 in combination with the Fourier transform of Eq. 3.6 to reproduce the spectrum yields the fits to the frequency and time-domain data in Fig. 3.4. Using the same dephasing time (T_2=1.65 $\pm$ 0.4 ps) and frequency distribution (ω_{inh} = 2250 cm^{-1} and $\Delta\omega$ = 2.8 $\pm$ 1 cm^{-1} and $\Delta\omega T_2$ = 0.6), both the SFG spectrum and the FID can be reproduced very well with one set of parameters. That this is a unique set of parameters can be seen from the functional form of $\overline{\chi}_{RES}^{(2)}(t)$ immediately. Namely, the function in the exponent is a unique function. This directly translates to the uniqueness of $\overline{\chi}_{RES}^{(2)}(t)$ itself. To illustrate this, Fig. 3.5 shows three calculated SFG spectra and Free Induction Decays for two different sets of $\Delta\omega$ and T_2. $\Delta\omega$=2.8 cm^{-1} and T_2=1.65 ps corresponds to the best fit. The degree of inhomogeneity, $\Delta\omega$, was varied by a factor of 2, and T_2 was treated as a fitting parameter. It clearly demonstrates that a time domain measurement allows for a more accurate estimate of T_2 and $\Delta\omega$ than a frequency domain measurement. For totally inhomogeneous dephasing behavior however, the frequency domain spectrum can be decisive, as it should be totally symmetric around ω_{inh}.
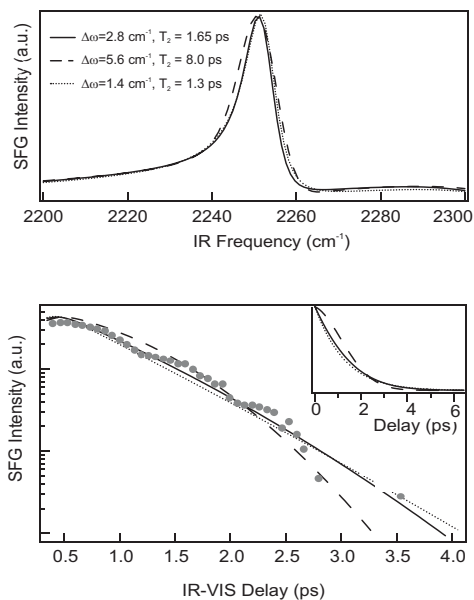
Figure 3.5: Calculated frequency domain (top panel) and time domain SFG spectra (bottom panel) in the C–N stretch region of acetonitrile for different values of $\Delta\omega$ and T_2. The solid line corresponds to the fit in Fig. 3.4. $\Delta\omega$ =1.4 cm^{-1}, T_2 = 1.3 ps corresponds to a more homogeneous scenario ($\cdots$) and $\Delta\omega$ =5.6 cm^{-1}, T_2 = 8.0 ps corresponds to a more inhomogeneous scenario ($- - -$). The time domain data is also shown. The inset shows $\overline{\chi}_{\mathrm{RES}}^{(2)}(\mathrm{t})$ changing shape.

Thus, we can conclude that the time domain measurement is much more sensitive to the spectral line shape. This can be understood by noting that, it is inherently more sensitive to the molecular response than the frequency domain measurement, since the non-resonant signal is only present when the two short pulses overlap. For IR-VIS delay >0.5 ps the time domain-FID is governed solely by the decay of the resonant polarization. In contrast, the frequency domain SFG spectrum does not give an unobscured image of the resonant polarization, since the molecular polarization interferes with the non-resonant metal response over the whole spectral region. Therefore, independent of the line shape model employed, a theoretical description of the frequency domain data will always have one extra parameter, namely the phase difference between the resonant and non-resonant response. Apart from an extra fitting parameter, the frequency domain SFG spectra can also be distorted due to the large dispersion in the refractive index of acetonitrile around the resonance [20]. This effect will be present in the interference region and hence can cause appreciable distortion to the frequency domain

spectrum. Moreover, from an experimental point of view, the signal-to-noise in the time domain experiment can be increased more easily than the signal-to-noise in the frequency domain experiment. Thus, although frequency domain and time domain SFG experiments are theoretically equivalent, they can lead to different conclusions concerning the line shape. To elucidate the vibrational decay mechanism both time and frequency domain measurements should be conducted and analyzed in a detailed fashion.

3.6   The influence of the surface

Now that we have established that there is a difference in line broadening for the C-H and C-N stretch modes of acetonitrile, we can examine the role of the gold surface more closely by comparing the liquid phase infrared spectra of acetonitrile to the acetonitrile/gold spectra (see Fig. 3.6).
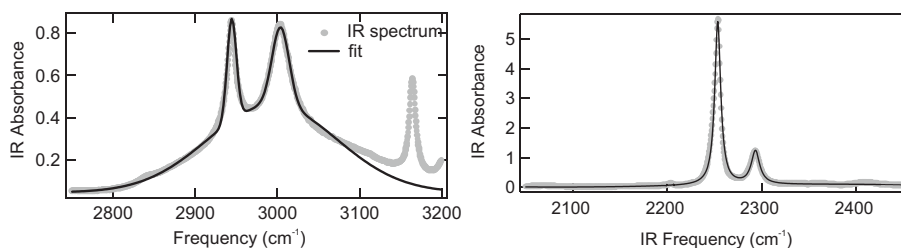
Figure 3.6: IR spectra of a 15 μm thick film of acetonitrile in the C-H stretch (left panel) and the C-N stretch (right panel) spectral regions. The solid lines are fits assuming Lorentzian line shapes, implying homogeneous line broadening. The band at ~3150 cm^{-1} is a combination mode of the C-C and the C-N stretch vibrations and the band at ~2287 cm^{-1} is an overtone of the C-H rocking mode [36].

The infrared spectra in Fig. 3.6 display vibrational resonances corresponding to the C-N stretch mode at 2253 cm^{-1} and resonances corresponding to the symmetric and antisymmetric CH$_3$ stretch modes at 2946 cm^{-1} and 3002 cm^{-1}. From the Lorentzian fits we obtain line widths (Γ) of 8.7 cm^{-1} (corresponding to 0.61 ps) for the symmetric stretch vibration, 26.6 cm^{-1} (corresponding to 0.20 ps) for the antisymmetric stretch vibration and 3.9 cm^{-1} for the symmetric stretch vibration. For both the C-H and C-N stretch modes the obtained resonance frequencies and line widths from the bulk liquid do not differ very much from the ones we have observed with SFG. This means that the effect the gold surface has on the acetonitrile molecules is marginal.

It has been shown that if the CH$_3$ group were pointing down to the surface, the vibrational frequency would be red-shifted [37]. The absence of a frequency shift indicates that acetonitrile molecules point with their C-N end towards the surface. Unlike many other molecules that have been studied on various surfaces with SFG, it is impossible in this system to determine the average orientation of molecules from comparing the amplitude of SFG spectra at various polarization combinations. The procedure of finding the molecular orientation, as described in Appendix A, requires an appropriate distribution function of the molecules at surface layer. Due to the high degree of surface corrugation, it is impossible to accurately determine the distribution function and we cannot just assume that all the molecules are distributed under a certain angle on a flat surface.

The infrared spectra of liquid acetonitrile can be described very well using Lorentzian line shapes, which indicates homogeneous line broadening for both the C-N stretch vibration and the C-H stretch vibrations in liquid acetonitrile. The observed partial inhomogeneity for the C-N stretch vibration can be concluded to be imposed by the surface and not due to any ordering already present in the liquid phase. The surface roughness (displayed in Fig. 3.2) leads to the appearance of different adsorption sites, resulting in an inhomogeneous distribution of vibrational resonances for the vibrational mode that is closest to the surface.

3.7   Conclusions

We have shown it is possible to study molecules absorbed onto a very thin gold film using femtosecond sum frequency generation. By applying time and frequency domain sum frequency generation, we have found that, although both measurement schemes are theoretically equivalent, they can lead to different conclusions concerning the line shape. To elucidate the vibrational decay mechanism both time and frequency domain measurements should be conducted and analyzed in a detailed fashion. The effect of the gold surface on acetonitrile is a marginal one, resulting only in the inhomogeneity of vibrational mode that is closest to the surface (the C-N stretch mode).

Chapter 4

Time resolved sum frequency generation

We present an investigation into femtosecond time-resolved vibrational sum frequency spectroscopy as a tool for studying ultrafast surface dynamics. It is demonstrated that the presence of experimentally observed new spectral features does not necessarily mean that a novel (transient) chemical species has appeared on the surface. When a strong visible pump pulse is used in pump sum frequency probe experiments, the perturbation of the free induction decay (FID) leads to transient line shifts even at negative delay times, i.e. when the IR-VIS SFG probe pair precedes the pump pulse. Based on an analysis of the time-dependent polarization we discuss the influence of the perturbed FID on time-resolved SFG spectra. In particular, we investigate how coherent effects modify the SFG spectra and we examine the time resolution in these experiments in relation with the dephasing time. In addition, we present a simple model for calculating the sum frequency intensity while a chemical reaction takes place on the surface via a transition state or reaction intermediate. These calculations show that a transition state can be observed and that its lifetime can be determined, using pump-probe sum frequency generation.

4.1   Introduction

Femtosecond spectroscopy has proven to be a powerful tool to study the dynamics of the interaction between molecules and metal surfaces, which is of fundamental importance in understanding chemical reactions and physical processes on surfaces [38, 39, 40, 41, 42, 13, 43, 44, 45]. These measurements generally employ a pump-probe scheme, in which the surface is excited by a femtosecond pump pulse and changes are probed with a time-delayed femtosecond laser pulse. Upon excitation with a femtosecond laser pulse, the energy is inserted into electronic degrees of freedom of the metal surface (see Fig. 4.1). The energy stored in these hot electrons can flow to the adsorbate via an electronic resonance or through coupling with the phonons [44]. Direct excitation of the small-molecule adsorbate [45] is a process of low probability and can often be neglected. Several time-resolved studies have been carried out to investigate the dynamical surface-adsorbate interactions of e.g. NO/Pd(111) [40], CO/Cu(100) [41, 42, 46, 47], CO/Cu(111) [13], CO/Ni(111) [43] and Cs/Cu(111) [45]. For a full microscopic understanding of molecular processes at these surfaces, the dynamics of vibrational excitations, energy exchange and relaxation in adsorbate surface systems is of prime importance [48]. Among various vibrational spectroscopies, vibrational sum-frequency generation (SFG) is a surface sensitive nonlinear optical technique that enables the study of adsorbates with high sensitivity and molecular specificity even at ambient conditions [49].

Using ultrashort laser pulses in combination with vibrational sum-frequency generation the dynamics of energy and phase relaxation of vibrational excited states can be investigated directly. For example the energy relaxation time T_1 of the vibrational population induced by an infrared (IR) pump pulse can be measured by SFG-spectroscopy without assumptions about the contribution to the line width of pure dephasing and inhomogeneous broadening [34, 41]. Furthermore, time-resolved sum frequency generation has great potential to investigate reaction intermediates and the coupling between different vibrational modes during the course of a surface reaction, since molecular vibrations of adsorbates can provide direct insights into the formation and breaking of chemical bonds at surfaces. In such experiments the reaction is initiated by a pump pulse and its temporal evolution is monitored by recording transient SFG spectra of the adsorbate layer on an ultrashort time scale. So far, few experiments have been reported using this type of pump-probe SFG spectroscopy as a molecule specific probe. Bandara et al. studied the conversion between two formate species (HCOO$^-$) adsorbed on NiO(111) with 30 ps time resolution [43, 50]. Using femtosecond pump-probe SFG spectroscopy the dynamics of the CO stretch vibration on Ru(001) and its coupling to low frequency vibrational modes and the subsequent desorption have been studied [44, 51]. In the latter experiments IR-broadband SFG spectroscopy was employed to record vibrational snapshots.
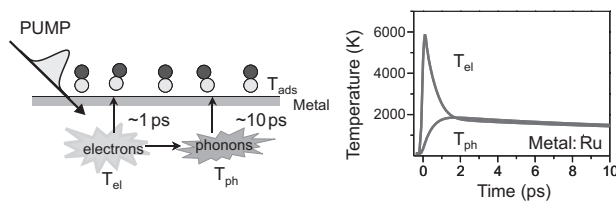
Figure 4.1: Pathways and time scales of energy flow following excitation of a metal surface by an ultrashort laser pulse (left). Calculated electron and phonon temperature using the two temperature model [27] after excitation at t=0 of a Ru surface with a pulse duration of 130 fs and 19 mJ/cm^2 (right).

The aim of these experiments is to obtain information about reaction time scales and pathways, in particular, on transition states and reaction intermediates, since these are essential in the description and understanding of chemical reactions. As the transition state inherently has a short lifetime, a very high time resolution is required to observe it. Moreover, transition state spectroscopy requires chemical specificity that allows one to probe the rearrangement of chemical bonds, such as vibrational spectroscopy. As mentioned above, pump SFG-probe spectroscopy combines femtosecond time resolution with chemical surface specificity and should be an ideal candidate for observing transition states. To the best of our knowledge, transition states have not yet been observed on surfaces.

We present here a general investigation into time resolved SFG as a probe of ultrafast surface processes, such as surface reactions. It is demonstrated that there are important differences in the interpretation of vibrational spectra between pump SFG-probe spectroscopy and static vibrational spectroscopies such as Reflection Absorption Infrared Spectroscopy (RAIRS) and Electron Energy Loss Spectroscopy (EELS) [48]. These effects are illustrated by numerically calculating pump SFG-probe spectra for CO adsorbed on Ru(001) and comparing these with recent experimental data [51] (in section 4.2). Next, we will use simple analytical models to discuss the influence of the free induction decay (FID) on the transient SFG spectra (in section 4.3) and the time-resolution of the pump/SFG-probe scheme (section 4.4). In section 4.5, we have investigated the effect on the SFG spectra of a simple chemical reaction taking place on the surface via a short-lived transition state, and demonstrate that with this technique it is possible to observe transition states and determine their lifetimes.

4.2   Modeling the CO/Ru(001) system
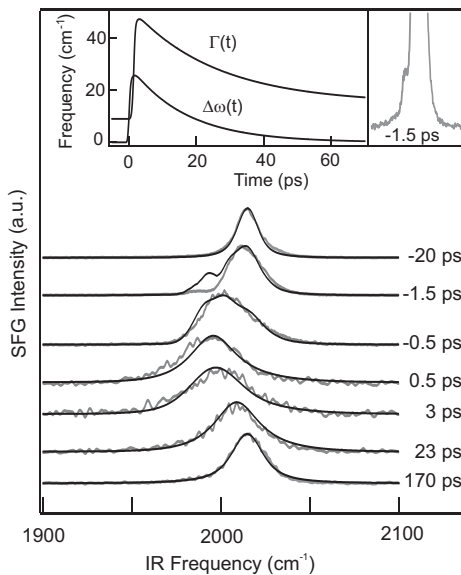
Figure 4.2: Normalized pump/SFG-probe spectra of CO/Ru(001) (adopted from [51]) (grey lines) at different delay times together with spectra (black lines) calculated with $\Gamma(t)$ and $\Delta\omega(t)$ as depicted in the inset. Spatial averaging due to finite spot sizes has been taken into account. The calculated spectra reproduce important features such as the asymmetry (-0.5 ps) and side peak (slightly overestimated by the model, at -1.5 ps).

Fig. 4.2 shows pump/SFG-probe spectra of CO adsorbed on Ru(001) in the $(\sqrt{3} \times \sqrt{3})$ structure (reproduced from Ref. [51]). In these experiments the SFG spectra are taken at different delay times between the probe pair (consisting of a tunable femtosecond IR pulse and a spectrally narrow 800 nm pulse) and a femtosecond (800 nm) pump pulse. Due to energy flow from the metal to the adsorbate (as illustrated in Fig. 4.1) the molecules become hot and desorption of a large fraction ($\sim$ 25%) of the ad-layer takes place [51]. As a consequence, the spectra are strongly modified as a function of delay time. The resonance frequency, line width and intensity change, and a side peak appears, most notably for -1.5 ps delay time (see inset). It should be noted that the time-resolution in these experiments is determined by the duration of the femtosecond infrared and excitation pulse, rather than by the decay of the infrared polarization (typically ~1 ps). This will be discussed more thoroughly in section 4.4. The pump-induced spectral modifications

were fully reproducible, indicating no structural surface changes due to the excitation.

In the interpretation of static vibrational spectra the observed spectral modifications would point towards structural or chemical changes on the surface, such as new binding sites or tilted structures. To investigate if this is also the case for pump/SFG-probe spectroscopy, it is necessary to calculate these sum frequency spectra.

The SFG intensity can be calculated from the Fourier transform of the time-dependent polarization [16]:

$$
\begin{aligned}
I_{SFG}(\omega, \tau_d) \quad &\propto \quad \left| \mathbf{P}^{(2)}(\omega, \tau_d) \right|^2 = \left| \int dt e^{-i\omega t} \mathbf{P}^{(2)}(t, \tau_d) \right|^2 \qquad (4.1) \\
&= \quad \left| \int dt e^{-i\omega t} (\mathbf{P}^{(2)}_{RES}(t, \tau_d) + \mathbf{P}^{(2)}_{NR}(t)) \right|^2 ,
\end{aligned}
$$

where $\mathbf{P}^{(2)}_{RES}$ is the vibrational polarization set up by $\mathbf{E}_2$ (with frequency ω_2) and τ_d is the pump-probe delay time. $\mathbf{P}^{(2)}_{NR}$ is independent of the pump-probe delay. Evaluation of this expression requires knowledge of $\mathbf{P}^{(2)}_{RES}$, which can be found by summing up all the individual responses of the molecules at the interface. If the pulse duration is short compared to the dephasing time the CO molecules are excited coherently, which means that the total time-dependent response is just the product of the number of molecules with a single molecular response. For non-resonant visible and sum frequency fields, the polarization $\mathbf{p}^{(2)}(t)$ generated by one molecule can be written as a product of the linear infrared polarization ($\mathbf{p}_{IR}(t)$) [15], the Raman polarizability, $\overset{\leftrightarrow}{(\mathbf{R})}$ and the visible field (see Appendix A).

The IR polarization can be calculated by solving the Bloch equations, which describe the time-dependent evolution of the density matrix $\overset{\leftrightarrow}{(\rho)}$ for a two level system [15, 16] (with energy levels n and m and matrix elements ρ_{mn}, ρ_{nm}, ρ_{mm} and ρ_{nn}). Using for the off-diagonal elements of $\overset{\leftrightarrow}{\rho}$ $\rho_{nm} = \sigma_{nm} e^{-i\omega t} = \frac{1}{2}(u - iv)e^{-i\omega t}$ and for the population difference w, $w = \rho_{mm} - \rho_{nn}$, the Bloch equations in the electric dipole[1] and rotating wave approximations[2] can be written as:

$$
\begin{aligned}
\dot{u} &= (\omega - (\omega_{CO} - \Delta\omega(t)))v - u\Gamma(t) \\
\dot{v} &= -(\omega - (\omega_{CO} - \Delta\omega(t)))u - v\Gamma(t) + \kappa E_{IR} w \qquad (4.2) \\
\dot{w} &= -\frac{(w - w^{eq})}{T_1} - \kappa E_{IR} v,
\end{aligned}
$$

---

[1] The interaction Hamiltonian V is only given by $\mathbf{V} = -\overset{\leftrightarrow}{\mu}\mathbf{E}_2$

[2] The off-diagonal elements are driven only close to their resonance, i.e. $V_{mn} = -\mu_{mn}(E_{IR}e^{-i\omega t} + E^*_{IR}e^{i\omega t}) = -\mu_{mn}E_{IR}e^{-i\omega t}$

in which w^{eq} is the population difference at thermal equilibrium, $\kappa = \frac{2\mu_{nm}}{\hbar}$ is the atom-field coupling constant, T_1 the (time independent) decay time from state m to n. E_2 and κ are assumed to be real quantities. $\Delta\omega(t)$ is the time-dependent response function of the resonance frequency (ω_{CO}) and $\Gamma(t)$ the time-dependent response of the line width of the CO stretch vibration (equivalent to the total dephasing time since $\Gamma = 1/T_2$).

$\Delta\omega(t)$ and $\Gamma(t)$ depend on the interaction of the pump pulse with the metal surface. They can be obtained by first calculating the electron and phonon temperature (as displayed in Fig. 4.1) with the two temperature model [27]. Using the obtained electron and phonon temperature, we can find a phenomenological adsorbate temperature from a friction model calculation [42]. The adsorbate temperature can be related to the excitation of low energy vibrational modes of the adsorbate molecules that couple with the CO stretch vibration [44, 51, 52]. This results in the time dependent resonance frequency ($\Delta\omega(t)$) and line width ($\Gamma(t)$) as displayed in Fig. 4.2.

When the Bloch equations (Eqs. 4.2) are solved using $\Delta\omega(t)$ and $\Gamma(t)$ shown in the left inset of Fig. 4.2 the pump/SFG-probe spectra can be reproduced (the black lines in Fig. 4.2), without assuming any chemical or structural change. The calculated spectra match the experimental data in the observed red shift, the line broadening and the side peak. Apparently, these are not due to chemical or structural changes, but rather to a strong transient perturbation of the vibration of the adsorbate, that comes about through phonon-adsorbate interactions [44]. Hence, although a large fraction of molecules desorb as a consequence of the excitation pulse, there is no indication of an effect of desorption on these SFG spectra, in agreement with calculations presented below. Interpretation of pump/SFG-probe spectra therefore has to be performed with some care.

4.3 Effect of FID on transient spectral features
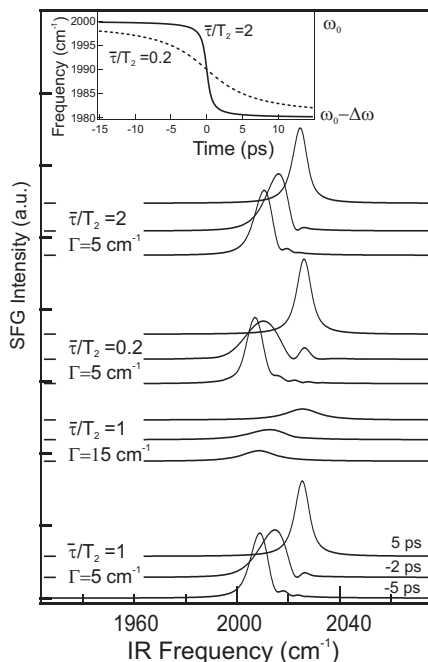
Figure 4.3: Calculated SFG spectra at different delay times using the vibrational response function ($\Delta\omega(t)$) shown in the inset at different rates and dephasing times ($\Gamma = 1/T_2$). Note that here delay zero is defined at half the frequency change. The rate of change is given with respect to the dephasing time ($\overline{\tau}/T_2$). The resonance frequency ω_{CO} is chosen to be 2000 cm^{-1} and $\Delta\omega = 20$ cm^{-1}.

To investigate spectral changes that are due to the interaction of a pump pulse with a metal surface in more detail we have performed simple model calculations. We assume that the response of the molecules to the pump pulse consists of a red shift ($\Delta\omega(t)$) of the vibrational frequency and obtain the SFG intensity by solving the Bloch equations. Fig. 4.3 shows calculated SFG spectra at several pump-probe delay times for frequency changes at different rates for varying dephasing times. The dimensionless rate of change ($\overline{\tau}/T_2$) is expressed relative to T_2 and is depicted in the inset of Fig. 4.3.

At delay times as early as -5 ps the peaks are already distorted (this effect is also present in the data of Fig. 4.2). This distortion occurs, because the vibrational resonance changes while the IR polarization is present at the surface, leading to a perturbed Free Induction Decay (FID) [46]. When the delay time approaches zero, the effect of the pump pulse on the vibrational polarization field becomes increasingly large, which results in more pronounced side bands appearing in

the SFG spectra. These effects are largest at about -2 ps delay when the overlap time of the polarization with the pump-induced modifications is maximum. The spectral changes decrease when this overlap time becomes smaller, i.e. at larger delay times, or for a faster change of $\Delta\omega(t)$. A slow change of $\Delta\omega(t)$ increases the interaction time, accounting for the larger spectral changes for slower frequency modulation.

Fig. 4.3 also shows that a shorter dephasing time (larger line width, $\Gamma=15$ cm^{-1}) leads to broader peaks with less pronounced dynamical spectral features. This can also be explained in terms of interaction time: A shorter T_2 means that $\mathbf{P}_{RES}^{(2)}$ decays faster, reducing the interaction time and resulting in less pronounced spectral features. The influence of the free induction decay on the apparent time-resolution in a pump/SFG-probe scheme will be discussed in the following section.

4.4   Effect of FID on time resolution

To obtain insights in how the transient SFG spectra are influenced by a perturbed free-induction decay, we have performed model calculations of time-resolved SFG spectra for a simple scenario of the time-dependent frequency $\omega(t)$ of a vibrational resonance. In this model, which is illustrated in the upper panel of Fig. 4.4, the frequency of the resonance (the CO stretch) is assumed to shift instantaneously upon excitation with the pump pulse. Such a response would correspond to an ultrafast (electron-mediated) excitation of the adsorbate and is similar to the one used in section 4.3. The assumption of the model used here allows us to separate the effect of the perturbed FID from the finite energy transfer rate between the substrate and the adsorbate. In the model, a shift of the resonance frequency back to its original value is chosen to occur linearly with time as shown in Fig. 4.4. This approximation enables us to obtain insightful analytical solutions for the SFG spectra. We calculate the SFG spectrum at various time delays τ_d between the pump and the IR pulse of the SFG probe according to Eq. 4.1.
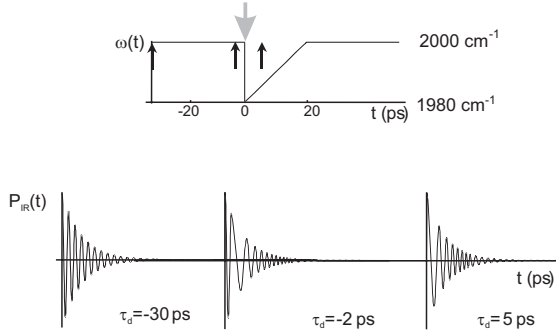
Figure 4.4: Description of the model used to study the effect of the free-induction decay induced by an ultrashort IR pulse on the transient SFG spectra. Top: The pump induced frequency response of the vibrational resonance used to model pump/SFG-probe spectra. The black arrows mark the delay times used with respect to the pump pulse (grey arrow). The resonance frequency ($\omega_{CO} - \Delta\omega(t)$) of the CO stretch is assumed to respond instantaneously to the excitation by the pump pulse and to relax to its original value linearly. Bottom: Illustration of the time dependence of the induced polarization $\mathbf{P}_{IR}(t)$ for pump-probe delay times of -30, -2 and 5 ps and $T_2 = 1$ ps.

For simplicity the IR field $\mathbf{E}_2$ is assumed to be a δ-function and the visible field a continuous-wave field (in the time domain). These approximations barely affect the outcome of the calculations, as evidenced by comparison to full numerical calculations using the two-level Bloch equations [53]. For the sake of clarity and simplicity, the line width or, equivalently, the dephasing time is kept fixed and the time-independent instantaneous non-resonant contribution is set zero. The calculated spectra are depicted centered around the IR-resonance. The lower panel of Fig. 4.4 depicts the time-dependent infrared polarization $\mathbf{P}_{IR}(t)$ for $T_2 = 1$ ps, at delays of -30 ps, -2 ps and 5 ps between the pump and the IR pulse. At large negative delay ($\tau_d = -30$ ps), the pump pulse arrives long after the probe pair, which is too late to perturb the decay of the coherent polarization. As the infrared polarization, oscillates with the frequency of the vibrational resonance, it also changes when the resonance frequency changes after the excitation by the pump pulse. If this frequency change occurs at small negative delays (e.g. -2 ps) the polarization changes on a time scale of the dephasing time T_2. At small positive delays $\mathbf{P}_{IR}(t)$ also changes with time. As the SFG spectrum is determined by the Fourier transform of $P_{RES}^{(2)}(t)$, a change in the polarization necessarily results in a change of the SFG spectrum. A larger T_2 corresponds to a longer decay time of the polarization and hence a large time window to modify $P_{RES}^{(2)}(t)$ and the SFG spectrum. This is demonstrated in Fig. 4.5, which compares calculated SFG spec-

tra for the pump-induced frequency changes of Fig. 4.4 at several delay times. The upper panel shows three SFG-spectra for $T_2 = 1$ ps, which approximates the pump/SFG-probe experiment at 340 K with respect to the dephasing time [54].
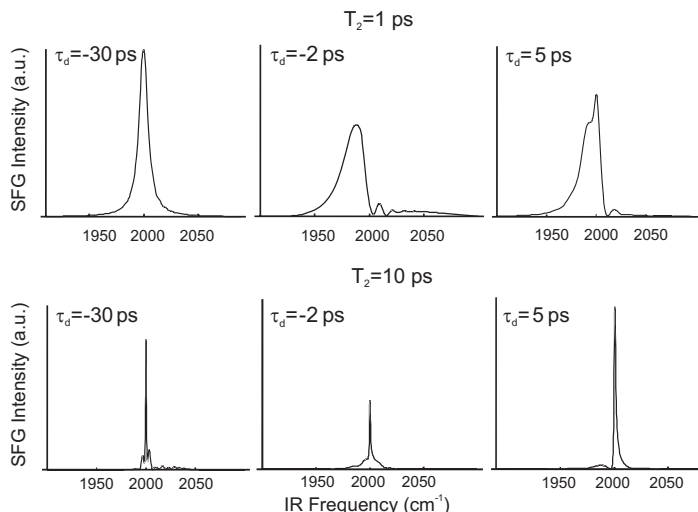

Figure 4.5: pump/SFG-probe spectra for the pump induced change in Fig.4.4 at delay times -30, -2, 5 ps and $T_2 = 1$ ps (upper panel) and $T_2 = 10$ ps (lower panel). For delays $|\tau_d| \gg T_2$ the pump pulse has no influence on the decay of the vibrational polarization leaving the SFG spectrum undistorted (see text).

Fig. 4.5 demonstrates that quite different SFG spectra can be obtained within the time span of T_2. The results of our model calculations show qualitatively that in a pump/SFG-probe experiment in which the dynamics of a vibrational resonance are investigated, unperturbed SFG spectra are expected to be observed only for delays much longer that the dephasing time, i.e. for $\tau_d \gg T_2$. In case of the CO stretch vibration of CO/Ru(001) the frequency shift at negative delays (see Fig. 4.2) clearly demonstrates the perturbation of the free induction decay by the pump pulse due to the finite decay time of the vibrational coherence. An important question that arises from the observed pump-induced spectral changes is how the time-resolution of our pump/SFG-probe scheme is influenced by the dephasing time T_2. In other words, although the time resolution is determined by the duration of the pump and IR pulses, the spectral changes for a given delay time strongly depend on the dephasing time. Fig. 4.6 shows three calculated SFG spectra at pump-probe delays of 200 fs, 1.2 ps and 3.0 ps, for $T_2 = 1$ ps. The pump-induced frequency response used in this calculation is the same as in Fig. 4.4. Even for relatively closely spaced delay times the SFG spectra are clearly different. To quantify the change in the SFG spectrum, we use the fractional integrated (absolute) intensity difference ΔI of two SFG spectra at a given delay time and zero ($\tau_d = 0$). Comparing this difference ΔI (i.e. a measure of the change in the

SFG spectra) for the same T_2 yields a measure of the achievable time resolution.
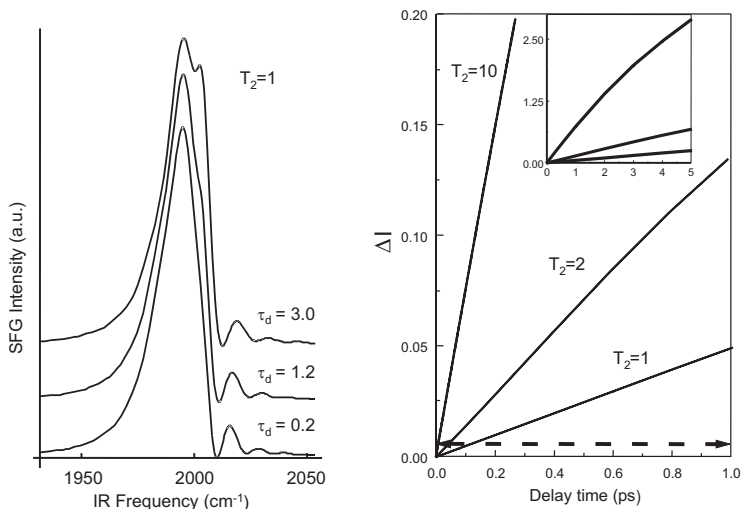
Figure 4.6: Calculations illustrating the time resolution in the time-resolved SFG experiment: (a) SFG spectra for $T_2 = 1$ ps at delay times of 200 fs, 1.2 ps and 3.0 ps. The transient change in the frequency is the same as in Fig. 4.4 (b). A plot of the fractional integrated (absolute) intensity difference ΔI vs delay time τ_d for $T_2 = 1$, 2 and 10 ps. The dashed line indicates a 1 % change in a SFG spectrum at zero delay for $T_2 = 1$ ps as an estimate of the typical experimental sensitivity. The inset shows the changes for larger delay times.

Fig. 4.6 shows ΔI as a function of the delay time for three different dephasing times. The dashed line indicates a 1 % change in the integrated spectrum of T_2 = 1 ps at zero pump-probe delay - as an estimate of the experimental sensitivity. It can be seen that a larger T_2 would lead to a better time resolution (more rapidly developing changes in the spectrum as a function of delay time). Although this result may seem counter-intuitive because the polarization decays slower, it is a consequence of the fact that the SFG intensity is determined by the Fourier transform of the time-dependent polarization. For longer T_2's the spectral features are sharper, and therefore more sensitive to (small) changes of the polarization. However, it should be noted that within the time window of T_2 a detailed understanding of the experimental results is accessible only via a detailed model, which describes the relaxation dynamics as well as the frequency shifts as a function of time.

4.5   Observing transition states

The question arises whether it is possible to observe short-time chemical changes induced by the pump pulse, i.e. whether it is possible to perform transition-state spectroscopy on surfaces with pump/SFG-probe. To investigate this we consider a simple system in which substrate-mediated interaction of a pump pulse with an adsorbed overlayer leads to a chemical reaction that develops via a transition state:

$$A \overset{R(t)}{\to} A^{\ddagger} \to B,$$
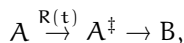
where $R(t)$ is the reaction rate that determines the number of molecules entering the transition state at time t. These three species can each be characterized by a resonance frequency ($\omega_A, \omega_A - \Delta\omega, \omega_B$) for A, $A^{\ddagger}$ and B, respectively, and a total dephasing time (T_2^A for A and $A^{\ddagger}$ and T_2^B for B). The transition state is further characterized by a short lifetime $\tau^{\ddagger}$. It is clear that $\Delta\omega$ contains information about the *structure* of the transition state, and $\tau^{\ddagger}$ about its *dynamics*. For the three individual susceptibilities of the sub-ensembles A (given by $\chi_A^{(2)}(t)$) , $A^{\ddagger}$ ($\chi_{A^{\ddagger}}^{(2)}(t)$) and B ($\chi_B^{(2)}(t)$), we assume that the reaction to the IR field decays exponentially so that the resonant polarization (for a given combination of input and output field polarization directions) becomes:

$$
\begin{aligned}
P^{(2)}(t) &= P_A^{(2)}(t) + P_{A^{\ddagger}}^{(2)}(t) + P_B^{(2)}(t) & (4.3)\\
&= \chi_A^{(2)}(t)e^{i(\omega_A+\omega_1)t} + \chi_{A^{\ddagger}}^{(2)}(t)e^{i(\omega_A-\Delta\omega+\omega_1)t} + \chi_B^{(2)}(t)e^{i(\omega_B+\omega_1)t}\\
&= e^{-t\Gamma^A}e^{i(\omega_A+\omega_1)t} + e^{-t\Gamma^{\ddagger}}e^{i(\omega_A-\Delta\omega+\omega_1)t} + e^{-t\Gamma^B}e^{i(\omega_B+\omega_1)t},
\end{aligned}
$$

where $\Gamma^A = 1/T_2^A$, $\Gamma^{\ddagger} = 1/T_2^A + 1/\tau^{\ddagger}$, and $\Gamma^B = 1/T_2^B$.
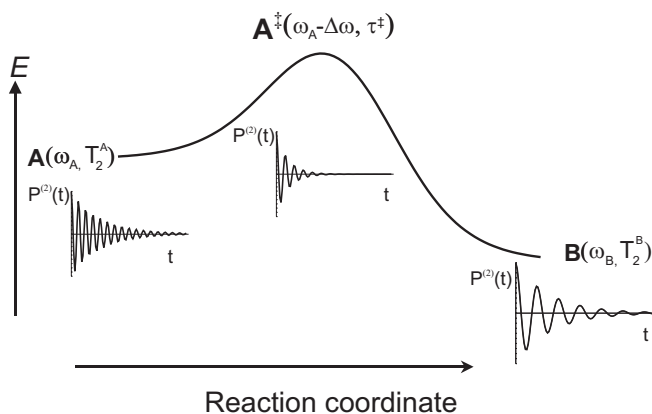

Figure 4.7: Schematic representation of a reaction occurring via a transition state together with an illustration of the modulation of the polarization.

Fig. 4.7 illustrates the different species on the surface together with their contribution to the polarization. Because the lifetime of the transition state is very short and the number of molecules residing in it is small compared to the total amount of molecules, the amount of molecules in state B can be approximated by the total number that has left $A^{\ddagger}$ at time $t - \tau^{\ddagger}$. The total polarization can now be given by the sum of three terms:

$$P^{(2)}(t) = [N_0 - \int_{-\infty}^{t} dt' R(t')] P_A^{(2)}(t - \tau_d) + \int_{-\infty}^{t} dt' R(t') P_{A^{\ddagger}}^{(2)}(t' - \tau_d)$$

$$+ \; [\int_{-\infty}^{t-\tau^{\ddagger}} dt' R(t')] P_B^{(2)}(t - \tau_d), \qquad (4.4)$$

where τ_d is the pump-probe delay and N_0 the total number of molecules. The first and third term consist of a product of an amplitude and a susceptibility, whereas in the second term the decay of the amplitude has been incorporated in the susceptibility. If $R(t)$ and the infrared and visible fields are known, the SFG intensity can be obtained from Eq. 4.1.

For most surface reactions the reaction products desorb so that $P_B^{(2)} = 0$, because gas phase molecules do not contribute to the sum frequency signal. Reaction rates typically lie in the sub-picosecond region (for desorption e.g. NO/Pd(111) [40], CO/Cu(100) [41, 42, 46], CO/Cu(111) [13], O_2/Pt(111) [55] and for oxidation of CO/Ru(001) [44]). The reaction rate can be approximated by the following expression:

$$R(t) = \frac{(a+b)N_0}{a^2} e^{-\frac{t}{a}} (1 - e^{-\frac{t}{b}}) \theta(t), \qquad (4.5)$$

where a (b) determines the speed of the decay (rise) of the reaction rate, $\theta(t)$ is the Heavyside function, and $R(t)$ is normalized to the initial coverage N_0. All molecules are assumed to react due to (substrate mediated) interaction with the pump pulse. When the femtosecond IR pulse is approximated by a δ-function in the time domain and the temporally long visible field by a cw field, the SFG intensity can be found analytically from Eqs. 4.1, 4.4 and 4.5, as opposed to solving Eqs. 4.2 numerically. As cross terms are negligible (they are smaller than $10^{-3}|P_{A^{\ddagger}}^{(2)}(\omega)|^2$) the sum frequency signal is given by:

$$I_0(\omega) \propto$$

$$\frac{(a+b)^2 N_0^2 e^{-2\Gamma^A \tau_d}}{a^4 b^2 (\Gamma^A)^2 ((\omega - \omega_A)^2 + (\Gamma^A)^2)((\omega - \omega_A)^2 + (\Gamma')^2)((\omega - \omega_A)^2 + (\Gamma'')^2)} +$$

$$\frac{(a+b)^2 N_0^2 e^{-2\Gamma^{A^{\ddagger}} \tau_d}}{a^4 b^2 \omega^2 ((\omega - (\omega_A - \Delta\omega))^2 + (\Gamma^{A^{\ddagger}})^2)((\omega - (\omega_A - \Delta\omega))^2 + (\Gamma^{A^{\ddagger}} + 1/a + 1/b)^2)},$$

$$(4.6)$$

where $\Gamma' = \Gamma^A + 1/a$ and $\Gamma'' = \Gamma^A + 1/a + 1/b$. The first term in Eq. 4.6 represents the contribution to the spectrum of molecules still residing on the surface. This peak is centered at ω_A and broadened by T_2^A, a and b. The disappearance of molecules results in an additional broadening of this peak. The second term represents a peak centered at $\omega_A - \Delta\omega$ whose width and intensity are dependent predominantly on $\tau^\ddagger$, a and b.
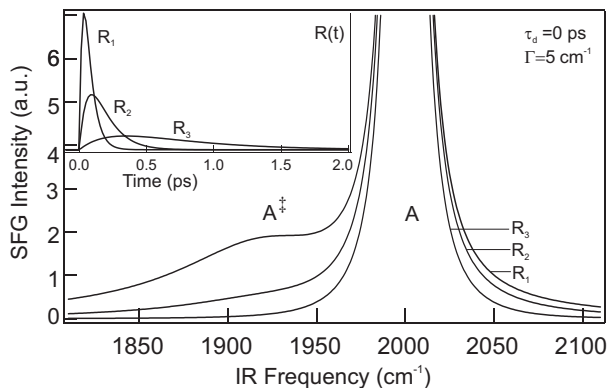
Figure 4.8: Calculated SFG spectra for different desorption functions R(t) (Eq. 4.5) shown in the inset having corresponding line types. the arrow marks the appearance of the transition state peak in the spectrum. The resonance frequency ω_A is chosen to be 2000 cm^{-1} and $\Delta\omega$=80 cm^{-1}. The peak maximum of the SFG signal is 100.

Fig. 4.8 shows three calculated SFG spectra for different reaction rates (shown in the inset of Fig. 4.8) setting $\tau^\ddagger$=0.1 ps, and Γ=5 cm^{-1}. This Figure shows that, even for very short $\tau^\ddagger$, reacting molecules can contribute to the observed SFG signal and that it is possible to extract $\tau^\ddagger$ from the spectral intensity and line width. Fast reaction leads to a larger contribution from the molecules in the transition state to the SFG intensity. In all three reaction curves the molecules have left the surface after 3 ps. For the slowest reaction process the spectral changes are not very pronounced, demonstrating that reacting molecules only contribute significantly to the signal if the reaction occurs within several picoseconds, i.e. in an electron-mediated scenario. This explains why desorbing CO does not contribute to the SFG spectra shown in Fig. 4.2: the desorption is phonon-mediated and takes ~20 ps [44]. Fig. 4.9 shows the effect of different transition-state lifetimes on the SFG spectra. A longer lifetime is shown to lead to a bigger contribution of the desorbing molecules to the SFG spectra. Longer lived reaction intermediates should certainly be observable.

In these calculations the parameters that determine the characteristics of the transition-state (Γ and $\Delta\omega$) were taken to be constants. This means that no re-

sponses due to coupling of the vibrations with phonons were considered and that the reaction does not proceed through a continuum of states (as one would expect for e.g. a barrier-less desorption process). Both effects can be incorporated into the theory by making $\Delta\omega$ and Γ time-dependent. As a reaction that might be suited for obtaining information on the transition state as described in this chapter we suggest the oxidation of CO on Ru(001). This is a very rapid electron-mediated reaction [51] which occurs via a transition state [56].
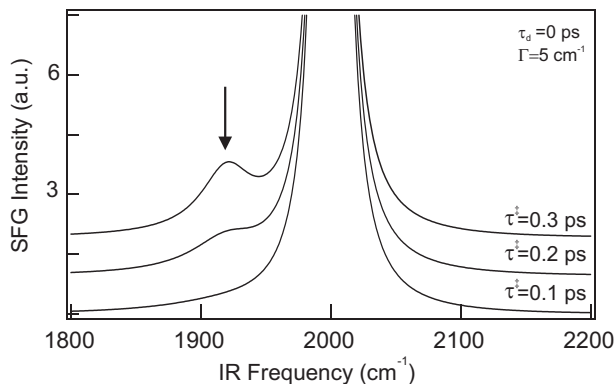
Figure 4.9: Calculated sum frequency spectra for desorbing molecules having different transition-state lifetimes and dephasing times ($\tau_d = 0$). The resonance frequency ω_A is chosen to be 2000 cm^{-1} and $\Delta\omega$=80 cm^{-1}. The peak maximum of the SFG signal is 100.

4.6 Conclusions

In summary, we have shown that changes in the pump/SFG-probe spectra do not necessarily point to chemical or structural changes on the surface and can be reproduced with calculations. Based on an analysis of the time-dependent polarization we have examined the influence of the perturbed FID on time-resolved SFG spectra. In particular, we have investigated how coherent effects modify the SFG spectra and we studied the time resolution in these experiments in dependence of the dephasing time. We have also calculated SFG spectra for a pump pulse inducing a simple reaction occurring via a transition state. For the reaction of an adsorbed overlayer we found that if the reaction is fast in response to the pump pulse, i.e. within several picoseconds, measurable changes in the SFG spectra can be observed. Thus, it should be possible to determine transition states and lifetimes from SFG measurements on metal surfaces.

Chapter 5

The phase behavior of phospholipids

The phase behavior of a biomimetic monolayer consisting of diphospholipid molecules on water is investigated using vibrational sum frequency generation and fluorescence microscopy. In addition to the transition from the – molecularly disordered – liquid phase to the highly ordered and oriented condensed phase, a novel, extremely sharp transition is observed at low compression, which is attributed to the uncurling of the hydrophobic alkane chains upon compression. At higher density there is a continuous order-disorder transition in the coexistence region of the liquid expanded and liquid condensed phase. This transition can be modeled by calculating the density dependent SFG intensity. This model indicates that on average only four chain defects are sufficient to change the SFG signal dramatically.

5.1   Introduction

The interest in the behavior of phospholipid layers on water is due to its importance as a key constituent of biological membranes. Lipid molecules, such as L-1,2-Dipalmitoyl-sn-glycero-3-phosphocholine (DPPC) under study here, consist of a polar headgroup and two long apolar alkyl chains, as shown in the inset of Fig. 5.1. Its bipolar structure gives rise to fascinating behavior, such as self-organization into different phases. Monolayers are excellent model systems for membrane biophysics, since a biological membrane can be considered as two weakly coupled monolayers. Of particular interest is the phase behavior as a function of lateral pressure, which has been studied with various thermodynamic and spectroscopic techniques [57]. It is clear that insight into the molecular and microscopic structure associated with the phase behavior of phospholipid layers is essential for a complete understanding of cell membrane and vesicle properties.

   We have investigated the phase behavior of a DPPC monolayer on water using vibrational sum frequency spectroscopy [16] (SFG) in conjunction with fluorescence microscopy [58, 59]. Second-order nonlinear spectroscopies, with their intrinsic surface sensitivity [16], have provided important molecular-level insights into biological surface systems [60]. In particular, SFG [61, 62] has been used to probe DPPC phospholipid layers at the liquid-liquid interface, as well as the kinetics of bilayer formation from vesicle rupture [63], by monitoring C–H stretch vibrations of both CH_2 and terminal CH_3 groups in the alkyl chain. Vibrational SFG is a very powerful spatially averaged local probe of molecular structure and orientation and provides information that is complementary to that obtained with the spatially resolved, but molecularly unspecific fluorescence microscopy [58, 59].

   Using vibrational SFG we observe, for the first time, a very sharp transition from a phase with curled alkyl chains to a phase with spatially extended chains. This transition, occurring at relatively low DPPC densities, cannot be observed with fluorescence microscopy and is not accompanied by significant changes in surface pressure. In addition, we analyze the order and orientation of the alkyl chains throughout the phase diagram.

   The outline of this Chapter is as follows. After a brief description of the experimental details we will introduce the isotherm of DPPC and illustrate the potential of vibrational SFG to study the molecular structure and orientation of the DPPC molecules (section 5.3). In sections 5.4 and 5.5 we will study the molecular properties of DPPC at increasing surface pressures.
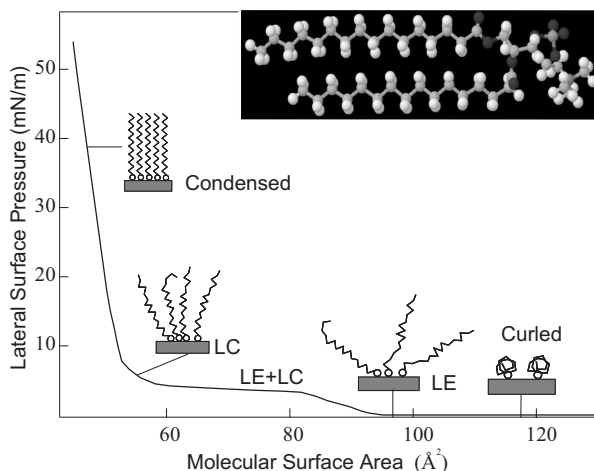
Figure 5.1: Isotherm of DPPC showing the condensed, liquid compressed–liquid expanded coexistence and the liquid expanded phase. After Refs. [58, 59]. Also shown is a molecular model of DPPC. Schematic drawings of the lipid monolayer illustrate the main findings in this Chapter.

5.2 Experimental

DPPC was obtained from Avanti Polar Lipids (Birmingham, Alabama), as was the fluorescent probe, NBD-PC[1]. The fluorescence experiments were carried out with a probe concentration of 0.5 mol% [58, 59]. The phospholipid was spread from a chloroform solution (Fisher HPLC grade) of 1 mM concentration onto Millipore water (18.2 MΩcm resistivity) of pH 7, in a home-built Teflon trough (dimensions 6x40 cm^2). Fluorescence images were taken with a charge-coupled device (CCD) camera mounted on a fluorescence microscope, with a 20$\times$/0.4 NA achromat microscope objective. The SFG experiments (without fluorescent probe) were performed using 120 fs (0.7-7 μJ) infrared pulses (FWHM bandwidth of ~180 cm^{-1}) centered at 2930 cm^{-1} and 3.5 μJ, 800 nm pulses with an 11 cm^{-1} bandwidth, unless otherwise specified (repetition rate 1 kHz). Spectra were obtained by dispersing the SFG light onto a CCD camera [24], and averaging for typically 200 s. The pulses, focused down to a ~0.4 mm beam waist, were incident at a 65° angle with respect to the surface normal.

---

[1]1-palmitoyl-2-[12-[(7-nitro-2,1,3-benzoxadiazol-4-yl)amino]dodecanoyl]-sn-glycero-3-phosphocholine

5.3 Sum frequency generation and fluorescence microscopy

Fig. 5.1 depicts the lateral pressure of a DPPC monolayer as a function of average surface area (A) per molecule, known to reflect the existence of several phases [57, 58, 59]: a condensed phase at high compression (molecular area $A < 47Å^2$/molecule), a liquid condensed (LC) phase, coexisting with the liquid expanded (LE) phase between ~50 and ~85 $Å^2$/molecule, and the LE phase for $A>80Å^2$/molecule. At much higher surface areas ($A \geq 400Å^2$/molecule), there exists an additional gas (G) phase [57].

Figure 5.2: SFG spectra (gray lines) obtained at different polarization conditions (the three letter code next to the spectra indicates polarizations for SFG, VIS and IR, respectively), in combination with the fluorescence microscopy image (50μm×50μm) for a compressed DPPC layer (47 $Å^2$). Spectra with pss polarization were also recorded (not shown) and found to be indistinguishable from the sps spectra. Black lines are fits as described in the text. In the bottom trace the signal from a bare water surface for ppp-combination is depicted, reflecting the IR pulse bandwidth.

Fig. 5.2 depicts three sets of spectra for the compressed layer (47 $Å^2$/molecule) at different polarization combinations (s or p) of the SFG, VIS and IR light, respectively, indicated in the graph. The absence of signal for other polarization combinations (apart from pss, which is identical to sps) establishes that the surface is isotropic around its azimuth [21] (see Appendix A). The fluorescence microscopy image (see the inset) shows a single, dense phase.

The SFG spectra $I_0(\omega)$ can be reproduced very well by an expression for the second-order nonlinear susceptibility consisting of a frequency independent nonresonant term $\chi_{NR}^{(2)}$ and a frequency dependent resonant term $\chi_{RES}^{(2)}$. The resonant contribution is composed of all the vibrational modes ($\chi_n^{(2)}$) that are excited by

the infrared field. As the line width of the visible pulse is comparable to the width of the vibrational resonances a convolution is necessary to accurately describe the intensity [8]:

$$\chi^{(2)} = \chi^{(2)}_{NR} + \chi^{(2)}_{RES} = A_0 e^{i\phi} + \sum_n \frac{A_n}{\omega - \omega_{0n} + i\Gamma_{0n}}$$

$$I_0(\omega) \propto |A_0 e^{i\phi} + \sum_n \int_{-\infty}^{\infty} \chi^{(2)}_n(\omega') E_1(\omega' - \omega) d\omega'|^2, \tag{5.1}$$

where the vibrational resonances are described by their resonance frequencies ω_{0n}, line widths $2\Gamma_{0n}$ and amplitudes A_n. A_0 is the amplitude of the non-resonant susceptibility and ϕ its phase relative to the vibrational resonances.

For the strongly compressed DPPC layer (47 Å^2/molecule), the three spectra require three resonances, well-established for terminal CH_3 groups: the symmetric stretch at 2878 cm^{-1}, the asymmetric stretch at 2963 cm^{-1}, and a Fermi resonance at 2938 cm^{-1}. Clearly, there are no observed resonances of the methylene (CH_2) stretch vibrations. As discussed in Chapter 1 and Appendix A sum frequency generation is inherently sensitive only to media lacking inversion symmetry [49]. The alkyl strands of the DPPC molecule consist of an even number of C atoms and consequently an even number of CH_2 groups. As can be seen form the molecular model displayed in the inset of Fig. 5.1, for a fully stretched alkyl chain each C-C bond has a local inversion symmetry center. This establishes once more (see e.g. [61, 62, 63, 9]) that the compressed DPPC layer consists of fully stretched alkyl chains. As can be seen in Fig. 5.3, upon decompression
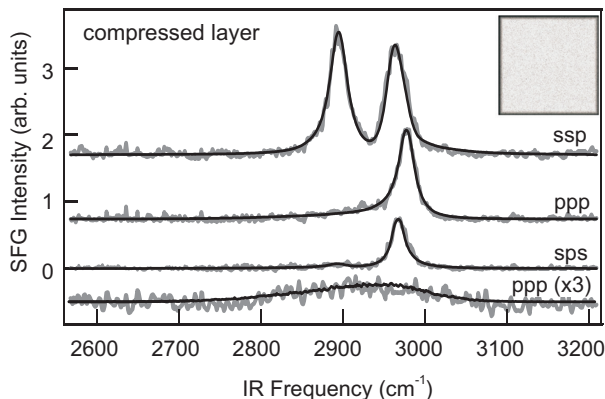

Figure 5.3: SFG spectra (gray lines) obtained at different polarization conditions (the three letter code next to the spectra indicates polarizations for SFG, VIS and IR, respectively), in combination with the fluorescence microscopy image (50μm×50μm) for a liquid condensed DPPC layer (58 Å^2).

of the layer to 58 Å^2/molecule, the two CH_2 resonances appear at ~2850 and

~2920 cm^{-1}. This indicates that the alkyl chains are no longer perfectly stretched (in agreement with previous measurements [9]). The fluorescence images show the breakup of the layer into islands of high density (white areas) and low density (dark areas). Fig. 5.4 shows SFG spectra for a further decompressed layer to 65 Å^2/molecu-le. It shows that the spectrum is dominated by the CH$_2$ modes, whereas the CH$_3$ modes are almost completely absent. Both observations are testimony of increase in the disorder in the monolayer. The relation between the amount of (dis)order and the shape of the SFG spectra will be the topic of section 5.5. The fluorescence image confirms that at lower densities there is a clear coexistence of the liquid condensed and liquid expanded phases [58, 59]. The fits
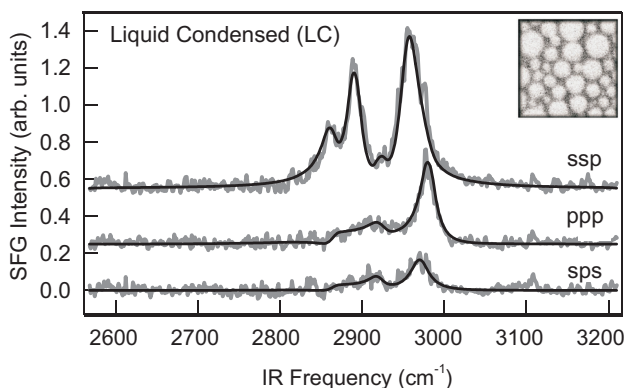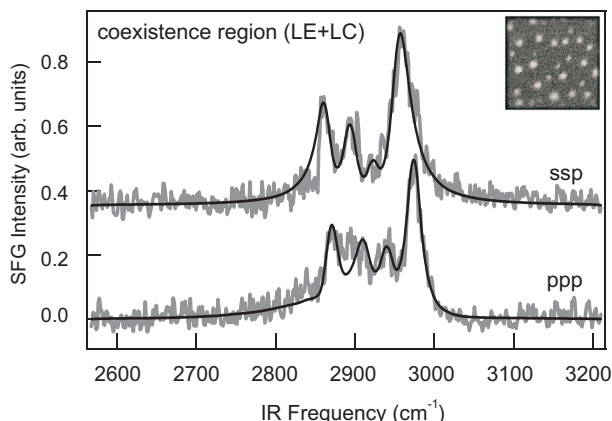

Figure 5.4: SFG spectra (gray lines) obtained at different polarization conditions (the three letter code next to the spectra indicates polarizations for SFG, VIS and IR, respectively), in combination with the fluorescence microscopy images (50μm×50μm) for the coexistence region of DPPC layer (65 Å^2).

were obtained under the global constraint of fixed frequencies for the transitions, with line widths varying in the range Γ=4.5-7 cm^{-1}. A fully stretched (all-trans[2]) DPPC molecule, as depicted in Fig. 5.1, has two independent alkyl chains. The local symmetry axes of both methyl (CH$_3$) end groups are under a relative angle of ~7º. We can neglect this small angular difference and treat the DPPC molecule as two uncorrelated alkyl chains[3]. By comparing the amplitude of the $\chi^{(2)}_{\alpha\beta\gamma}$ (α, β, γ=s or p) of the CH$_3$ C–H stretching mode for the different polarization combinations, as described in detail in Ref. [21] and summarized in Appendix A, we can deduce the orientation of the chains as well as the depolarization ratio

---

[2]This means that the C-C chain lies in one plane and refers to the eclipsed conformation of an alkyl chain as defined in [64]. The use of the terminology 'cis' and 'trans' should be restricted to unsaturated in-plane bonds but has been used in the context of ordered and disorder alkyl chains in the past by many others (see e.g. [9, 65]). To remain consistent we will continue applying this (incorrect) terminology.

[3]This seems valid, since we have established that the surface is azimuthally isotropic.

r. Required in the fit procedure are the Fresnel coefficients ($\mathcal{L}(\omega_i)$), that can be calculated from the angles of incidence and the complex (frequency dependent) refractive indices of air (n_1), water (n_2) and the interface layer (n_1'). The refractive indices for the three beams are set as $n_1 = 1$ and $n_1' = 1.18$ [21] for all beams; $n_2^{IR} = 1.39 + 0.013i$; $n_2^{VIS} = 1.326 + 1.3 \times 10^{-7}i$ and $n_2^{SFG} = 1.331$.

For the fully compressed phase (47 Å^2/molecule, Fig. 5.2), we find an angle between the transition dipole moment of the methyl (CH$_3$) stretch mode and the surface normal (θ) of $31° < \theta < 47°$, (with $1.6 < r < 2.6$, in good agreement with the previously reported value of 2.3 [21, 66]). This implies that the molecular axis lies along the surface normal, as one would expect for the highly compressed phase [57]. In the decompression region the angle θ increases to 53°, indicating that the molecules now – on average – make an angle of $\sim 20°$ with the surface normal. From the spectra at 65 Å^2/molecule (Fig. 5.4) no orientation could be deduced.

5.4   A new phase transition

Now we can use sum frequency generation and fluorescence microscopy to obtain a more detailed understanding of the phase behavior of DPPC. Starting at very low densities (A $\geq$ 110 Å^2/molecule) we can compress the layer and monitor spectral changes (see Fig. 5.5). At very low densities no resonant signal is observed in the C–H stretch region. Compression of the layer leads to the sudden appearance of two resonances around 2850 and 2920 cm^{-1}, associated mainly with CH$_2$-moieties in the disordered alkyl chain (although some contribution from the CH$_3$ groups cannot be excluded; to obtain sufficient signal-to-noise the spectral resolution in this set of experiments is 40 cm^{-1}). These two peaks can be reproducibly 'switched on and off' (without significant hysteresis) by very slight re- and de-compression, where the system must be allowed to equilibrate for some ~20 seconds. Note that the change in surface coverage between the presence and the absence of the signal is less than 1%. The numbers next to the spectra (in parentheses) denote the order in which the spectra were recorded in this particular run. There is a surprisingly sharp and sudden change in the signal (also observed under ppp-polarization conditions) as a function of molecular surface area.
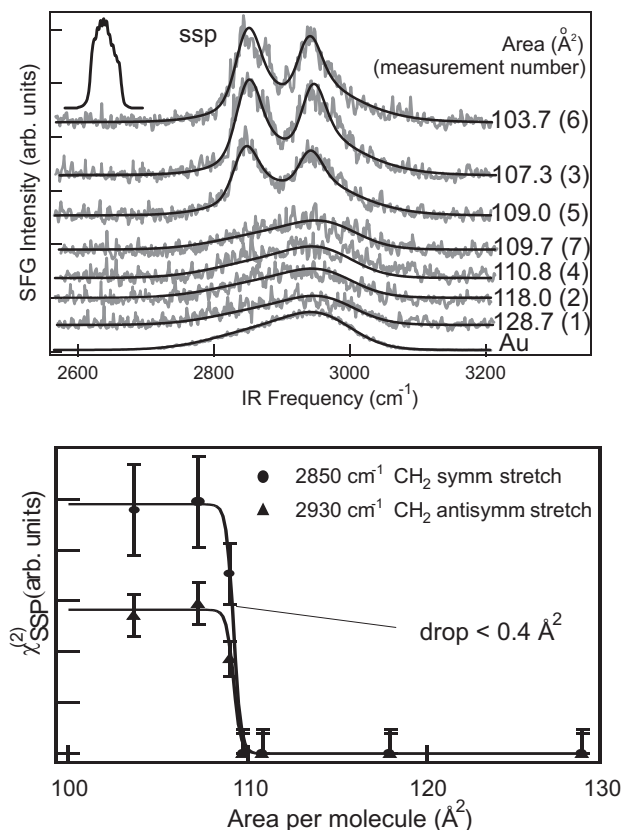
Figure 5.5: Top: SFG spectra (grey lines) upon compression of the DPPC monolayer starting at very low densities using an infrared pulse energy of 3 μJ. It also depicts the SFG signal from a gold (Au) surface, to demonstrate the non-resonant nature of the signal for $A > 109.0\,\text{Å}^2/$molecule. Black lines are fits as described in the text. The spectral profile of the visible upconversion pulse is depicted in the upper left corner. Bottom panel: Amplitudes for the second-order susceptibilities for different vibrations obtained from the fits shown in the left panels. Absolute values for the area per molecule may vary by 7%, but the relative values on the x-axis are reliable within 0.5%. Lines in this panel are guides to the eye.

This anomalous behavior – the disappearance of SFG signal for constant surface coverage of alkyl chains – has been observed previously for a surfactant adsorbed to quartz [65], at a coverage comparable to where the transition is observed here: at twice the surface area relative to fully compressed. In these experiments [65], the surface was in contact with solvents of varying polarity. As apolar solvent molecules interact with the alkyl chains, chain-chain interactions increase, causing a lengthening and straightening out of the alkyl chains. In contrast, po-

lar solvents were observed to cause a curling up of the chains, due to repulsive solvent-chain interactions; by curling up, the apolar alkyl chain can reduce its exposure to the polar environment. At the same time this can result in restoration of (averaged) in-chain inversion symmetry, causing the SFG signal to disappear. In the case of DPPC, the relative importance of the water-chain interactions is increased as the coverage is decreased, and, apparently, there is a very clear point at which the chain-water interactions supersede the chain-chain interactions, resulting in a sudden, conjunct coiling of the chains. As can be observed in the right hand side of Fig. 5.5, the width of the transition is less than 0.4 Å^2/molecule (the fitted line results in a width of 0.2 Å^2/molecule). The narrow range over which the transition occurs can be understood by noting that, if for one chain (i.e. locally) the chain-water interactions exceed the chain-chain interactions and this chain curls up, its neighbor will experience less chain-chain stabilization, causing it to curl up as well. As a result of this avalanche process, the transition is very sharp. As such, the observed transition cannot be the LE-G transition, which is known to exhibit a very large coexistence region. SFG is insensitive to first order phase transitions with coexistence regions, such as the LE-G and the LE-LC transition, since the onset of coexistence initially affects only a small fraction of the molecules (and the SFG signal originates from the majority). Indeed, although the LE-LC transition can be observed in detail using fluorescence microscopy, SFG is insensitive to it (as can be seen from Fig. 5.7). Inversely, the molecular transition observed here with SFG does not result in microscopic changes, such as domain formation, and it remains undetected using fluorescence microscopy. The two techniques thus provide complementary information.

Similar observations (a sudden increase in the nonlinear response in the region of the phase diagram where the surface tension is still very close to zero and constant) have been made in second harmonic generation (SHG) nonlinear spectroscopic studies on Langmuir films [67, 68, 69]. This fact, together with the otherwise typical behavior of DPPC as a surfactant [57], indicate that this observation of a molecular coiled-uncoiled transition is relevant to a wider range of Langmuir- and Langmuir-Blodgett systems.

5.4.1 Heating effect

To investigate the effect of absorbed infrared pulse energy by the water surface on the observed phase transition we have monitored the point at which the phase transition occurs as a function of pulse power. The result is plotted in Fig. 5.6. It shows that for high laser power the transition occurs at lower molecular areas, indicating that some heating effect is present. For lower energy the molecular area converges to a constant value of $115 \pm 3\text{\AA}^2$/molecule. Thus, the observed phase transition (in Fig. 5.5) is not caused by laser heating effects. Also, we have changed the laser power by variation of the focus size by a factor of two. The observed shift in the transition area was only dependent on the total pulse power. Changing the repetition rate over a factor of ten, while preserving the DC power did not alter the observed value for given pulse power, indicating that the deviation is caused by steady state heating.
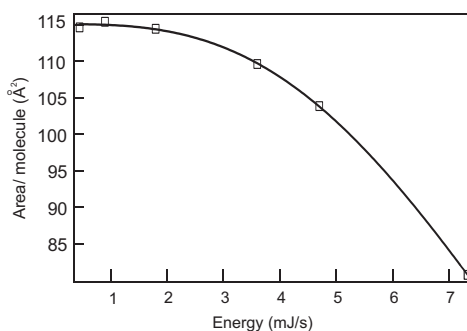
Figure 5.6: Heating effect. The observed molecular area for which the phase transition occurred as a function of pulse power. The drawn line is a guide for the eye.

5.5 Order-disorder transition

As shown briefly in section 5.3, at lower surface densities, going from the condensed phase to the coexistence region, there is a decrease in order in the alkyl chains that can be monitored by comparing the amplitude of the methyl (CH_3) and methylene (CH_2) stretching modes. Fig. 5.7 (from top to bottom), shows a series of SFG spectra (in ssp polarization) at various decreasing densities. It demonstrates that, (with decreasing density) the CH_3 peaks rapidly lose in intensity, whereas the CH_2 intensity remains constant over the entire coexistence region.

The bottom panel of Fig. 5.7 shows the amplitudes of the symmetric methyl (CH_3) and methylene (CH_2) stretching modes. With decreasing density (increasing surface area), the amplitude of the CH_3 symmetric stretch (ω=2878 cm^{-1})

decreases much more rapidly than expected from the number of molecules, due to rapid onset of disorder: the signal is largest when all the dipoles are aligned. In contrast, for the CH_2 symmetric stretch (2850 cm^{-1}), the amplitude rises steeply with surface area due to the onset of disorder to level off at 55 Å^2/molecule, and remain at this value until the signal abruptly disappears (at 109 Å^2/molecule, as shown in Fig. 5.5).
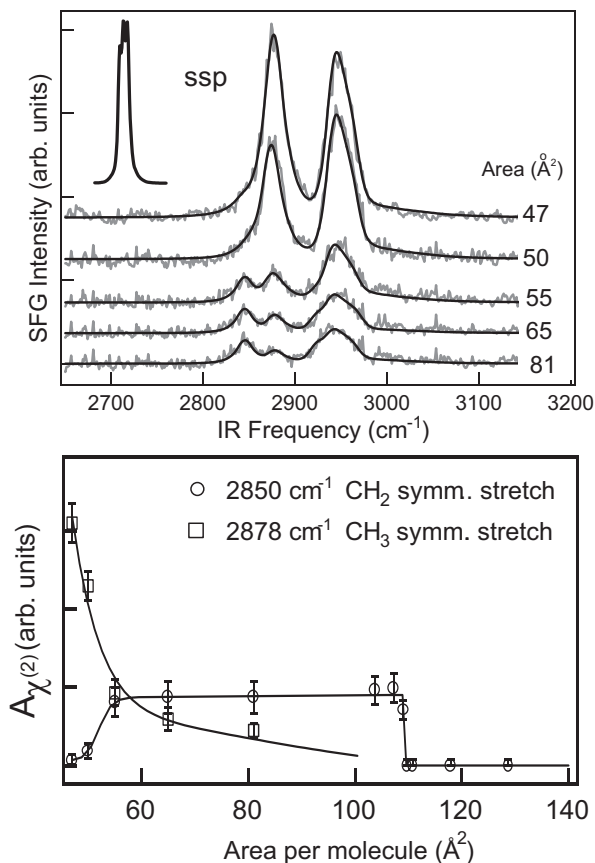
Figure 5.7: Top panel: SFG spectra (grey lines) upon compression of the DPPC monolayer. Black lines are fits as described in the text. The spectral profile of the upconversion pulse is depicted in the upper left corner. Bottom panel: Amplitudes for the second-order susceptibilities for different vibrations obtained from the fits shown in the left panels. Lines in this panel are guides to the eye.

Despite the change in phospholipid concentration by almost a factor of 2, which results in a decrease of the number of molecules in the focus, there is no change in the SFG intensity associated with the methylene (CH_2) stretching mode. The rapid decrease in CH_3 intensity is related to the onset of orientational

disorder, which apparently sets in early in the decompression. The equally fast appearance of the CH_2 resonances reveals the underlying cause of this disorder: the presence of defects within the alkyl chains. It is clear that an appropriate model should provide a simultaneous description of these two closely related observations. The SFG signal is determined in a complex manner by the transition dipole moment, the Raman tensor and the distribution of molecules. As both vibrational modes are symmetric the Raman tensor has only two independent non-vanishing elements, whose ratio (the hyperpolarizability ratio r) can be considered a constant and independent of chain orientation [70]. The variation in the observed SFG intensity can be traced back to a change in the average transition dipole moment (**P**). As a coherent process, SFG is particularly sensitive to the preferential alignment of surface dipoles that must add up coherently to produce a macroscopic polarization.

In our calculation, this order parameter represents the average number of chain defects in both phospholipid phases in the coexistence region, as we have not attempted to separate the contributions from the individual phases. Starting from one C atom at the surface each chain is constructed atom by atom. The angle of each new bond is determined by choosing a random number between 0 and 1 and comparing it to the value of p. For values smaller (larger) than p the angle between the plane holding atoms C_i, C_{i+1}, C_{i+2} and the plane holding atoms C_{i+1}, C_{i+2} C_{i+3} is chosen such that the bond is in an all-trans (random) conformation. Knowing all the positions of all the atoms the transition dipole moment for the symmetric methyl (CH_3) and methylene (CH_2) stretch modes can be calculated. The probability of chain defects[4] then becomes $(1 - p)$. The restriction that chains cannot penetrate the water surface is also applied. The angle of the first CH_2 group is determined by the distribution of initial angles (θ_s) with respect to the surface normal. It is a Gaussian distribution with a standard deviation σ.

We can calculate the SFG intensity with a simple Monte Carlo procedure in order to qualitatively explain the behavior of phospholipids in the coexistence region. We can use the average transition dipole moment as a measure of SFG intensity and calculate it for a sufficiently large ensemble of molecules (~2500) as a function of average chain orientation and the number of defects in each chain. The number of chain defects can be modeled by introducing an in-chain order parameter (p), which is the probability that a C-C bond is in an all-trans conformation: If $p = 1$ the alkyl chain is in all-trans conformation and if $p = 0$ all C-C bonds are oriented randomly.

---

[4]Chain defect is used here to denote any conformation that is not eclipsed. Usually the term "gauche defect" is used, but this can be misleading as it is originally meant to denote a single conformation and not any conformation that is different from the eclipsed conformation.
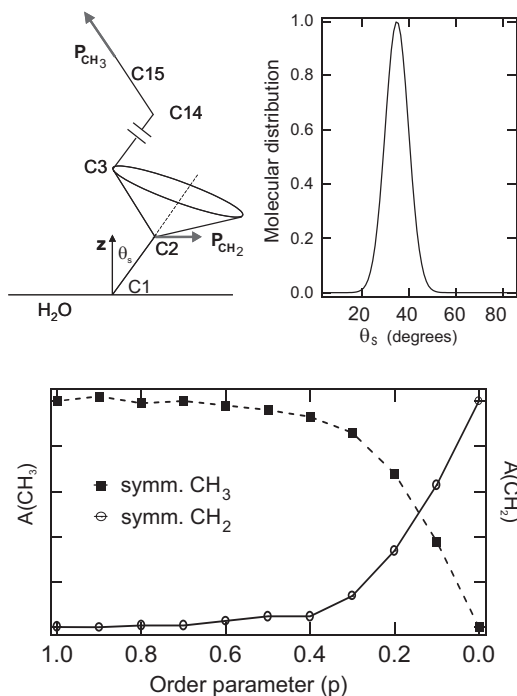
Figure 5.8: Upper panel: Illustration of the model to calculate the amplitude of the ensemble transition dipole moment. The C-C bonds are constructed one by one for an azimuthally isotropic interface, with a Gaussian angular distribution. Lower panel: Calculation of the amplitude as a function of order parameter for an ensemble having an initial surface angle, $\theta_s = 35.25°$ and a distribution $\sigma = 7°$.

As shown in Fig. 5.8, our model has four parameters: The orientation of the backbone of the alkyl chains (represented by θ_s, which is the angle between the first C-C bond and the surface normal), its distribution (σ), the surface density and the number of chain defects (represented by p). The lower panel of Fig. 5.8 shows a calculation of the amplitude of the symmetric CH_2 and CH_3 stretch vibrations, for an initially stretched alkyl chain oriented along the surface normal. As the order decreases the intensity of the symmetric CH_3 stretch vibration decreases, partly because the density decreases, but more so because the CH_3 groups lose their preferential orientation. In the end, no net orientation exists, which results in a vanishing average transition dipole moment and, consequently, the absence of SFG intensity. For the CH_2 groups the effect is reversed as the inversion symmetry that is present initially is lifted and the polarizations of the adjacent CH_2 groups no longer interfere destructively. From the analysis of SFG spectra taken at different polarization combinations (section 5.3), we can estimate aver-

age values for θ_s and σ. As the area is known, the only adjustable parameter that remains is the order parameter p. We can use this model to describe the amplitude of the measured CH_2 and CH_3 symmetrical stretch modes. For a given area and average orientation (both obtained from the SFG spectra) we can reproduce the amplitude ratio of both vibrational modes by appropriate adjustment of the order parameter. The results are shown in the upper panel of Fig. 5.9.
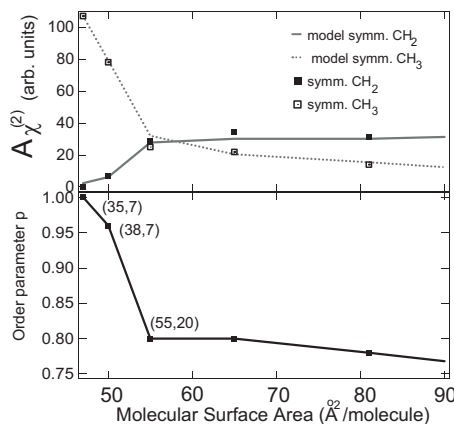
Figure 5.9: Upper panel: Amplitudes for the nonlinear susceptibilities of the symmetrical CH_3 and CH_2 stretch vibration (obtained from the fits in Fig. 5.7). The lines are fits using the Monte Carlo model as described in the text. Lower panel: The obtained order parameter as a function of molecular surface area. The average orientation and its distribution are given in parenthesis (θ_s, σ).

Tilt angles and distributions are given in parenthesis. From the polarization-dependent spectra at 65 Å^2/molecule and 81 Å^2/molecule no net orientation could be deduced. Hence for these points the angular distribution was unweighed. In the lower panel the derived order parameter is plotted, which clearly shows that with increasing area the order in the chains decreases, resulting in a dramatic change in the amplitude. The order need not drop dramatically, however. To maintain a constant CH_2 amplitude only 28 percent of the C atoms needs to be constructed randomly, which means that averaged over both the liquid expanded and liquid condensed phase four carbon atoms per chain have no preferential orientation.

5.6   Conclusions

Using SFG we observe, for the first time, a very sharp transition from a phase with curled alkyl chains to a phase with spatially extended chains. This transition, occurring at relatively low DPPC densities, cannot be observed with fluorescence

microscopy and is not accompanied by significant changes in surface pressure. We have analyzed the order and orientation of the alkyl chains in the condensed and coexistence regions of the phase diagram by calculating the SFG intensity as a function of alkyl chain density. By introducing an order parameter we are able to reproduce the dramatic change in the SFG intensity as a function of phospholipid density.

Chapter 6

Sum frequency generation scattering

A novel application of vibrational Sum Frequency Generation (SFG) is developed to study the molecular properties of the surface of sub-micron particles in suspension. The Rayleigh-Gans-Debye scattering theory is extended to extract the local molecular response from the macroscopic nonlinearly scattered spectral intensity. These results demonstrate the use of vibrational SFG to investigate quantitatively the surface molecular properties of sub-micron particles of varying sizes, dispersed in solution. It provides information on the order and density of alkyl chains and allows us to determine the elements of the local second-order surface susceptibility.

6.1   Introduction

Second-order nonlinear optical spectroscopies have become well-established and versatile tools to investigate planar interfaces, because of their sensitivity to broken inversion symmetry. Particularly vibrational Sum Frequency Generation (SFG) has emerged as an important technique in surface studies, owing to its molecular surface specificity [5, 8, 49, 63, 71, 72]. It allows one to e.g. determine the orientation and molecular order of molecules constituting biological membranes and Langmuir-Blodgett films [9, 21, 65, 66, 73, 74]. Ideally, one would want to enjoy the advantages of SFG to obtain information on non-planar local surfaces of e.g. liposomes and cells. Although the inherent macroscopic inversion symmetry in these media seems to exclude the application of SFG to such systems, recent experimental [75, 76] and theoretical [77] reports of second harmonic generation provide good prospects. In addition, reflection sum frequency experiments have been successfully performed on strongly corrugated surfaces comprised of micron-sized powdered crystalline particles [78], 15 nm gold nano-particles deposited on water and silicon/air interfaces [79] and 200 nm latex beads at the air/liquid, and air/solid interface [80]. These observations suggest that it should, in principle, be possible to probe the usually weak vibrational modes of molecules on the surface of sub-micron particles in a dilute suspension.

In the first part of this Chapter it is demonstrated that SFG can be used to study the interface of sub-micron particles in suspension. As a model system we use a suspension of silica particles covered with alkyl chains anchored by one end to the sphere. We obtain information on the molecular order and density of the molecules at the surface by analyzing both the vibrational response and the angle dependent scattered intensity, as a function of polarization of the incident and emitted fields. The Rayleigh-Gans-Debye scattering theory is further developed to extract local second-order nonlinear susceptibility elements from the macroscopic scattered spectral intensity. The results demonstrate the possibility of using vibrational SFG to investigate the molecular properties of the non-planar surface of sub-micron particles dispersed in a solution.

6.2   Experimental

The SFG experiments were performed using 10 µJ (120 fs) infrared (IR) pulses (repetition rate 1 kHz, FWHM bandwidth of ~180 cm^{-1}) centered around 2900 cm^{-1} and 3.0 µJ, 800 nm visible (VIS) pulses with a 10 cm^{-1} bandwidth. A schematic representation of the experimental geometry can be found in Fig. 6.1 (left panel). The selectively polarized IR and VIS pulses were incident under a relative angle of 15° (β) and focused down to a ~0.4 mm beamwaist. The scattered light was collimated with a lens, polarization selected and dispersed onto an intensified charge coupled device (CCD) camera [23, 24]. Typical recording times were ~600 s. The angular resolution was controlled by an aperture placed

in front of the collimating lens and was typically 12°.
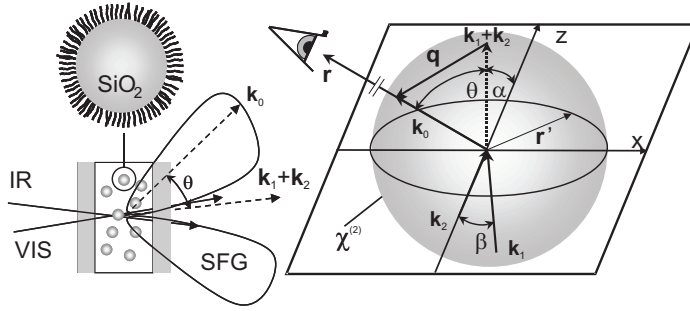
Figure 6.1: Left panel: The experimental geometry, with a schematic illustration of one particle. Right panel: The scattering geometry. $\mathbf{k_2}$ is the wave vector of the infrared field, $\mathbf{k_1}$ is the wave vector of the visible field, $\mathbf{k_0} = k_0\hat{\mathbf{n}}$ is the wave vector of the scattered sum frequency field, $\mathbf{q}$ is the scattering wave vector, $\mathbf{r} = r\hat{\mathbf{n}}$ is the detector position, θ is the scattering angle (in solution) and $\mathbf{r}'$ is a point on the surface of the sphere, whose center is chosen as the origin. All $\mathbf{k}$ vectors and $\mathbf{r}$ lie in the horizontal x-z plane. The infrared, visible and sum frequency fields are either polarized parallel (p) or perpendicular (s) to the scattering plane.

The samples consist of dry stearic alcohol ($C_{18}H_{37}OH$) coated [81] silica particles [82] dispersed in CCl_4 (99.9%, Baker Analyzed) with radii (σ) of 342 nm, 123 nm, and 69 nm. The colloid volume fractions where, respectively 5 % (σ=342 nm $\pm$ 36 nm), 4 % (σ=123 nm $\pm$ 11 nm) and 6.7 % (σ=69 nm $\pm$ 7.1 nm). The sample cell consists of 2 CaF_2 plates separated by a 1 mm teflon spacer. The particle size distribution was determined from an analysis of Transmission Electron Microscopy (TEM) images containing several hundred colloids (see Fig. 6.2 for a TEM image of the 342 nm particles). Before each measurement the samples were put in an ultrasonic bath for several minutes, to minimize the number of aggregates. Spectra were recorded on short time scales (1 s) so that it was possible to check for aggregates (which can appear at small scattering angles and have a disproportionally large signal compared to single particles) and –if present– remove their contribution from the data.

6.3   Results

Fig. 6.2 shows four SFG spectra recorded with different polarization combinations denoted in the graph, at a scattering angle (θ) of 22º.
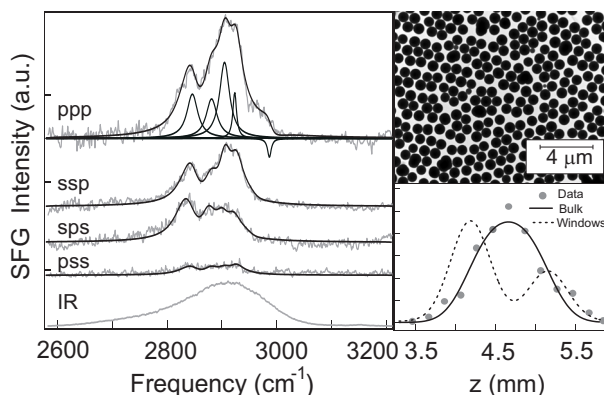
Figure 6.2: Left panel: SFG spectra (grey lines) and fits (black lines) obtained at different polarization conditions (the three letter codes next to the spectra indicate (p for horizontal, s for vertical) polarizations for SFG, VIS and IR, respectively) at a scattering angle of 22°. The angular resolution was 12°. The intensities are corrected for polarization dependent detector sensitivity. The black lines are fits as described in the text. The solid lines in the upper trace (ppp) represent the squared IR amplitude functions used in the fitting procedure with the sign indicating the relative phase. The bottom trace depicts an SFG spectrum from a gold surface, which reflects the IR pulse bandwidth. Top right: TEM image of the colloids. Bottom right: Integrated SFG intensity as a function of sample position. The solid (dashed) line represents the calculated signal if the signal was to originate from colloids in the suspension (adsorbed to the windows).

To ascertain that the signal originates from the colloids in suspension and not from those adsorbed to the sample window, we have measured the total SFG intensity as a function of sample position along the z axis (shown in the bottom right). The solid line is a calculation assuming signal originating from the colloids in the suspension and the dashed line represents the case of signal originating from colloids adsorbed to the walls. Clearly, the measured intensity originates from the particles in the suspension. That the signal does not originate from a macroscopic interface is further corroborated by the observation that no signal could be detected in the macroscopic phase matched direction (along $\mathbf{k}_1 + \mathbf{k}_2$). The signal vanishes upon replacing the suspension with pure CCl_4. No signal was observed for polarization combinations other than indicated in the graph.

To obtain meaningful information from these spectra we describe the generated sum frequency field in terms of the local components of the second-order nonlinear surface susceptibility, $\chi^{(2)}$, for each vibrational mode. As the colloid surfaces can be considered locally isotropic [15], there are four non-zero elements of $\chi^{(2)}$ (for each mode): $\chi^{(2)}_{\perp\perp\perp}$, $\chi^{(2)}_{\perp\parallel\parallel}$, $\chi^{(2)}_{\parallel\perp\parallel}$ and $\chi^{(2)}_{\parallel\parallel\perp}$ contributing to the second-order nonlinear polarization at the surface of the sphere, $\mathbf{P}^{(2)}_0(\mathbf{r}')$ [$\perp$ ($\parallel$) refers to the direction perpendicular (parallel) to the local surface normal]. $\mathbf{P}^{(2)}_0$ is a function of the local infrared $\mathbf{E}_2$ and visible $\mathbf{E}_1$ fields:

$$\mathbf{P}^{(2)}_0(\mathbf{r}') = \sum_n \chi^{(2)}_n : \mathbf{E}_1(\mathbf{r}')\mathbf{E}_2(\mathbf{r}'), \tag{6.1}$$

where n refers to the different vibrational modes. For dilute suspensions the total scattered intensity is the incoherent sum of the intensities scattered by the individual colloids [83]. We can describe the scattering field outside one spherical particle as a function of scattering angle (θ) by solving the wave equation (with the local second-order nonlinear polarization as source term) using a Green's function method following [84]:

$$\mathbf{E}_0(\mathbf{r}) = \frac{1}{\epsilon}\nabla \times \nabla \times \oint d^2\mathbf{r}' \frac{e^{ik_0|\mathbf{r}-\mathbf{r}'|}}{|\mathbf{r}-\mathbf{r}'|}\mathbf{P}^{(2)}_0(\mathbf{r}'), \tag{6.2}$$

in which $\mathbf{k}_0$ is the scattering wave vector, ϵ the dielectric constant of the solvent, $\mathbf{r} = r\hat{\mathbf{n}}$ the position of the detector and $\mathbf{r}'$ the local coordinate at the surface of the sphere ($|\mathbf{r}'|=\sigma$). By integrating over the surface of the sphere, the phase relation between light generated at different parts of the sphere is fully taken into account in the analysis. As detection occurs in the far field we can safely assume that $\sigma \ll r$. We can now approximate $|\mathbf{r}-\mathbf{r}'|$ by $r - \hat{\mathbf{n}}\mathbf{r}'$. This simplifies Eq. 6.2 to:

$$\mathbf{E}_0(\mathbf{r}) = \frac{e^{ik_0 r}}{\epsilon r}\nabla \times \nabla \times \oint d^2\mathbf{r}' e^{ik_0\hat{\mathbf{n}}\mathbf{r}'}\mathbf{P}^{(2)}_0(\mathbf{r}'). \tag{6.3}$$

Noting that in the far field we can also assume that $\nabla\frac{e^{ik_0 r}}{r} \simeq \frac{ik e^{ik_0 r}}{r}\nabla r = \frac{ik e^{ik_0 r}}{r}\hat{\mathbf{n}}$ Eq. 6.3 becomes:

$$\mathbf{E}_0(\mathbf{r}) = -\frac{e^{ik_0 r}}{\epsilon r}\hat{\mathbf{n}} \times \hat{\mathbf{n}} \times \oint d^2\mathbf{r}' e^{ik_0\hat{\mathbf{n}}\mathbf{r}'}\mathbf{P}^{(2)}_0(\mathbf{r}'). \tag{6.4}$$

Since the refractive indices of the solvent and the particle are almost identical (n_{CCl_4}=1.4579 [85] and n_{SiO_2}=1.42, as determined from linear optical measurements at 645 nm), we can use the Rayleigh-Gans-Debye (RGD) approximation [76, 75], which treats the electric fields inside and outside the sphere as identical [84]. Inserting Eq. 6.1 and using for the electrical fields, $\mathbf{E}^{(2)}_i(\mathbf{r}') = \mathcal{E}_i e^{ik_i\mathbf{r}'}\mathbf{u}_i$, Eq. 6.4 becomes:

$$\mathbf{E}_0(r) = -\mathcal{E}_2\mathcal{E}_1 k_0^2 \frac{e^{ik_0 r}}{\epsilon r}\hat{\mathbf{n}} \times \{\hat{\mathbf{n}} \times \oint d^2\mathbf{r}' e^{i\mathbf{q}\cdot\mathbf{r}'}(\sum_\gamma(\sum_{\alpha,\beta}\chi^{(2)}_{\gamma\alpha\beta}(\mathbf{e}_\alpha\cdot\mathbf{u}_1)(\mathbf{e}_\beta\cdot\mathbf{u}_2)\mathbf{e}_\gamma))\}. \tag{6.5}$$

In the above expression $\chi^{(2)}_{\gamma\alpha\beta}$ are the elements of the local second-order non-linear surface susceptibility. $\mathbf{e}_{\alpha,\beta,\gamma}$ correspond to the unit vectors of the local (spherical) coordinate system with unit vectors $(e_{r'}, e_{\theta'}, e_{\phi'})$, $\mathbf{u}_{1,2}$ are the unit polarization vectors of the incoming infrared and visible beams, $\mathbf{k}_0 = k_0\hat{\mathbf{n}}$ is the wave vector of the scattered SFG field, and $\mathbf{q}$ is the scattering wave vector, defined as $\mathbf{k}_1 + \mathbf{k}_2 - \mathbf{k}_0 = q\hat{\mathbf{q}} = 2k_0\sin\frac{\theta}{2}\hat{\mathbf{q}}$. The double outer product ensures that only transverse components of the scattered field are calculated. The unit polarization vectors are independent of the spherical coordinates and by applying an appropriate contraction [86] we can write:

$$\mathbf{E}_0(r) = -\mathcal{E}_2\mathcal{E}_1 k_0^2 \frac{e^{ik_0 r}}{\epsilon r}\hat{\mathbf{n}}\times\{\hat{\mathbf{n}}\times(\mathbf{u}_1\cdot\oint d^2\mathbf{r}' e^{i\mathbf{q}\cdot\mathbf{r}'}(\sum_{\gamma}(\sum_{\alpha,\beta}\chi^{(2)}_{\gamma\alpha\beta}(\mathbf{e}_\alpha\mathbf{e}_\gamma\mathbf{e}_\beta))\cdot\mathbf{u}_2)\}. \quad (6.6)$$

Eq. 6.5 can be solved analytically by rotating the (x,y,z) axis system (in which the polarization directions of the incoming beams are written) around the y axis, such that they become aligned with $\mathbf{q}$.

For the case of ppp polarization the transverse scattered field from a single sphere can be calculated from Eq. 6.6 to be:

$$E_0(r) = -\mathcal{E}_2\mathcal{E}_1 k_0^2 \frac{e^{ik_0 r}}{2\epsilon r}\times$$
$$\{\cos\frac{\theta}{2}[(\Gamma^{(2)}_{\perp\perp\perp} + \Gamma^{(2)}_{\perp\|\|})\cos\beta + (\Gamma^{(2)}_{\perp\perp\perp} - \Gamma^{(2)}_{\perp\|\|})\cos(\theta - \beta + 2\alpha)] - \quad (6.7)$$
$$\sin\frac{\theta}{2}[(\Gamma^{(2)}_{\|\|\perp} - \Gamma^{(2)}_{\|\perp\|})\sin\beta + (\Gamma^{(2)}_{\|\perp\|} + \Gamma^{(2)}_{\|\|\perp})\sin(\theta - \beta + 2\alpha)]\},$$

where $\Gamma^{(2)}_{iii}$ is a function of the local second-order susceptibility elements and the experimental parameters σ and θ as defined in Table 6.1. It is insightful to express the nonlinearly scattered sum frequency field in terms of an effective nonlinear susceptibility of a single sphere, $\Gamma^{(2)}$, because it allows us to describe the nonlinear surface scattering from one sphere at a particular angle in a way similar to conventional sum frequency generation from a planar surface (this approach will be exploited in Chapter 7). Corresponding expressions for the other polarization combinations can also be derived. Of the eight possible polarization combinations only four expressions remain non-zero: ppp, ssp, sps, and pss (shown in Fig. 6.2). Eq. 6.7 reduces to the results reported earlier [75, 76] for second harmonic scattering if $\chi^{(2)}$ is dominated by the radial component (i.e. $\chi^{(2)}=0$, except for $\chi^{(2)}_{\perp\perp\perp}$). From Eq. 6.7 it is clear that for a given scattering angle the transverse component of $\mathbf{E}_0$ is a linear combination of the components of the effective nonlinear spherical susceptibility $\Gamma^{(2)}$. This is equivalent to the description of SFG from a planar interface [16]. Hence, we can still model the spectra using the familiar expressions for SFG [8, 5, 74]:

$$\mathbf{E}_0 \propto \sum_n \Gamma^{(2)}_n : \mathbf{E}_2\mathbf{E}_1 \qquad \Gamma^{(2)}_n(\omega) = \frac{A_n}{(\omega - \omega_{0n}) + i\Upsilon_n}, \qquad (6.8)$$

Table 6.1: Values of the elements of the effective second-order susceptibility $\Gamma^{(2)}$ in terms of the local susceptibilities $\chi^{(2)}$ and experimental observables, θ and σ.

$\Gamma^{(2)}_{\perp\perp\perp}$	$2\pi(B\chi^{(2)}_{\perp\perp\perp} + A(\chi^{(2)}_{\perp\|\|} + \chi^{(2)}_{\|\perp\|} + \chi^{(2)}_{\|\|\perp}))$
$\Gamma^{(2)}_{\perp\|\|}$	$\pi(A\chi^{(2)}_{\perp\perp\perp} + (A+2B)\chi^{(2)}_{\perp\|\|} - A(\chi^{(2)}_{\|\perp\|} + \chi^{(2)}_{\|\|\perp}))$
$\Gamma^{(2)}_{\|\perp\|}$	$\pi(A(\chi^{(2)}_{\perp\perp\perp} - \chi^{(2)}_{\perp\|\|}) + (A+2B)\chi^{(2)}_{\|\perp\|} - A\chi^{(2)}_{\|\|\perp})$
$\Gamma^{(2)}_{\|\|\perp}$	$\pi(A(\chi^{(2)}_{\perp\perp\perp} - \chi^{(2)}_{\perp\|\|}) - A\chi^{(2)}_{\|\perp\|} + (A+2B)\chi^{(2)}_{\|\|\perp})$
A	$\frac{6i}{q^4\sigma^2}\{2(1 - \frac{q^2\sigma^2}{3})\sin(q\sigma) - 2q\sigma\cos(q\sigma)\}$
B	$\frac{6i}{q^4\sigma^2}\{(q^2\sigma^2 - 2)\sin(q\sigma) - q\sigma(\frac{q^2\sigma^3}{3} - 2)\cos(q\sigma)\}$

where n refers to a vibrational mode, ω_{0n} is the resonance frequency and Υ_n the spectral half width at half maximum. The solid lines in Fig. 6.2 are fits to the data using the convolution of $\Gamma^{(2)}_n$ with the electric field envelope of the upconversion pulse:

$$I_0(\omega) \propt |\sum_n \int_{-\infty}^{\infty} \Gamma^{(2)}_n(\omega')E_1(\omega' - \omega)d\omega'|^2. \qquad (6.9)$$

The fits were obtained using all five well-known CH stretch resonances [21]: the symmetric CH_3 and CH_2 stretches at 2890 cm^{-1} and 2853 cm^{-1}, the asymmetric CH_3 and CH_2 stretches at 2980 cm^{-1} and 2910 cm^{-1} and a Fermi resonance at 2930 cm^{-1}. The central frequencies were obtained from a linear infrared spectrum and a Raman spectrum of the same colloid sample. For planar surfaces it is well-established that alkyl chains in an ordered all-trans conformation possess inversion symmetry around the CH_2 groups, which, as a consequence, do not appear in the sum frequency spectrum [9, 63, 72, 74]. As the CH_2 group distances are very small compared to the particle dimensions, this selection rule still applies for colloidal particles and therefore we can conclude from the relatively strong contribution from the CH_2 groups to the spectrum that the stearyl chains are not well-ordered on the surface. If we compare this to a structure of a Langmuir film the structure must be an open one with gauche defects in the alkyl chains, much like the uncompressed liquid expanded phase of a phospholipid monolayer [74].
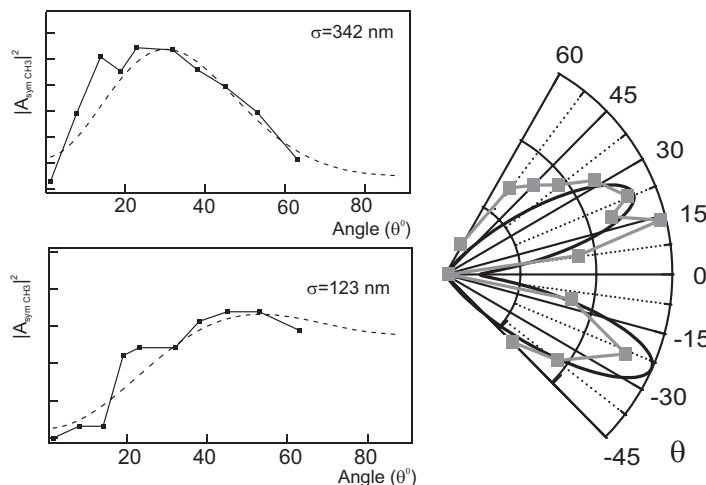
Figure 6.3: Left panel: The angular distribution of SFG intensity for the symmetrical CH$_3$ stretch mode for silica particles with σ=342 nm (top panel) and σ=123 nm (bottom panel). Right panel: Polar plot of the angular distribution of SFG intensity for the symmetrical CH$_3$ stretch mode for silica particles with a radius of 342 nm. The dashed lines are fits to the data using Eq. (6.7).

Fig. 6.3 shows the scattered intensity for the symmetrical CH$_3$ stretch vibration ($|A_{\text{sym.CH}_3}|^2$) of the stearyl groups attached to the surface of the 342 nm and the 123 nm particles as a function of the scattering angle θ (left panel) as well as a polar plot for the 342 nm particles (right panel). Similar to previous theoretical [77] and experimental [75] results for SHG scattering, the sum frequency signal vanishes in the forward direction (i.e., at $\theta = 0$) in agreement with Eq. 6.5. The solid line represents the calculated emitted power ($\frac{\mathrm{d}P}{\mathrm{d}\Omega} = \frac{cr^2\sqrt{\epsilon}}{2\pi}|\mathbf{E}_0|^2$) over a solid angle ($\Omega$) of 12°. The fits result in amplitudes of the local surface susceptibility for this mode of $\chi^{(2)}_{\perp\|\|}/\chi^{(2)}_{\perp\perp\perp}$=-0.29, $\chi^{(2)}_{\|\perp\|}/\chi^{(2)}_{\perp\perp\perp}$=0.28 and $\chi^{(2)}_{\|\|\perp}/\chi^{(2)}_{\perp\perp\perp}$=0.32. With these parameters the intensity ratio of the different polarization combinations as presented in Fig. 6.2 can be reproduced very well.

As can be seen from Eqs. 6.7 and Table 6.1 the scattered intensity depends strongly on the particle size. Fig. 6.4 shows SFG spectra of stearyl-coated silica particles with radii of 69 nm, 123 nm and 342 nm respectively as well as the angle dependent intensity for these radii as calculated using Eq. 6.7, with the parameters obtained from the angle dependent fits in Fig. 6.3. Only two (ppp and ssp) polarization combinations are shown (top panel). The intensity ratio is very well reproduced by the RGD theory as witnessed by the bottom panel.
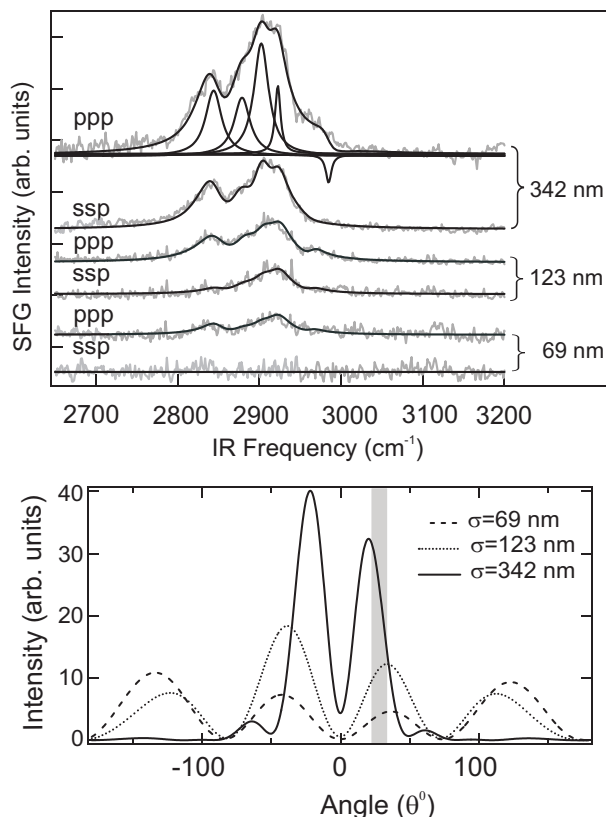
Figure 6.4: Top panel: SFG spectra (grey lines) and fits (black lines) obtained at different polarization conditions (the three letter codes next to the spectra indicate polarizations (p for horizontal, s for vertical with respect to the plane of incidence for SFG, VIS and IR, respectively) at a scattering angle of 26°. The angular resolution was 12°. The intensities are corrected for polarization dependent detector sensitivity. The solid lines are fits as described in the text. Bottom panel: Calculated intensities as a function of scattering angle. The shaded area indicates the angle for which the spectra in the top panel have been recorded.

This shows that for sub-micron sized particles the RGD approach is well suited to describe the experimental results and allows for an accurate estimate of the relative magnitudes of the different elements of the local nonlinear susceptibility. The applicability of the RGD approximation will be discussed in more detail in then next Chapter.

6.4   Conclusions

To summarize this Chapter, we have measured vibrational sum frequency spectra for a dispersion of sub-micron sized particles covered with alkane chains. By analyzing the results using the Rayleigh-Gans-Debye approximation we obtain information about the local molecular order and density of these chains on the surface of the particle. This extension of SFG to non-planar surfaces demonstrates that this technique with its inherent molecular surface sensitivity can now be applied to a wider range of systems. This opens new avenues for the in-situ research of the surfaces of e.g. cells, vesicles, particles and related systems.

Chapter 7

Nonlinear optical scattering: the concept of an effective susceptibility

We present a general theoretical method for deriving effective susceptibilities for (non)-linear optical scattering processes of arbitrary order using the reciprocity principle. This method allows us to formulate a generalized treatment of nonlinear optical scattering and deduce selection rules independent of the precise mechanism of light-matter interaction. We particularize this approach to second-order sum frequency scattering from an inhomogeneous medium and consider the limiting cases of small particle scattering, refractive index matched (Rayleigh-Gans-Debye) scattering, small refractive index contrast (Wentzel-Kramers-Brillouin) scattering and correlated scattering.

7.1   Introduction

Several theoretical studies have been performed with the aim of modeling the radiation emitted in a nonlinear scattering event. These studies include the work described in the previous Chapter, second harmonic scattering from small dielectric [77, 87] and metallic [88, 89] spheres, from an ordered lattice [76] and from a small metallic hemispherical boss [90]. All of these investigations are aimed at finding a model for second harmonic or sum frequency generation scattering from a typical –mostly spherical– particle shape. No description exists of a general scattering event of arbitrary order from an arbitrary shaped particle.

In this Chapter, we introduce the concept of effective susceptibility for a (non)linear scattering event of arbitrary (n-th) order from the reciprocity principle, which provides a general theoretical framework for nonlinear-optical scattering. This enables us to derive selection rules for different experimental geometries based on symmetry arguments alone. We then consider different limiting cases of sum frequency generation (SFG) scattering. In particular we will consider small particle scattering, index matched (nonlinear Rayleigh-Gans-Debye) scattering, small index contrast (nonlinear Wentzel-Kramers-Brillouin) scattering and correlated scattering. Finally, we will compare the results of the nonlinear Rayleigh-Gans-Debye (RGD) and Wentzel-Kramers-Brillouin (WKB) approximations.

7.2   Theory

The nonlinear response of a material to incident electro-magnetic waves is usually described in terms of the nonlinear polarization. The polarization is related to the incoming field(s) by the nonlinear susceptibility $\overset{\leftrightarrow}{\chi}$. Consequently, the susceptibility is a measure of how much polarization is built up in the medium by the incident fields. The incoming fields are considered to be composed of monochromatic plane waves of the form:

$$\mathbf{E}_\alpha^{\mathbf{k}}(\mathbf{r}, t) = \mathcal{E} \mathbf{u}_\alpha e^{i(\mathbf{k} \cdot \mathbf{r} - \omega t)}, \qquad (7.1)$$

with $\mathcal{E}$ the scalar amplitude of the wave and $\mathbf{u}_\alpha$ the unit polarization vector (α denotes the polarization state). This description of the incident fields in terms of plane waves limits the further applicability to beams with a low intensity gradient in the beam waist, i.e. excludes tightly focused pulses as in Ref. [91, 92]. As the fields interact with the medium, there are two effects that modify the build-up of the local nonlinear polarization: a microscopic local field correction due to dipole-dipole interactions, and a change in the average macroscopic field due to the linear optical properties of the medium (see [90] and references therein). The first can be taken into account by the local Lorentz-Lorenz correction [93], which we will not take into account in this description (but can readily be done). The latter can be implemented by using Fresnel type coefficients $\overset{\rightarrow}{\mathcal{L}}_\alpha(\mathbf{r})$, which

describe the modification of the local field by the particle (note that far from the particle $\vec{\mathcal{L}}_\alpha(\mathbf{r}) \to \mathbf{u}_\alpha$), so that the local field becomes:

$$\mathbf{E}_\alpha^\mathbf{k}(\mathbf{r}, t) = \mathcal{E}_\alpha^\mathbf{k}\vec{\mathcal{L}}_\alpha(\mathbf{r})e^{i(\mathbf{k}\cdot\mathbf{r}-\omega t)}. \tag{7.2}$$

The most general form of the non-locally-induced nonlinear polarization reads as [16]:

$$\mathbf{P}^{\omega_0=\omega_1+...+\omega_n}(\mathbf{r}) = \int ... \int \overset{\leftrightarrow}{\chi}(\mathbf{r}, \mathbf{r}_1, ..., \mathbf{r}_n) \cdot \mathbf{E}^{\omega_1}(\mathbf{r}_1) \\ ... \cdot \mathbf{E}^{\omega_n}(\mathbf{r}_n)\, d^3\mathbf{r}_1 ... d^3\mathbf{r}_n, \tag{7.3}$$

which also includes any possible interaction with the magnetic field of the optical waves [94]. In particular, this allows us to set the optical magnetic permeability $\mu(\omega) \equiv 1$ without loss of generality in the following. In addition to assuming plane waves, we also restrict ourselves to detection in the far field. No other restriction (e.g., on the nature of light-matter interaction) is assumed in this section.

7.2.1 Reciprocity

Consider two different current sources $\mathbf{j}_I(\mathbf{r})$ and $\mathbf{j}_{II}(\mathbf{r})$ emitting optical fields $\mathbf{E}_I$ and $\mathbf{E}_{II}$ at a single frequency. Then the relationship between the currents $\mathbf{j}_{I,II}$ and the fields $\mathbf{E}_{I,II}$ is given by the following relation [94]:

$$\int \mathbf{j}_I(\mathbf{r}) \cdot \mathbf{E}_{II}(\mathbf{r})d^3\mathbf{r} = \int \mathbf{j}_{II}(\mathbf{r}) \cdot \mathbf{E}_I^\dagger(\mathbf{r})d^3\mathbf{r}, \tag{7.4}$$

where the integrals are taken over the volumes of the sources and the † denotes that all non-reciprocal interactions must be reversed in the calculation of the radiated field $\mathbf{E}_I^\dagger(\mathbf{r})$ (see Ref. [95]). Eq. (7.4) is known as the reciprocity theorem and is one of the basic concepts in physics. In linear optics reciprocity arises from the following (Onsager) symmetry of the linear susceptibility [95]:

$$\overset{\leftrightarrow}{\chi}_{ij}(\mathbf{r}, \mathbf{r}_1) = \overset{\leftrightarrow}{\chi}{}_{ji}^\dagger(\mathbf{r}_1, \mathbf{r}), \tag{7.5}$$

where $\overset{\leftrightarrow}{\chi}{}^\dagger$ is the susceptibility of the same medium after application of the time-inversion operation. The application of the time-inversion operation is relevant for example, in magnetic materials where it reverses the direction of the media's DC magnetization. In non-magnetic media, which can be described by a local dielectric response, this leads to a symmetric dielectric response tensor $\overset{\leftrightarrow}{\epsilon}_{ij}(\mathbf{r}) = \overset{\leftrightarrow}{\epsilon}_{ji}(\mathbf{r})$. Note that light absorption, which is an intrinsically non-reversible process, does not affect the reciprocity. The Onsager symmetry (Eq. (7.5)) yields a general relation between results of two experimental situations, in which the position of a monochromatic light source and a detector are exchanged [94, 95, 96, 97].
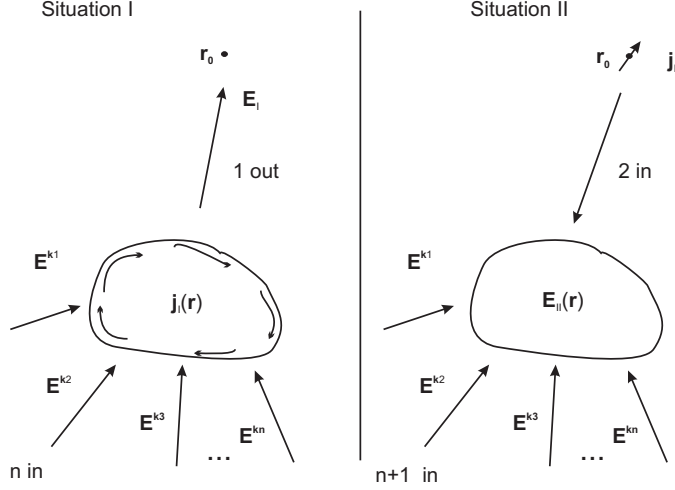
Figure 7.1: Two different current sources. Current source I is the scattering object (with the center of mass placed at the origin), in which the currents are induced by an n-th order nonlinear optical interaction. $\mathbf{E}_I$ is the field from the particle (indicated in the graph by "1 out") measured by a detector at $\mathbf{r}_0$. Current source II is a point dipole located at $\mathbf{r}_0$. $\mathbf{E}_{II}$ is the field emitted by the current source (indicated in the graph by "2 in") experienced by the particle.

As the current and polarization are related by $\mathbf{j} = \frac{\partial}{\partial t}\mathbf{P}$, the reciprocity theorem can be used to describe (non)linear-optical scattering from a particle. One can consider the two situations that are sketched in Fig. 7.1. In the first we are dealing with a current source ($\mathbf{j}_I$) induced in the scattering particle by an n-th order nonlinear optical interaction with n incoming waves that emits a field $\mathbf{E}_I$ which is detected at position $\mathbf{r}_0$. In the second situation we are dealing with a dipolar point source located at $\mathbf{r}_0$ having a current $\mathbf{j}_{II}$ ($\sim \delta(\mathbf{r}-\mathbf{r}_0)$) that induces a field $\mathbf{E}_{II}$ in the particle. Assuming that the detector is placed in the Fraunhofer zone (i.e. the far field), the wave incident from the detector (or current source) on the particle can be treated as a plane wave. Knowing the relation between $\mathbf{j}_{II}$ and the distribution of the local field $\mathbf{E}_{II}(\mathbf{r})$ it induces in the particle, we can employ the reciprocity theorem, Eq. (7.4), to evaluate the field $\mathbf{E}_I$ at the detector position, which can have two orthogonal polarization components. To calculate its amplitude $\mathcal{E}^{\mathbf{k}_0}_{\alpha_0}$ in a given polarization state α_0, one has to choose the direction of $\mathbf{j}_{II}$ along the polarization vector. Here $\mathbf{k}_0$ denotes the wave vector of the wave scattered into the direction of the detector. The result can be written in the form:

$$\mathcal{E}^{\mathbf{k}_0}_{\alpha_0} = e^{ik_0 r_0}\frac{k_0^2}{r_0}\Gamma^{\mathbf{k}_0,\mathbf{k}_1,\ldots,\mathbf{k}_n}_{\alpha_0,\alpha_1,\ldots,\alpha_n}\,\mathcal{E}^{\mathbf{k}_0}_{\alpha_0}\mathcal{E}^{\mathbf{k}_1}_{\alpha_1}\cdots\mathcal{E}^{\mathbf{k}_n}_{\alpha_n}. \tag{7.6}$$

Here $\alpha_1,\ldots,\alpha_n$ and $\mathbf{k}_1,\ldots,\mathbf{k}_n$ denote the polarization state and the wave vectors

of the incident plane waves and

$$\Gamma_{\alpha_0,\alpha_1,\ldots,\alpha_n}^{\mathbf{k}_0,\mathbf{k}_1,\ldots,\mathbf{k}_n} = \iint \ldots \int \vec{\mathcal{L}}_{\alpha_0}^{-\mathbf{k}_0,\dagger}(\mathbf{r}) \cdot \overleftrightarrow{\chi}(\mathbf{r},\mathbf{r}_1,\ldots,\mathbf{r}_n)$$
$$\cdot \vec{\mathcal{L}}_{\alpha_1}^{\mathbf{k}_1}(\mathbf{r}_1) \ldots \cdot \vec{\mathcal{L}}_{\alpha_n}^{\mathbf{k}_n}(\mathbf{r}_n) \, e^{i(-\mathbf{k}_0\cdot\mathbf{r}+\mathbf{k}_1\cdot\mathbf{r}_1\ldots\mathbf{k}_n\cdot\mathbf{r}_n)} \, d^3\mathbf{r}\, d^3\mathbf{r}_1 \ldots d^3\mathbf{r}_n, \tag{7.7}$$

which can be interpreted as an effective nonlinear polarizability of the scattering object. It is analogous to atomic or molecular polarizability, which is often introduced to describe the nonlinear-optical interactions in e.g. gases with an exception that $\Gamma_{\alpha_0,\alpha_1,\ldots,\alpha_n}^{\mathbf{k}_0,\mathbf{k}_1,\ldots,\mathbf{k}_n}$ is not only a property of the scattering object, but also depends on the experimental geometry via the wave vectors $\mathbf{k}_0, \mathbf{k}_1, \ldots, \mathbf{k}_n$ of the interacting waves. In its essence, this treatment replaces an extended scattering object, which could have any complex internal structure with any nature of internal nonlinear interaction, by a simple point object with dipole nonlinear polarizability given by Eq. (7.7) that creates exactly the same scattered field at the position of the detector for a given experimental configuration.

Thus, the reciprocity theorem allows us to re-formulate the problem in a way that is symmetric with respect to the incident and outgoing fields. This intrinsic symmetry of Eq. (7.7) ensures reciprocity on the level of the field scattered by the whole particle. One can also show that this symmetry is needed in non-absorbing systems to ensure energy conservation and the Manley-Rowe relations [33] requiring that equal amount of photons are emitted into or absorbed from each interacting wave.

7.2.2 Symmetry

In nonlinear optics one often applies symmetry arguments on the level of the susceptibility $\overleftrightarrow{\chi}$. The effective susceptibility presented in Eq. (7.7) is an integrated quantity, which is not a function of the scattering object alone, but also depends on the experimental geometry via the wave vectors $\mathbf{k}_i$. Still, one can apply the symmetry operations to the whole scattering geometry [98]. Thus, particle symmetry (like e.g. inversion symmetry) is no longer the sole factor of relevance. This allows us to directly formulate selection rules for different scattering events, independent of the mechanisms of linear- and nonlinear-light-matter interactions.

For example, when using a planar geometry, (i.e. all incident and scattered beams lie within one (scattering) plane), the polarization direction of the waves parallel (perpendicular) to that plane are defined as p (s). If the particle is symmetric with respect to the scattering plane, then, upon reflection in the symmetry plane all p-polarized waves and $\overleftrightarrow{\chi}$ remain unchanged, whereas the s-polarized waves change phase by a factor of π. The induced polarization should be the same for both cases. Hence for all n-th order scattering processes all elements of $\overleftrightarrow{\Gamma}_{\alpha_0,\alpha_1,\ldots,\alpha_n}^{\mathbf{k}_0,\mathbf{k}_1,\ldots,\mathbf{k}_n}$ with an odd number of s-polarized waves must equal 0. Thus, in the case of in-plane second-order scattering, for example, there are only four

allowed elements of $\overset{\leftrightarrow}{\Gamma}{}^{\mathbf{k}_0,\mathbf{k}_1,\mathbf{k}_2}_{\alpha_0,\alpha_1,\alpha_2}$ (ppp, ssp, sps and pss). Analogously, for third-order scattering there are only 8 allowed elements of $\overset{\leftrightarrow}{\Gamma}{}^{\mathbf{k}_0,\mathbf{k}_1,\mathbf{k}_2,\mathbf{k}_3}_{\alpha_0,\alpha_1,\alpha_2,\alpha_3}$, (ssss, pppp, sspp, ppss, spsp, psps, pssp and spps). For situations with an additional 2-fold rotational symmetry (which is the case in higher harmonic scattering, when detection is in the forward, or backward direction) no even-harmonic scattering can occur as the only allowed elements must have both an even number of s and p polarized waves. This is a well-known phenomena in x-ray generation from noble gasses were only odd numbers of the fundamental frequency are generated. This symmetry is broken if one uses non-colinear input waves of different frequencies (which occurs for example in infrared-visible sum frequency generation).

7.3 Sum frequency generation scattering

The solutions to Eqs. (7.6) and (7.7) for the scattered fields depend on the order of the scattering event and on possible simplifications imposed by the symmetry of the geometry. In the following description we focus on second-order scattering processes. For dielectric and metallic *spherical* particles an exact treatment (Mie theory) exists for second harmonic scattering, in which the amplitude of the scattered wave is expressed as a set of absolutely converging series of complex terms, which involve spherical harmonics and Bessel functions of increasing order [77, 88]. For the special case of second-order sum frequency scattering the effective susceptibility (Eq. 7.7) becomes:

$$\Gamma^{\mathbf{k}_0,\mathbf{k}_1,\mathbf{k}_2}_{\alpha_0,\alpha_1,\alpha_2} = \int \vec{\mathcal{L}}^{-\mathbf{k}_0,\dagger}_{\alpha_0}(\mathbf{r}) \cdot \overset{\leftrightarrow}{\chi}(\mathbf{r},\mathbf{r}_1,\mathbf{r}_2) \cdot \vec{\mathcal{L}}^{\mathbf{k}_1}_{\alpha_1}(\mathbf{r}_1)$$
$$\cdot \vec{\mathcal{L}}^{\mathbf{k}_2}_{\alpha_2}(\mathbf{r}_2) e^{i(-\mathbf{k}_0\cdot\mathbf{r}+\mathbf{k}_1\cdot\mathbf{r}_1+\mathbf{k}_2\cdot\mathbf{r}_2)} d^3\mathbf{r}\,d^3\mathbf{r}_1\,d^3\mathbf{r}_2. \tag{7.8}$$

We will use this expression as a starting point for sum frequency scattering from small particles (section 7.3.1). In sections 7.3.2 and 7.3.3 we will implement approximations that are generally employed in nonlinear surface spectroscopy.

7.3.1 Small particles

To consider the scattering from small particles (with typical size dimension σ) we decompose the local-field factors into even and odd parts as:

$$\vec{\mathcal{L}}^{\mathbf{k}}_{\alpha}(\mathbf{r}) = \vec{\mathcal{L}}^{\mathbf{k},\text{even}}_{\alpha}(\mathbf{r}) + \vec{\mathcal{L}}^{\mathbf{k},\text{odd}}_{\alpha}(\mathbf{r}), \tag{7.9}$$

where

$$\vec{\mathcal{L}}^{\mathbf{k},\text{even}}_{\alpha}(\mathbf{r}) \equiv \frac{1}{2}\left(\vec{\mathcal{L}}^{\mathbf{k}}_{\alpha}(\mathbf{r}) + \vec{\mathcal{L}}^{-\mathbf{k}}_{\alpha}(\mathbf{r})\right) \tag{7.10}$$

$$\vec{\mathcal{L}}^{\mathbf{k},\text{odd}}_{\alpha}(\mathbf{r}) \equiv \frac{1}{2}\left(\vec{\mathcal{L}}^{\mathbf{k}}_{\alpha}(\mathbf{r}) - \vec{\mathcal{L}}^{-\mathbf{k}}_{\alpha}(\mathbf{r})\right), \tag{7.11}$$

where $\vec{\mathcal{L}}_\alpha^{\mathbf{k}}$ and $\vec{\mathcal{L}}_\alpha^{-\mathbf{k}}$ are the normalized local fields of the wave, propagating in the forward and backward directions.

The interactions are now split into a centrosymmetric (Eq. 7.10) and an anti-centrosymmetric part (Eq. 7.11). Expanded in powers of σ/λ, the lowest order contribution to $\vec{\mathcal{L}}_\alpha^{\mathbf{k},\text{even}}(\mathbf{r})$ comes from $(\frac{\sigma}{\lambda})^0$. Likewise $\vec{\mathcal{L}}_\alpha^{\mathbf{k},\text{odd}}(\mathbf{r})$, is determined by $(\frac{\sigma}{\lambda})^1$.

If we expand the phase factors in Eq. (7.7) as well, we can decompose the effective susceptibility (Eq. (7.7)) in powers of σ/λ. The zeroth-order contains all even parts of the local field:

$$\Gamma_{\alpha_0,\alpha_1,\alpha_2}^{\mathbf{k}_0,\mathbf{k}_1,\mathbf{k}_2} = \int \vec{\mathcal{L}}_{\alpha_0}^{\mathbf{k}_0,\text{even},\dagger} \cdot \overset{\leftrightarrow}{\chi}(\mathbf{r},\mathbf{r}_1,\mathbf{r}_2) \cdot \vec{\mathcal{L}}_{\alpha_1}^{\mathbf{k}_1,\text{even}}(\mathbf{r}_1) \cdot \vec{\mathcal{L}}_{\alpha_2}^{\mathbf{k}_2,\text{even}}(\mathbf{r}_2) d^3\mathbf{r}\, d^3\mathbf{r}_1 d^3\mathbf{r}_2 \quad (7.12)$$

The next order in (σ/λ) is obtained by expanding the phase factor in Eq. (7.8) or by using the odd part for one of the local fields yielding:

$$\Gamma_{\alpha_0,\alpha_1,\alpha_2}^{\mathbf{k}_0,\mathbf{k}_1,\mathbf{k}_2} = \int \vec{\mathcal{L}}_{\alpha_0}^{-\mathbf{k}_0,\text{even},\dagger}(\mathbf{r}) \cdot \overset{\leftrightarrow}{\chi}(\mathbf{r},\mathbf{r}_1,\mathbf{r}_2) \cdot \vec{\mathcal{L}}_{\alpha_1}^{\mathbf{k}_1,\text{even}}(\mathbf{r}_1) \cdot \vec{\mathcal{L}}_{\alpha_2}^{\mathbf{k}_2,\text{odd}}(\mathbf{r}_2)\, d^3\mathbf{r}\, d^3\mathbf{r}_1 d^3\mathbf{r}_2$$

$$+ \int \vec{\mathcal{L}}_{\alpha_0}^{-\mathbf{k}_0,\text{even},\dagger}(\mathbf{r}) \cdot \overset{\leftrightarrow}{\chi}(\mathbf{r},\mathbf{r}_1,\mathbf{r}_2) \cdot \vec{\mathcal{L}}_{\alpha_1}^{\mathbf{k}_1,\text{odd}}(\mathbf{r}_1) \cdot \vec{\mathcal{L}}_{\alpha_2}^{\mathbf{k}_2,\text{even}}(\mathbf{r}_2)\, d^3\mathbf{r}\, d^3\mathbf{r}_1 d^3\mathbf{r}_2$$

$$+ \int \vec{\mathcal{L}}_{\alpha_0}^{-\mathbf{k}_0,\text{odd},\dagger}(\mathbf{r}) \cdot \overset{\leftrightarrow}{\chi}(\mathbf{r},\mathbf{r}_1,\mathbf{r}_2) \cdot \vec{\mathcal{L}}_{\alpha_1}^{\mathbf{k}_1,\text{even}}(\mathbf{r}_1) \cdot \vec{\mathcal{L}}_{\alpha_2}^{\mathbf{k}_2,\text{even}}(\mathbf{r}_2)\, d^3\mathbf{r}\, d^3\mathbf{r}_1 d^3\mathbf{r}_2 \quad (7.13)$$

$$+ i \int \vec{\mathcal{L}}_{\alpha_0}^{-\mathbf{k}_0,\text{even},\dagger}(\mathbf{r}) \cdot \overset{\leftrightarrow}{\chi}(\mathbf{r},\mathbf{r}_1,\mathbf{r}_2) \cdot \vec{\mathcal{L}}_{\alpha_1}^{\mathbf{k}_1,\text{even}}(\mathbf{r}_1) \cdot \vec{\mathcal{L}}_{\alpha_2}^{\mathbf{k}_2,\text{even}}(\mathbf{r}_2) \cdot (-\mathbf{k}_0 + \mathbf{k}_1 + \mathbf{k}_2)\, d^3\mathbf{r}\, d^3\mathbf{r}_1 d^3\mathbf{r}_2.$$

For a centrosymmetric particle we have upon inversion of the spatial coordinates:

$$\overset{\leftrightarrow}{\chi}(\mathbf{r},\mathbf{r}_1,\mathbf{r}_2) = -\overset{\leftrightarrow}{\chi}(-\mathbf{r},-\mathbf{r}_1,-\mathbf{r}_2) \quad (7.14)$$

and for the local fields we have upon inversion:

$$\vec{\mathcal{L}}_{\alpha_m}^{\mathbf{k},\text{even}}(\mathbf{r}_m) = \vec{\mathcal{L}}_{\alpha_m}^{-\mathbf{k},\text{even}}(-\mathbf{r}_m) = \vec{\mathcal{L}}_{\alpha_m}^{\mathbf{k},\text{even}}(-\mathbf{r}_m) \quad (7.15)$$

$$\vec{\mathcal{L}}_{\alpha_m}^{\mathbf{k},\text{odd}}(\mathbf{r}_m) = \vec{\mathcal{L}}_{\alpha_m}^{-\mathbf{k},\text{odd}}(-\mathbf{r}_m) = -\vec{\mathcal{L}}_{\alpha_m}^{\mathbf{k},\text{odd}}(-\mathbf{r}_m). \quad (7.16)$$

Thus, for all second-order (and other even-order) nonlinear processes the leading order contribution (Eq. (7.12)), vanishes since the contribution to the integral at $\{\mathbf{r},\mathbf{r}_1,\mathbf{r}_2\}$ is cancelled exactly by that at $\{-\mathbf{r},-\mathbf{r}_1,-\mathbf{r}_2\}$. The first non-vanishing terms are given by Eq. (7.13). For a non-centrosymmetric object (with a noncentrosymmetric shape or made of non-centrosymmetric material), Eq. (7.12) is the leading-order term.

In the limit of small scattering particles one can separate the properties of the scattering objects from the experimental geometry. In the zeroth-order approximation $\mathcal{L}_\alpha^{\mathbf{k},\text{even}}$ is given by the electrostatic ($\mathbf{k} \to 0$) approximation, which can be written as $\vec{\mathcal{L}}_\alpha^{\mathbf{k},\text{even}}(\mathbf{r}) \approx \overset{\leftrightarrow}{\mathcal{L}}_{\text{static}}(\mathbf{r}) \cdot \mathbf{u}_\alpha$ where $\overset{\leftrightarrow}{\mathcal{L}}_{\text{static}}(\mathbf{r})$ is a second-rank tensor. The

next term, linear in $\mathbf{k}$, leads to a non-zero contribution: $\vec{\mathcal{L}}_\alpha^{\mathbf{k},\text{odd}}(\mathbf{r}) \approx \overset{\leftrightarrow}{\mathcal{M}}(\mathbf{r}) : \mathbf{u}_\alpha \cdot \mathbf{k}$ where $\overset{\leftrightarrow}{\mathcal{M}}$ is a third-rank tensor.

This separates the experimental geometry (contained in $\mathbf{k}$ and $\mathbf{u}_\alpha$) from the particle properties in the field factors. The omitted terms are of second or higher order in (σ/λ), which can be neglected for small particles. For small particles we can expand $\Gamma_{\alpha_0,\alpha_1,\alpha_2}^{\mathbf{k}_0,\mathbf{k}_1,\mathbf{k}_2}$ as:

$$\Gamma_{\alpha_0,\alpha_1,\alpha_2}^{\mathbf{k}_0,\mathbf{k}_1,\mathbf{k}_2} \approx \overset{\leftrightarrow}{\Gamma}_\text{d} \cdot \mathbf{u}_{\alpha_0} \cdot \mathbf{u}_{\alpha_1} \cdot \mathbf{u}_{\alpha_2} + \overset{\leftrightarrow}{\Gamma}_\text{Q0} \cdot \mathbf{u}_{\alpha_0} \cdot \mathbf{k}_0 \cdot \mathbf{u}_{\alpha_1} \cdot \mathbf{u}_{\alpha_2}$$
$$+ \overset{\leftrightarrow}{\Gamma}_\text{Q1} \cdot \mathbf{u}_{\alpha_0} \cdot \mathbf{u}_{\alpha_1} \cdot \mathbf{k}_1 \cdot \mathbf{u}_{\alpha_2} + \overset{\leftrightarrow}{\Gamma}_\text{Q2} \cdot \mathbf{u}_{\alpha_0} \cdot \mathbf{u}_{\alpha_1} \cdot \mathbf{u}_{\alpha_2} \cdot \mathbf{k}_2, \qquad (7.17)$$

where the third-rank $\overset{\leftrightarrow}{\Gamma}_\text{d}$ and the forth-rank $\overset{\leftrightarrow}{\Gamma}_\text{Q}$ tensors describe the dipole (d) and quadrupole (Q) contributions and depend on the properties of the scattering object only. For SHG scattering from small spheres the above expression has been evaluated previously by Dadap et. al [77].

7.3.2   Index matched particles

In the following paragraphs we consider nonlinear index-matched Rayleigh-Gans-Debye (RGD) and small contrast Wentzel-Kramers-Brillouin (WKB) scattering. To do so, we shall restrict ourselves to a local form of the second-order susceptibility, i.e. $\overset{\leftrightarrow}{\chi}(\mathbf{r},\mathbf{r}_1,\mathbf{r}_2) = \chi^{(2)}(\mathbf{r})\delta(\mathbf{r}-\mathbf{r}_1)\delta(\mathbf{r}-\mathbf{r}_2)$. Furthermore, we shall assume that the scattering particles are made of centrosymmetric material so that $\chi^{(2)}(\mathbf{r})$ is non-vanishing only at the particle surface. These assumptions are very common in nonlinear surface spectroscopy [5]. Eq. (7.8) then takes the form of a surface integral:

$$\Gamma_{\alpha_0,\alpha_1,\alpha_2}^{(2)} = \oint \vec{\mathcal{L}}_{\alpha_0}^{-\mathbf{k}_0,\dagger}(\mathbf{r}) \cdot \chi^{(2)}(\mathbf{r}) \cdot \vec{\mathcal{L}}_{\alpha_1}^{\mathbf{k}_1}(\mathbf{r}) \cdot \vec{\mathcal{L}}_{\alpha_2}^{\mathbf{k}_2}(\mathbf{r}) e^{i(-\mathbf{k}_0+\mathbf{k}_1+\mathbf{k}_2)\cdot\mathbf{r}} \text{d}^2\mathbf{r}. \qquad (7.18)$$

Before considering the cases of index matched and small index contrast scattering, we remark that the optical fields in the vicinity of an interface can be strongly screened by the surface. The local-field factors $\vec{\mathcal{L}}_\alpha^{\mathbf{k}}$ depend on whether the fields are evaluated outside or inside the particle [90]. $\chi^{(2)}$ appearing in Eq. (7.18) is an effective integrated nonlinear susceptibility, which must include the surface screening effects (that are intrinsically non-local). Consequently, the values of the elements of $\chi^{(2)}$ depend on the definitions adopted. It is assumed in this work that the fields are evaluated at the outer side of the particle surface and the nonlinear source is located outside. Furthermore, Eq. (7.18) assumes that the curvature of the particle surface is small on the scale of the screening length so that the concept of the effective surface susceptibility [99] is applicable.

Eq. (7.18) can be evaluated if the local field factors $\vec{\mathcal{L}}_\alpha^{\mathbf{k}}$ are known. If the refractive index of the particle (n_p) and the surrounding medium (n_m) are matched, such that $|(\frac{n_p}{n_m} - 1)| \ll 1$, the local fields can be assumed to be identical to the

incoming fields. This approximation is known as the Rayleigh-Gans-Debye (RGD) approximation in which one can set $\vec{\mathcal{L}}_\alpha(\mathbf{r}) = \mathbf{u}_\alpha$.

The effective second-order polarizability can then be written as:

$$\Gamma^{(2)}_{\alpha_0,\alpha_1,\alpha_2}(\mathbf{q}) = \oint \mathbf{u}^{-\mathbf{k}_0,\dagger}_{\alpha_0}(\mathbf{r}) \cdot \chi^{(2)}(\mathbf{r}) \cdot \mathbf{u}^{\mathbf{k}_1}_{\alpha_1}(\mathbf{r}) \cdot \mathbf{u}^{\mathbf{k}_2}_{\alpha_2}(\mathbf{r}) e^{i\mathbf{q}\cdot\mathbf{r}} d^2\mathbf{r}, \qquad (7.19)$$

with $\mathbf{q} = -\mathbf{k}_0 + \mathbf{k}_1 + \mathbf{k}_2 = q\hat{\mathbf{q}}$ the scattering wave vector. For an arbitrary particle shape we can now find the scattered field, Eq. (7.6), in terms of $\Gamma^{(2)}$.

As mentioned in section 6.1, it is enlightening to draw an analogy between sum frequency scattering and conventional sum frequency generation from an (effective) planar surface [99]. We define this effective surface (lower panel of Fig. 7.2) to be orthogonal to the scattering wave vector $\mathbf{q}$ (illustrated in the top panel of Fig. 7.2). Thus, we can envisage the scattering particle as an effective surface with its normal (Z) parallel to $\mathbf{q}$. In sum frequency generation from a surface it is the interface that breaks the inversion symmetry, leading to a second-order nonlinear response. For a centrosymmetric index-matched particle it is the spatial variation of the phase factor $e^{i\mathbf{q}\cdot\mathbf{r}}$ that lifts the inversion symmetry. Further drawing upon this analogy, it is evident that $\Gamma^{(2)}$ is essentially the susceptibility of the effective surface. For a symmetric particle (similar to an isotropic surface) there are only four independent elements: $\Gamma^{(2)}_{\perp\perp\perp}$, $\Gamma^{(2)}_{\perp\|\|}$, $\Gamma^{(2)}_{\|\perp\|}$ and $\Gamma^{(2)}_{\|\|\perp}$, where $\perp$ refers to directions perpendicular to the effective surface (i.e. parallel to $\mathbf{q}$) and $\|$ refers to directions parallel to the effective surface. The solutions for the transverse scattered sum frequency fields become:

$$E_{ppp}(r) = -\mathcal{E}^{\omega_1}\mathcal{E}^{\omega_2}\frac{\omega^2 e^{ik_0 r}}{2c^2 r} \times$$
$$\{\cos\frac{\theta}{2}[(\Gamma^{(2)}_{\perp\perp\perp} + \Gamma^{(2)}_{\perp\|\|})\cos\beta + (\Gamma^{(2)}_{\perp\perp\perp} - \Gamma^{(2)}_{\perp\|\|})\cos(\theta - \beta + 2\alpha)] - \quad (7.20)$$
$$\sin\frac{\theta}{2}[(\Gamma^{(2)}_{\|\|\perp} - \Gamma^{(2)}_{\|\perp\|})\sin\beta + (\Gamma^{(2)}_{\|\perp\|} + \Gamma^{(2)}_{\|\|\perp})\sin(\theta - \beta + 2\alpha)]\}$$

$$E_{ssp}(r) = -\mathcal{E}^{\omega_1}\mathcal{E}^{\omega_2}\frac{\omega^2 e^{ik_0 r}}{2c^2 r}\Gamma^{(2)}_{\|\|\perp}\left(\cos\beta\cos\left(\frac{\theta}{2} + \alpha\right)\right.$$
$$\left. + \sin\beta\sin\left(\frac{\theta}{2} + \alpha\right)\right) \qquad (7.21)$$

$$E_{sps}(r) = -\mathcal{E}^{\omega_1}\mathcal{E}^{\omega_2}\frac{\omega^2 e^{ik_0 r}}{2c^2 r}\Gamma^{(2)}_{\|\perp\|}\cos\left(\frac{\theta}{2} + \alpha\right) \qquad (7.22)$$

$$E_{pss}(r) = -\mathcal{E}^{\omega_1}\mathcal{E}^{\omega_2}\frac{\omega^2 e^{ik_0 r}}{2c^2 r}\Gamma^{(2)}_{\perp\|\|}\cos\left(\frac{\theta}{2}\right) \qquad (7.23)$$

where θ is the scattering angle, α is the angle between $\mathbf{k}_2$ and $\mathbf{k}_1 + \mathbf{k}_2$, β is the angle between $\mathbf{k}_1$ and $\mathbf{k}_2$ and p (s) refers to polarization parallel (perpendicular) to the plane of incidence. Note that the expression in Eq. 7.20 is exactly the same
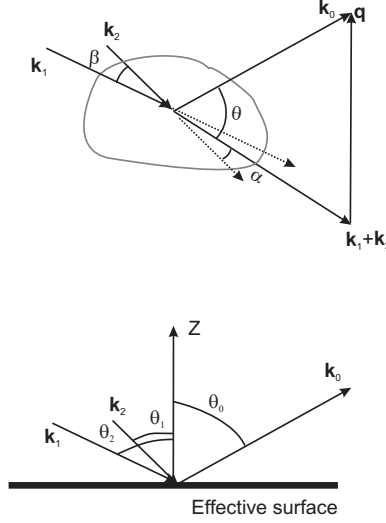
Figure 7.2: Illustration of the analogy between a sum frequency scattering experiment and a surface sum frequency experiment in reflection mode from a planar surface. Top panel: Scattering geometry with relevant parameters. Bottom panel: Surface analogy, in which the surface normal (Z) is parallel to **q**.

as that in Eq. 6.7. The difference lies in the methodology: In deriving Eq. 6.7 we start our calculation with the particle shape and the local surface properties and calculate all the components of the local surface polarization in the coordinate frame dictated by the particle shape and then arrive at an expression for the electric field. Eq. 7.20 is calculated from the effective susceptibility, which already has the macroscopic experimental symmetry incorporated in it. This makes the actual calculation shorter and more general as the specific properties of the particle become important only in the last stage of the evaluation.

To obtain a clear analogy between the scattering experiment and a surface sum frequency experiment, we introduce angles $\theta_{0,1,2}$ as in Fig. 7.2 and rewrite Eq. (7.20) as:

$$E_{ppp}(r) \propto 2(\Gamma^{(2)}_{\perp\perp\perp} \sin\theta_0 \sin\theta_2 \sin\theta_1 + \Gamma^{(2)}_{\perp\|\|} \sin\theta_0 \cos\theta_2 \cos\theta_1 - \Gamma^{(2)}_{\|\|\perp} \cos\theta_0 \cos\theta_2 \sin\theta_1 - \Gamma^{(2)}_{\|\perp\|} \cos\theta_0 \sin\theta_2 \cos\theta_1). \tag{7.24}$$

Apart from a geometrical factor, this expression corresponds exactly to that found for a conventional surface sum frequency experiment [99] (where the Fresnel fac-

tors are neglected, which is essentially the Rayleigh-Gans-Debye approximation). The difference lies in the nature of the detection. In a surface sum frequency experiment one detects the whole SFG signal in the far field and has to take into account the illuminated area of the surface (resulting in an amplitude factor that scales with $\frac{1}{\cos\theta_0}$). In the scattering experiment only a small portion of the scattered field is collected.

For a given particle shape $\Gamma^{(2)}$ can be expressed in terms of the local susceptibility elements, the scattering angle and particle dimension (both contained in $\mathbf{q}$). For an isotropic medium we only need to consider the surface contributions. For a spherical particle we can write:

$$\Gamma_{ijk}^{(2)}(\mathbf{q}) = \sum_{\alpha,\beta,\gamma} \chi_{\alpha\beta\gamma}^{(2)} \oint (\mathbf{e}_\alpha \cdot \mathbf{u}_i)(\mathbf{e}_\beta \cdot \mathbf{u}_j)(\mathbf{e}_\gamma \cdot \mathbf{u}_k) e^{i\mathbf{q}\cdot\mathbf{r}} d^2\mathbf{r}, \qquad (7.25)$$

where the integral is over the particle surface, $\chi_{\alpha\beta\gamma}^{(2)}$ are the elements of the local surface susceptibility and $\mathbf{e}_{\alpha,\beta,\gamma}$ represent the unit vectors of the spherical coordinate system of the particle. The resulting expressions for the elements of $\Gamma^{(2)}$ are given in section 6.1 in Table 6.1 for an isotropic spherical particle (for which $\chi^{(2)}$ has only four independent elements [16]).

7.3.3   Small index difference

One of the successful models that has been used in the past to describe linear scattering, is the so-called Wentzel-Kramers-Brillouin (WKB) approximation [100]. It can be applied to particles, which have relatively small refractive index contrast ($\delta n = n_p - n_m$) with the surrounding medium, i.e. $|\delta n| \ll 1$. In the RGD approximation the electromagnetic wave is assumed to travel through the particle, without being modified in any way by its presence. It has been demonstrated that in linear scattering the most important refinement lies in the phase-shift that an electromagnetic wave experiences as it travels through the particle [100]. To embed this correction within the RGD approximation, one can assume that the waves retain their parallel character, without changing direction or amplitude. Hence the phase on the directly illuminated half of the particle (the white area in Fig. 7.3) is exactly that of the incoming wave, whereas the phase of the outgoing wave (the grey area in Fig. 7.3) must be corrected by an amount $\delta n_i l_i k_i$, where δn_i is the refractive index contrast at the frequency of the i-th wave, having wave vector $\mathbf{k_i}$ and l_i is the distance travelled by the wave inside the particle. This is illustrated in Fig. 7.3, which shows one wave $\mathbf{k_i}$ interacting with the particle. If we apply this to scattering by a spherical particle, the local field at the *outer side* of the surface can be written as:

$$\mathcal{L}_{\alpha_i}^{\mathbf{k_i}}(\mathbf{r}) = \mathbf{u}_{\alpha_i}^{\mathbf{k_i}} \exp(i\delta n_i [\mathbf{k_i} \cdot \mathbf{r} + |\mathbf{k_i} \cdot \mathbf{r}|]). \qquad (7.26)$$

Effectively this restates that the wave becomes phase shifted as it exits the sphere. Namely, for $\mathbf{k_i} \cdot \mathbf{r} < 0$ (on the illuminated part of the particle) the two terms in
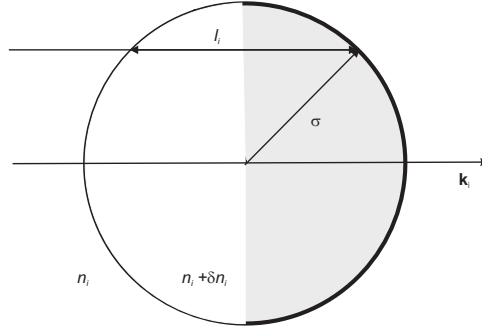
Figure 7.3: Illustration of the Wentzel-Kramers-Brillouin approximation. At the surface of the backside (dark area) the wave is phase shifted by an amount $\delta n_i l_i k_i$.

the exponent cancel each other and $\mathcal{L}^{\mathbf{k}_i}_{\alpha_i} \to \mathbf{u}^{\mathbf{k}_i}_{\alpha_i}$.

With the aid of Eq. (7.18) the effective surface susceptibility of a sphere in the WKB approximation becomes:

$$
\begin{aligned}
\Gamma^{(2)}_{\alpha_0,\alpha_1,\alpha_2} &= \oint \left[\mathbf{u}^{\mathbf{k}_0}_{\alpha_0} \cdot \boldsymbol{\chi}^{(2)}(\mathbf{r}) \cdot \mathbf{u}^{\mathbf{k}_1}_{\alpha_1} \cdot \mathbf{u}^{\mathbf{k}_2}_{\alpha_2} \right] \\
&\times \quad \exp(-i\mathbf{q} \cdot \mathbf{r}) \, \exp\left[i\,\delta n_0(-\mathbf{k}_0 \cdot \mathbf{r} + |\mathbf{k}_0 \cdot \mathbf{r}|) \right. \\
&+ \quad \left. i\,\delta n_1(\mathbf{k}_1 \cdot \mathbf{r} + |\mathbf{k}_1 \cdot \mathbf{r}|) + i\,\delta n_2(\mathbf{k}_2 \cdot \mathbf{r} + |\mathbf{k}_2 \cdot \mathbf{r}|) \right] \mathrm{d}^2\mathbf{r}.
\end{aligned}
\tag{7.27}
$$

For a centrosymmetric sphere one can also use the symmetry of $\boldsymbol{\chi}^{(2)}$ upon inversion of the spatial coordinates, namely

$$
\boldsymbol{\chi}^{(2)}(-\mathbf{r}) = -\boldsymbol{\chi}^{(2)}(\mathbf{r}).
$$

The integral in Eq. (7.27) runs over the whole spherical surface and, thus, $\mathbf{r}$ can be replaced by $-\mathbf{r}$. We can rewrite the integral as a half of the sum of these two forms (i.e., with $\mathbf{r}$ and $-\mathbf{r}$). This gives:

$$
\begin{aligned}
\Gamma^{(2)}_{\alpha_0,\alpha_1,\alpha_2} &= i \oint \mathbf{u}^{\mathbf{k}_0}_{\alpha_0} \cdot \boldsymbol{\chi}^{(2)}(\mathbf{r}) \cdot \mathbf{u}^{\mathbf{k}_1}_{\alpha_1} \cdot \mathbf{u}^{\mathbf{k}_2}_{\alpha_2} \\
&\times \quad \exp(i\,\delta n_0 |\mathbf{k}_0 \cdot \mathbf{r}| + i\,\delta n_1 |\mathbf{k}_1 \cdot \mathbf{r}| + i\,\delta n_2 |\mathbf{k}_2 \cdot \mathbf{r}|) \\
&\times \quad \sin(\mathbf{q} \cdot \mathbf{r} - \delta n_0 \mathbf{k}_0 \cdot \mathbf{r} + \delta n_1 \mathbf{k}_1 \cdot \mathbf{r} + \delta n_2 \mathbf{k}_2 \cdot \mathbf{r}) \, \mathrm{d}^2\mathbf{r}.
\end{aligned}
\tag{7.28}
$$

If we compare these expressions to the ones obtained using the RGD approximation it is clear that if the refractive index contrast δn_i becomes appreciable and frequency dependent $\delta n_0 \neq \delta n_1 \neq \delta n_2$, the scattered intensity in the phase matched direction ($\mathbf{q} = 0$) is not necessarily 0.

7.3.4 Correlated scattering

So far, we have considered scattering from only one particle. Here, we will describe correlated scattering but restrict ourselves to weak scattering so that one can neglect the effect of the scatterers on the wave propagation (i.e., one can ignore multiple scattering). For a system of many scatterers one has to take into account the fact that the phases of the scattered waves can become correlated. In the following we assume that the sample consists of N identical particles, which are spherically symmetric, i.e. their scattering field does not depend on their orientation.

We then have to sum up all the scattered waves $\mathbf{E}_j$. Given the assumptions mentioned above, these fields have the same amplitude but may possess a different phase that arises from a position-dependent delay of the fundamental fields and the varying path length of the scattered fields (the distance between the scatterer and the detector, $|\mathbf{r}_0|$). In the Fraunhofer zone (i.e. $|\mathbf{r}_j - \mathbf{r}_k| \ll \sqrt{\lambda |\mathbf{r}_0|}$) we can write for the scattered intensity:

$$I(\mathbf{q}) = \sum_{k=1}^{N} \sum_{j=1}^{N} |\mathbf{E}|^2 e^{i\mathbf{q}(\mathbf{r}_j - \mathbf{r}_k)} = N|E|^2 \langle \sum_{j=1}^{N} e^{i\mathbf{q}(\mathbf{r}_j - \mathbf{r}_k)} \rangle_k \qquad (7.29)$$

where the brackets denote an ensemble average. This bracketed term is known as the structure factor $S(\mathbf{q})$ in x-ray diffraction [101, 102]. If the concentration of scattering particles is low there is no positional correlation between the emitted fields of the individual particles and the only non-zero contribution to the sum in Eq. (7.29) arises from terms with $j = k$. This means that we are dealing with independent scatterers and that the scattered intensity can be described by uncorrelated scattering, i.e. $S(\mathbf{q}) = 1$. Consequently, the total scattered intensity can be described by an incoherent sum of the scattered intensity of the individual particles. For a dense suspension, the particle positions become correlated, leading to correlations of the phases of the scattered fields, so that $S(\mathbf{q}) \neq 1$. In a disordered (fluid) suspension the structure factor $S(\mathbf{q})$ will reflect the short-range order between the neighbors, while if the particles form a regular periodic structure (as in colloidal crystals, for example), the long-range correlation between the particle positions leads to development of the Bragg peaks in $S(\mathbf{q})$ at specific values of the scattering vector $\mathbf{q}$.

Thus, the effect of particle correlations on nonlinear scattering is very similar to that in linear optics. However, an interesting aspect appears in the forward scattering, for $\mathbf{q} = 0$. In linear scattering and diffraction extraction of useful information in the forward direction ($\mathbf{q} = 0$) is complicated due to the presence of the strong primary beam. In contrast, this is not necessarily the case for nonlinear scattering as one can directly measure the scattered field in the forward direction. At $\mathbf{q} = 0$ the waves scattered by different particles have the same phase, which should lead to a development of a Bragg-like forward peak even in disordered structures without long-range order. For periodic (crystalline) arrangements of

scattering particles comparison of the 'true' Bragg peaks (at $\mathbf{q} \neq 0$) and the forward peak (at $\mathbf{q} = 0$) could open novel approaches to access information on e.g. long-range ordering from a nonlinear diffraction experiment.

As discussed above, the forward scattering intensity of a single particle could be very weak, which could complicate the observation of the forward nonlinear scattering peak. In the case of second harmonic generation ($\omega_1 = \omega_2$) the intensity scattered exactly into the forward direction should vanish due to symmetry reasons. A forward SHG peak observed in Ref. [91] in transmission through a system of silicon nano-clusters in a silica matrix was associated with spatial inhomogeneities in the medium on length scales exceeding the wavelength or a gradient of the light intensity in a tightly focused laser beam [92]. Both explanations imply that the forward SHG peak must be broader than the angular width of the excitation beam, in agreement with experiment [91]. In the case of sum frequency generation ($\omega_1 \neq \omega_2$) with a non-colinear excitation geometry, however, the symmetry does not forbid forward scattering from a single particle even if the latter possesses spherical symmetry. As shown in the preceding section and further illustrated in section 7.3.5, the forward scattering intensity remains finite for a finite refractive index mismatch.

As a final remark, we note that for given directions of the fundamental beams, $\mathbf{q}$ can be finite for any detection direction since its length (given by $|\mathbf{q}| = |-\mathbf{k}_0 + \mathbf{k}_1 + \mathbf{k}_2|$) is determined by both the incidence angle and the refractive indices for each different wavelength. In this case the resulting intensity should depend on the sample thickness d in the direction at which $\mathbf{q}$ reaches its minimum value $\mathbf{q}_{min}$. For $dq_{min} \ll 1$ the whole sample volume will coherently contribute to the forward peak. Otherwise, for $dq_{min} > 1$, the intensity of the forward scattering will display beatings as a function of the sample thickness d.

7.3.5 Comparison of RGD and WKB approximations

As the particle size increases the angle dependent intensity changes and it can be expected that at a certain radius the RGD approximation is no longer valid. Fig. 7.4 shows a comparison between the RGD and WKB approximations. Angular dis-
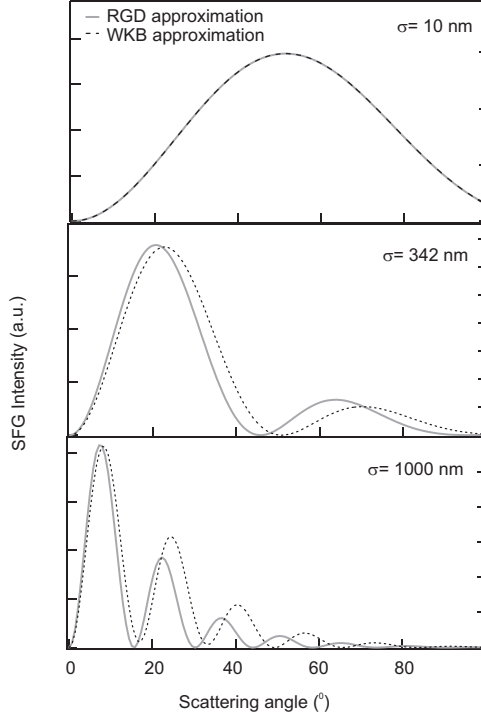
Figure 7.4: Comparison of the Wentzel-Kramers-Brillouin approximation to the Rayleigh Gans Debye approximation for spherical particles, with a radius of 10 nm, 342 nm and 1000 nm. It shows that for larger particles the phase shift becomes significant and the scattering patterns start to differ significantly.

tributions are calculated for different radii. The input parameters are: $\chi^{(2)}_{\perp\perp\perp}=1$, $\chi^{(2)}_{\perp\|\|}=0$, $\chi^{(2)}_{\|\perp\|}=0$, $\chi^{(2)}_{\|\|\perp}=0$ and $\lambda_1=3448$ nm, $n_1=1.49$, $\lambda_2=793$ nm, $n_2=1.46$, $\lambda_0=645$ nm, $n_0=1.46$ and a realistic refractive index contrast of $\delta n=-0.1$ (defined as the difference between the solute and the particle). For these values both approximations produce the same radiation pattern for the small (10 nm) particles. For larger sizes, the phase shift becomes significant and the scattering patterns start to differ. For relatively large particles ($\sim$1 μm) the difference becomes ap-

preciable, especially at larger angles. This effect was also observed when the RGD and WKB approximation were compared in linear scattering experiments [100]. This shows that for samples like the stearyl-coated silica particles in CCl$_4$ the Rayleigh-Gans-Debye approximation is valid and that typically for micron sized particles one needs to take into account the phase shift that the waves experience as they travel through the particle.
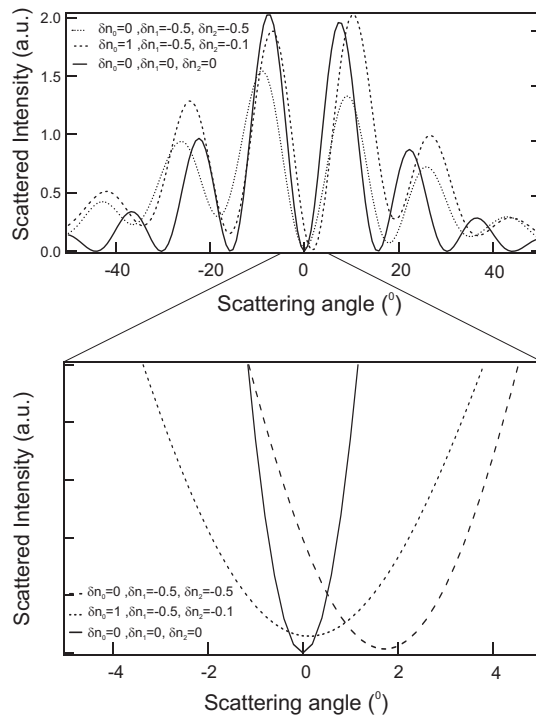
Figure 7.5: Scattered intensity for a single sphere with a radius of 1000 nm in the Wentzel-Kramers-Brillouin approximation, with different values of $\delta n_{0,1,2}$, demonstrating that in contrast to the Rayleigh-Gans-Debye approximation ($\delta n_{0,1,2} = 0$) there can be scattered intensity in the phase matched direction if the index contrast increases.

Fig. 7.5 shows several calculations for the scattered SFG intensity as a function of the scattering angle for several refractive index contrasts. It shows that, in contrast to the Rayleigh-Gans-Debye approximation there can be scattered intensity in the phase matched direction if the index contrast increases. If we also take into account the notion that at this scattering angle the scattered intensity becomes

proportional to the square of the number of particles in the suspension, we might expect a peak in the phase matched direction. In our experiments with colloidal particles dispersed in CCl_4 however, we were not able to observe a peak in this direction. This could be due to the small contrast in our sample ($|\delta n| < 0.1$ for all wavelengths) in combination with the relatively small radii. For a dried (drop-casted) sample of colloids we did observe a small signal in the forward direction. Due to limitation imposed by our experimental geometry we were not able to collect an angle dependent intensity plot with significant resolution. The observation of a signal in the forward direction does however corroborate our predictions.

7.4   Conclusions

In conclusion, we have introduced the concept of an effective susceptibility to formulate a generalized treatment of nonlinear optical scattering. From simple symmetry arguments we can deduce selection rules that are independent of the properties of the scattering object. For sum frequency scattering in particular, we have considered limiting cases of small particle scattering, index matched (Rayleigh-Gans-Debye) scattering, small index contrast (Wentzel-Kramers-Brillouin) scattering and correlated scattering. We have found that for particles with radii up to several hundred nanometers the RGD approximation generates a good description, in good agreement with the first findings presented in Chapter 6. Phase differences upon traversing the particle need to be incorporated for larger particles (for comparable refractive index contrast).

Chapter 8

Molecular origin of a phase transition of colloids

We have studied the phase behavior of a colloidal dispersion at the molecular level using sum frequency generation (SFG) scattering. By expanding the scattering theory developed in Chapter 6 we can selectively monitor the order and orientation of the molecular stearyl ($C_{18}H_{37}$) groups that terminate the surfaces of the sub-micron sized silica colloids dispersed in hexadecane. In the highly viscous gel state, at low temperatures, the alkyl chains are very well ordered and oriented. In contrast, in the low viscosity suspension at higher temperatures, the surface molecules are disordered. By simultaneously monitoring the SFG spectrum and the phase behavior of the colloidal dispersion (through turbidity and calorimetric measurements) with varying temperature we obtain direct evidence that the surface-solvent interactions play a key role in the phase transition. We also investigate the molecular nature of gel aging and observe that (slow) ordering occurs over time periods ranging from minutes to days.

8.1   Introduction

Recently, colloidal particles have acquired a renewed interest as a tool to monitor molecular interactions in lipid membrane surfaces [103]. By modifying the surface layer of glass beads such that they contain phospholipids and proteins, information on the molecular level can be obtained by investigating the phase behavior of these particles. It has repeatedly been suggested that the surface plays an important role in physical interactions between particles governed by e.g. Van der Waals forces, electrostatic forces and sterical stabilization. For this reason colloids are often used as a model system [104, 105, 106, 107]. The surface to bulk ratio of colloidal particles is very large compared to non-colloidal matter, resulting in phase behavior that is expected to be dominated by the surface [104]. So far, the phase behavior has only been studied experimentally by thermodynamic measurements [108], linear scattering experiments with neutrons [109], x-rays and visible photons [110, 111, 112, 113] and microscopic imaging [103]. Although the (inherent or specifically engineered) molecular surface properties of the colloids affect their collective phase behavior, information on the surface properties has been obtained indirectly, as most techniques employed up to date lack molecular surface sensitivity.

As a well documented example of a phase transition of colloids, silica particles coated with alkyl chains are known to undergo a (reversible) phase transition when suspended in various apolar solvents like benzene, toluene, and n-alkanes [114, 115, 108] (see Fig. 8.1 (right panel)). The particle potential depends critically on the solvent-particle interaction [111] and can be changed by altering the temperature. Upon cooling below a certain temperature (known as the cloud-point) the particle-particle interaction changes from repulsive to attractive and the suspension enters a gel state or phase separates into a liquid-like and gas-like state [114].

With the recent development of surface specific second-order scattering techniques [78, 77, 75] and in particular vibrational sum frequency scattering (see Chapters 6 and 7) it has now become possible to obtain detailed information about the role of the surface in such a phase transition for the first time [116, 117].

In this Chapter we study a colloidal phase transition on a molecular level using sum frequency scattering. We draw upon the recently developed second-order scattering theory, in order to obtain information on the molecular orientation in a gel and a suspension and during gel aging of silica particles in n-hexadecane. By combining temperature dependent sum frequency scattering measurements, turbidity and calorimetric measurements we find direct evidence that the surface indeed plays an important role in the phase transition. We further investigate the role of the solvent on a molecular level by comparing a phase transition of silica particles in n-hexadecane with a phase transition of the same particles in benzene.

8.2   Experimental

The SFG experiments were performed using 7 μJ (120 fs) infrared (IR) pulses (repetition rate 1 kHz, FWHM bandwidth of ~180 cm^{-1}) centered around 2900 cm^{-1} and 3 μJ, 800 nm visible (VIS) pulses with a 7 cm^{-1} bandwidth. A schematic representation of the experimental geometry can be found in Fig. 8.1 (left panel). The selectively polarized IR and VIS pulses were incident under a relative angle of 15° (β) and focused down to a ~0.4 mm beam waist. The scattered light was collimated with a lens (with an angular acceptance of 17°), polarization selected and dispersed onto an intensified charge coupled device (CCD) camera [23, 24].
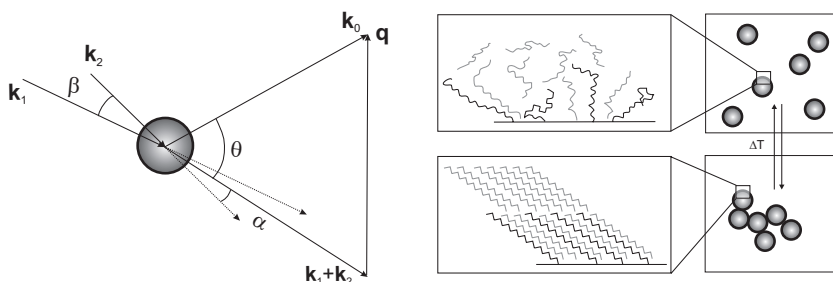

Figure 8.1: Left panel: The scattering geometry. $\mathbf{k}_0$, $\mathbf{k}_1$, $\mathbf{k}_2$ are the wave vectors of the scattered sum frequency, the visible and infrared fields. $\mathbf{q}$ is the scattering wave vector. All $\mathbf{k}$ vectors and the detector lie in one plane. The IR, VIS and SFG fields are either polarized parallel (p) or perpendicular (s) to the scattering plane. Right panel: Schematic illustration of the phase transition showing the transformation from gel into suspension, displaying the structural changes on a molecular scale that are found in this study (middle panel) and a microscopic scale (right panel).

The samples consist of dry stearic alcohol (C$_{18}$H$_{37}$OH) coated [81] silica particles [82] with a radius (σ) of 123 nm dispersed in n-hexadecane-d$_{34}$ (98 atom % D, Aldrich), n-hexadecane (> 99 %, Sigma Aldrich), and benzene-d$_6$ (99 atom % D, Sigma Aldrich) with a colloid volume fraction of 20 %. Gels were prepared by dispersing the particles in warm (~50 °C) solvent. The resulting suspension was quenched to room temperature. The sample cell consisted of a cuvette (Hellma GmbH) with a volume of 280 μl and a path length of 1 mm. The scattering angle θ (as measured in air) was 51^0. For temperature dependent scattering and turbidity[1] measurements, the sample temperature was raised by resistively heating the sample holder, resulting in a constant heating rate of typically 2.9 °C/min. The temperature was measured with a small thermocouple placed in the cell ~ 1 mm away from the laser focus. Unless otherwise stated, gel spectra were recorded at room temperature (20 °C) and the suspensions spectra were measured at 50

---

[1]The turbidity is defined as the extinction due to scattering and measured in the forward direction.

°C. The calorimetric measurements were performed in a differential scanning calorimeter with a heating rate of 0.5 °C/min and are described in detail else-where [118].

8.3 Molecular surface structure

8.3.1 Theoretical considerations

On a flat surface the orientation of the alkyl chains can be deduced by compar-ing the amplitude of the local surface susceptibility $\chi^{(2)}_{ijk}$ (where i,j,k represent the polarization directions, s or p) of the symmetric CH_3 stretching mode for the different polarization combinations, as described in detail in Refs. [21, 70]. For the analysis of these scattering sum frequency spectra we can adopt an analogous procedure by comparing the elements of $\chi^{(2)}$ for different polarization combina-tions that are accessible through the effective particle susceptibility.

In particular, for the isotropic surface of index matched particles, the ampli-tudes of the scattered transverse electric field for the different polarization com-binations are given by the following equations (see chapter 7):

$$E_{ppp} \propto \cos\frac{\theta}{2}[(\Gamma^{(2)}_{\perp\perp\perp} + \Gamma^{(2)}_{\perp\|\|})\cos\beta + (\Gamma^{(2)}_{\perp\perp\perp} - \Gamma^{(2)}_{\perp\|\|})\cos(\theta - \beta + 2\alpha)] \tag{8.1}$$

$$- \sin\frac{\theta}{2}[(\Gamma^{(2)}_{\|\|\perp} - \Gamma^{(2)}_{\|\perp\|})\sin\beta + (\Gamma^{(2)}_{\|\perp\|} + \Gamma^{(2)}_{\|\|\perp})\sin(\theta - \beta + 2\alpha)]$$

$$E_{ssp} \propto \Gamma^{(2)}_{\|\|\perp}(\cos\beta\cos(\frac{\theta}{2} + \alpha) + \sin\beta\sin(\frac{\theta}{2} + \alpha)) \tag{8.2}$$

$$E_{sps} \propto \Gamma^{(2)}_{\|\perp\|}\cos(\frac{\theta}{2} + \alpha) \tag{8.3}$$

$$E_{pss} \propto \Gamma^{(2)}_{\perp\|\|}\cos(\frac{\theta}{2}), \tag{8.4}$$

where θ is the scattering angle (in the solution), α is the angle between $\mathbf{k}_1$ and $\mathbf{k}_1 + \mathbf{k}_2$, β is the angle between $\mathbf{k}_1$ and $\mathbf{k}_2$ and p (s) refers to polarization parallel (perpendicular) to the plane of incidence. A full description is given in Chapter 7.

If we assume that the orientational distribution is cylindrically symmetric and note that away from electronic resonance the Raman tensor is symmetrical, there are only three independent elements of $\chi^{(2)}$ ($\chi^{(2)}_{yzy} = \chi^{(2)}_{xzx} = \chi^{(2)}_{zyy} = \chi^{(2)}_{zxx} = \chi^{(2)}_{\perp\|\|}$, $\chi^{(2)}_{yyz} = \chi^{(2)}_{xxz} = \chi^{(2)}_{\|\|\perp}$, and $\chi^{(2)}_{zzz} = \chi^{(2)}_{\perp\perp\perp}$). As a consequence there are also only three independent components of $\Gamma^{(2)}$ ($\Gamma^{(2)}_{\perp\perp\perp}$, $\Gamma^{(2)}_{\perp\|\|}$, $\Gamma^{(2)}_{\|\|\perp}$) and the spectra obtained by monitoring the polarization combinations sps and pss differ only by a factor $(\frac{\cos((\theta/2)+\alpha)}{\cos(\theta/2)})^2$. With the above assumptions the effective particle susceptibility

elements can be written in terms of the local surface susceptibility elements as:

$$\Gamma^{(2)}_{\perp\perp\perp} = 2\pi(B\chi^{(2)}_{\perp\perp\perp} + 2A\chi^{(2)}_{\perp\|\|} + A\chi^{(2)}_{\|\|\perp})$$
$$\Gamma^{(2)}_{\perp\|\|} = \pi(A\chi^{(2)}_{\perp\perp\perp} + 2B\chi^{(2)}_{\perp\|\|} - A\chi^{(2)}_{\|\|\perp}) \tag{8.5}$$
$$\Gamma^{(2)}_{\|\|\perp} = \pi(A\chi^{(2)}_{\perp\perp\perp} - 2A\chi^{(2)}_{\perp\|\|} + (A+2B)\chi^{(2)}_{\|\|\perp}),$$

where A and B are the familiar scattering form factors ($A = \frac{6i}{q^4\sigma^2}\{2(1-\frac{q^2\sigma^2}{3})\sin(q\sigma) - 2q\sigma\cos(q\sigma)\}$ and $B = \frac{6i}{q^4\sigma^2}\{(q^2\sigma^2 - 2)\sin(q\sigma) - q\sigma(\frac{q^2\sigma^3}{3} - 2)\cos(q\sigma)\}$).
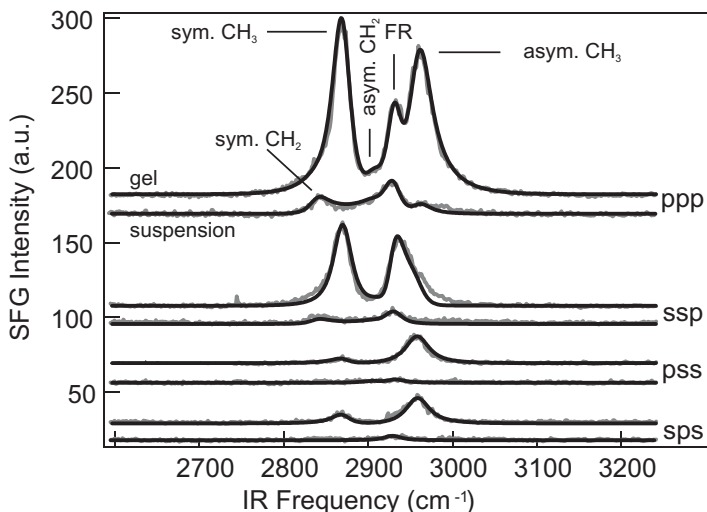
Figure 8.2: Four sets of SFG spectra (grey lines) obtained at different polarization combinations of a gel and a suspension of colloidal particles in n-hexadecane-d_{34}. The pairs represent from top to bottom the polarization combinations ppp, ssp, pss and sps. For each set the upper (lower) trace corresponds to the gel phase (suspension) measured at 20 °C (50 °C). The spectra were collected at a scattering angle of 51° and are offset for clarity. The black lines are fits as described in the text. The vibrational modes that appear in the SFG spectra are marked in the upper trace pair.

Fig. 8.2 shows SFG spectra of the dispersion in a gel state and in suspension. The four pairs correspond to spectra taken with polarization combinations ppp, ssp, pss and psp and the upper (lower) spectrum of each pair has been obtained with the sample in a gel state (suspension). As shown in Chapter 6 (and repeated here for the readers convenience) the scattered sum frequency field can be described very well with the well-known expression for SFG, where the local surface susceptibility ($\chi^{(2)}$) has been replaced by an effective particle susceptibility

($\Gamma^{(2)}$):

$$\mathbf{E}_0 \propto \sum_n \Gamma_n^{(2)} : \mathbf{E}_1 \mathbf{E}_2 \qquad \Gamma_n^{(2)}(\omega) = \frac{A_n}{(\omega - \omega_{0n}) + i\Upsilon_n}, \qquad (8.6)$$

where n refers to a vibrational mode, ω_{0n} is the resonance frequency and Υ_n the spectral half width at half maximum. The solid lines in Fig. 8.2 are fits to the data using the convolution of $\Gamma_n^{(2)}$ with the electric field envelope of the upconversion pulse:

$$I_0(\omega) \propto |\sum_n \int_{-\infty}^{\infty} \Gamma_n^{(2)}(\omega') E_1(\omega' - \omega) d\omega'|^2. \qquad (8.7)$$

The fits were achieved with the usual resonance frequencies for the symmetric CH_2 and CH_3 stretching modes (at 2854 cm^{-1} and 2888 cm^{-1} respectively), the asymmetrical CH_3 stretch vibration (2978 cm^{-1}), the Fermi resonances of the symmetric CH_3 stretching mode with an overtone of the CH_3 bending mode (2952 cm^{-1}) and a Fermi resonance of the symmetric CH_2 stretching mode with in plane methyl (CH_2) deformations (2925 cm^{-1}) [21, 70]. In the fit procedure the intensity variation due to polarization dependent infrared and visible intensities and detector efficiency was taken into account.

From Fig. 8.2 we can see that the gel spectra are dominated by the symmetric and asymmetric methyl (CH_3) stretching modes and that methyl (CH_2) stretch modes are almost absent. This indicates that there are very few chain defects in the surface layer and that the methyl groups are highly oriented with respect to the surface. Indeed, we can reproduce the polarization dependent intensity assuming a Dirac delta distribution for the tilt angle of the carbon backbone of the stearyl chains. We find that in the gel phase the carbon backbone of the chains are tilted with an angle of 54º away from the local surface normal. The corresponding fit value for the hyperpolarizability ratio (r) was 3.4, in good agreement with Ref. [11]. This analysis indicates that in the gel state the particle surfaces consist of highly ordered alkyl chains tilted away from the surface normal, composing a highly ordered layer of surface molecules at room temperature (21 ºC). In contrast, the spectra taken of the suspension are dominated by the methyl (CH_2) stretch modes and Fermi resonance, whereas the methyl (CH_3) stretch modes are absent. This indicates that upon heating of the gel the alkyl chains at the surface lose their ordering and the crystalline-like layer transforms into a disordered one. It also implies that the surface coverage of the particles with alkyl chains is not very dense, because there is enough space for the molecules to form a disordered layer.

It must be noted that the above fitting procedure is valid only if the refractive index of the particles and solvent are nearly identical and the particles are small. This analysis also works for the spectra of the gel state despite the fact that the analysis becomes more complicated because both structure and form factor may change, leading to changes in the intensity (that are independent of frequency). However, it has been shown that for small particles with a low contrast

the structure factor can still be approximated by the above expressions [112]. Furthermore, it was shown that the structure factor changes only by a factor of 2 upon gel formation (leading to a larger intensity of the gel signal) [113]. The change observed in Fig. 8.2 is much larger than this, which indicates that the amplitude change can be traced back to changes in the surface structure. This is also evident from the very different spectral shape of the response of the gel and the suspension state.

To see whether the order is confined to the first layer we have also taken SFG spectra of a 20 v% gel in a mixture of 80 v% n-hexadecane-d_{34} with 20 v% n-hexadecane. Replacing part of the deuterated solvent by non-deuterated solvent does not affect the phase behavior of the dispersion (see section 8.4.2 and [119]).

The SFG spectrum of an ordered layer is dominated by the vibrations of the methyl (CH_3) groups (as is evident from Figs. 8.2 and 5.2). Also, as part of the solvent is non-deuterated some of the signal might be lost due to destructive interference with methyl (CH_3) groups that are pointing in the opposite direction. The amount of intensity loss critically depends on the structure of the layer. If local inversion symmetry exists over a long range around the particle, a large portion of the signal might be lost. A disordered layer on the other hand can be expected to be dominated by the methyl (CH_2) stretching modes and the Fermi resonances.
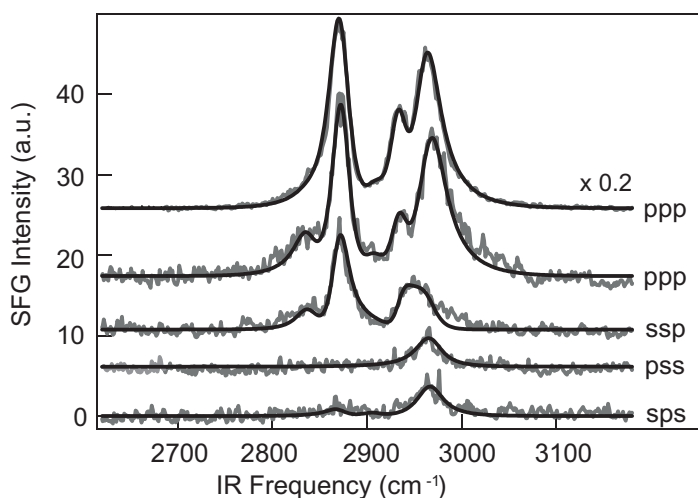
Figure 8.3: SFG spectra (grey lines) obtained at different polarization conditions of a gel of colloidal particles in 20/80 v% n-hexadecane/n-hexadecane-d_{34}. The spectra were taken at polarization combinations ppp, ssp, pss and sps and collected at a scattering angle of 51°. The black lines are fits as described in the text. The top trace shows the SFG spectra of a gel with fully deuterated hexadecane in ppp polarization combination (the same as in Fig. 8.2).

Fig. 8.3 shows SFG spectra taken at different polarization combinations of a 20 v% gel in a mixture of 80 v% n-hexadecane-d_{34} with 20 v% n-hexadecane. These spectra are fitted with the same parameters as used in the fits of Fig. 8.2. These gel spectra are dominated by the methyl (CH_3) stretching modes, but there is also a clear signal from the symmetric methyl (CH_2) stretching mode (at ∼ 2850 cm^{-1}). Also, it can be seen that the signal from the gel state in a solvent mixture is over a factor of 5 smaller than the signal from the gel in 100 % n-hexadecane-d_{34}. This dramatic decrease in intensity is much more than expected if we take the absorption of the infrared into account (which amounts to a intensity loss of 15 %).

Both the decrease in intensity as well as the appearance of CH_2 resonances are related to the structure of the solvent around the particles. The loss of intensity cannot be due to disorder as witnessed by the strong signal from the methyl (CH_3) groups (compared to that of the methylene (CH_2) groups), that still dominate the spectrum. The CH_2 resonances should be much stronger than what is observed to account for the decrease in the overall signal (see e.g. Fig. 5.3). As mentioned above, the alkyl chains are not densely packed on the surface and to form a crystalline layer the solvent molecules must participate to form an ordered layer. The dramatic intensity difference upon partially non-deuterating can be explained by the formation of one (or several) more or less ordered layers on top of the first, leading to restoration of local inversion symmetry. It explains why a relatively small amount of non-deuterated solvent leads to a disproportionate change in intensity. The ordered layers gradually transform into disordered solvent, which leads to the appearance of more pronounced methyl (CH_2) stretch modes that are representative of the number of chain defects. This kind of gradual loss in order has been observed also for multilayered self assembled monolayers of stearic acid [120]. The formation of ordered layers is illustrated in the middle panel of Fig. 8.1.

8.3.2   Gel aging

To investigate the mechanism through which the crystalline layer is formed we have taken SFG spectra as a function of time after preparation of the gel.
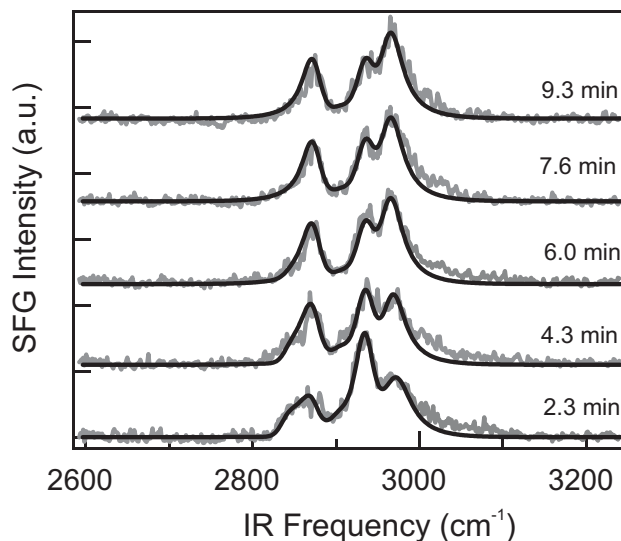

Figure 8.4: SFG spectra with ppp polarization combination of a 20 v% gel as a function of age. It shows spectra taken after several minutes after preparation. The acquisition time for each spectrum was 100 s. Fits were performed as described in the text.

Fig. 8.4 shows ppp polarized SFG spectra at several time intervals after preparation of the gel. It shows that the SFG spectra change dramatically over a time span of minutes. Directly after formation they are dominated by the Fermi resonance (at 2952 cm^{-1}) and the symmetric methyl (CH$_2$) stretch vibration (at 2856 cm^{-1}), whereas after a few minutes the symmetric (at 2890 cm^{-1}) and asymmetric methyl (CH$_3$) (at 2978 cm^{-1}) stretch modes appear. Fig. 8.5 shows spectra after a few hours up to a few days. The inset displays the amplitudes (obtained from the fits) of the symmetric methyl (CH$_3$) and methyl (CH$_2$) stretch modes that can be used to follow the order in the octadecyl layer. It shows that directly after formation the methyl (CH$_2$) stretch mode looses intensity, followed by a (slower) increase of the methyl (CH$_3$) stretch modes. This indicates that the order in the layer increases, starting at the surface of the sphere and working its way outwards. This kind of behavior has been observed previously also for self assembled monolayers (SAMs) of docosanethiol (CH$_3$(CH$_2$)$_{21}$SH) on polycrystalline gold [121]. After formation of the monolayer it was observed that in the first few minutes the chain defects disappear, followed by a slow in-growth

of the methyl (CH$_3$) stretch vibrations. This slow in-growth was assigned to slow reorientation in an almost fully packed layer. From the sequence of events it was concluded that ordering starts at the gold surface and works its way outward. As the time scales are comparable as well as the order of events it is very likely that the same mechanism occurs in the aging process of this gel.
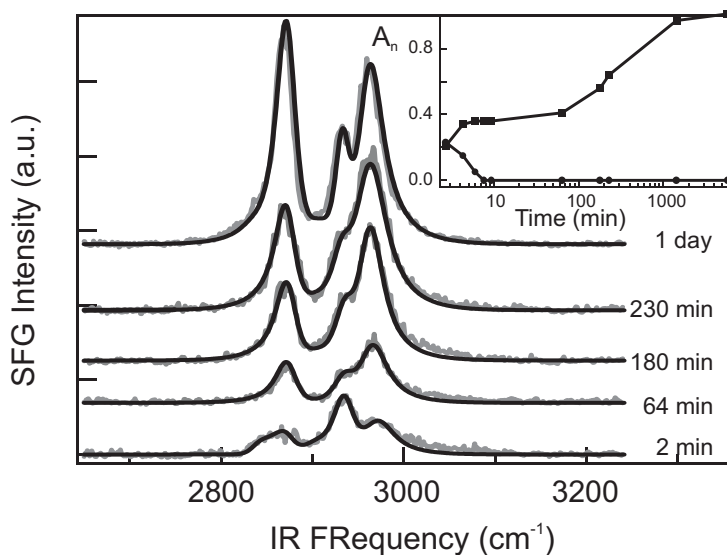
Figure 8.5: SFG spectra with ppp polarization of a 20 v% gel as a function of age. It shows spectra taken after an hour up to a few days. The inset shows the amplitude of the symmetric CH$_3$ (open circles) and CH$_2$ (closed circles) stretch modes. The acquisition time was 100 s. for each spectrum. Fits were performed as described in the text.

8.4 Temperature dependence and the role of the solvent

8.4.1 Calorimetric measurements

To obtain a more profound understanding of the role of the solvent we can compare the scattering results to calorimetric measurements performed on similar systems. Fig. 8.6 shows calorimetric measurements, reproduced from [118], of stearyl-coated silica particles with a radius of 36 nm in n-hexadecane. As can be seen in Fig. 8.6, starting with a frozen sample, upon heating three peaks are observed. The origin of the first peak is unclear and is independent of the solvent and unrelated to gel breakup. The second, large, peak is also present for pure n-hexadecane samples and corresponds to melting of n-hexadecane. The third peak

is observed between the melting point of n-hexadecane and the cloud-point[2] and is shown more clearly in the right panel of Fig. 8.6. It is not present at low concentration when there is no gel formation. Furthermore this additional heat effect is also absent for phase transitions in benzene or toluene [108, 118] and always occurs at lower temperatures than the cloud-point.
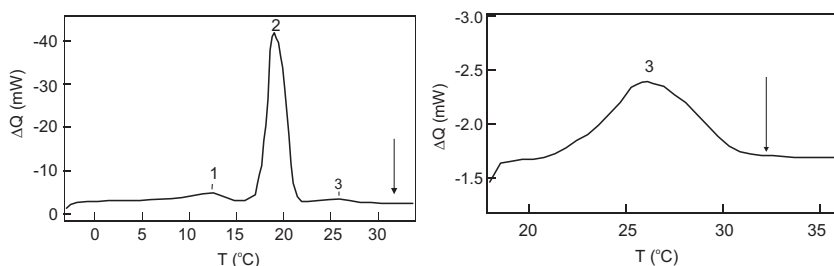

Figure 8.6: Calorimetric measurements of 28.9 v% 30 nm stearyl-coated silica particles in n-hexadecane, starting at -5 °C (left panel) and 18 °C (right panel). The heating rate in both cases was 0.5 °C/min. The arrow marks the cloud-point of the dispersion. The heat effects associated with the three peaks are 7.5 J/g for the first peak, 97.7 for the n-hexadecane melting peak and 4.8 J/g for the additional third peak that can be associated to gelation.

These measurements show that there is a clear difference between solvents, indicating that the solvent-particle interaction is of prime importance in the phase transition and that prior to gel breakup a very endothermic transition occurs. Given that the heat of fusion of n-hexadecane is 228.8 J/g [118], the 4.8 J/g observed amounts to melting of a surface layer (on particles with a radius of 36 nm) with a thickness of 1.1 nm.

From a series of calorimetric measurements (including the one presented in Fig. 8.6) it was proposed that upon cooling, the n-hexadecane solvent molecules mix with the stearyl chains and form a crystalline layer on the surface of the colloids. Such a transition can explain the observed heat effect as well as the solvent dependence and also causes the particle-particle interaction to become attractive, leading to gelation [118].

8.4.2   Phase transition in n-hexadecane

To investigate the mechanism through which the gel transforms into a suspension we have taken SFG spectra (Fig. 8.7) while the gel was heated with a constant heating rate and compared it to a turbidity measurement of the same sample with the same heating rate. The bottom panel of Fig. 8.7 shows the turbidity

---

[2]The cloud-point is usually defined as the temperature at which the turbidity starts to change due to appearance of clusters and aggregates and marks the onset of gelation upon cooling [122].

as a function of temperature for a 20 v% colloidal suspension in solution of n-hexadecane-d_{34} and a mixture of n-hexadecane-d_{34} and n-hexadecane (80 v%, 20 v%).
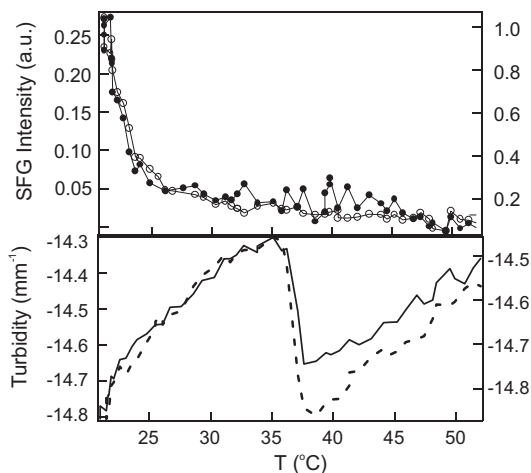
Figure 8.7: Integrated SFG intensity (upper panel) and turbidity (lower panel) as a function of temperature for silica particles dispersed in n-hexadecane-d_{34} (open circles, dashed line, right axis) and a mixture of n-hexadecane-d_{34}/n-hexadecane (80 v%/20 v%) (solid circles, solid line, left axis).

The integrated SFG intensity drops rapidly over an order of magnitude as the temperature is raised from room temperature to above the cloud-point[3] (at 37 °C). There is no difference between the purely deuterated solvent and the mixture, which indicates that gel formation and breakup occur in the same way and at the same temperature. As shown in Fig. 8.2 and discussed in section 8.3, the intensity drop is caused by the loss of order in the surface layer and the solvent.

8.4.3   Phase transition in benzene

To investigate the role of the solvent on a molecular level we have compared temperature dependent sum frequency scattering measurements of 20 v% dispersions in n-hexadecane-d_{34}, with those in benzene-d_6. Fig. 8.8 shows SFG spectra (left panel) of a suspension in n-hexadecane-d_{34} (upper trace) and in benzene-d_6 (lower trace). Both spectra are dominated by chain defects, indicating a disordered surface layer.

---

[3]In our system we did not observe a significant hysteresis.

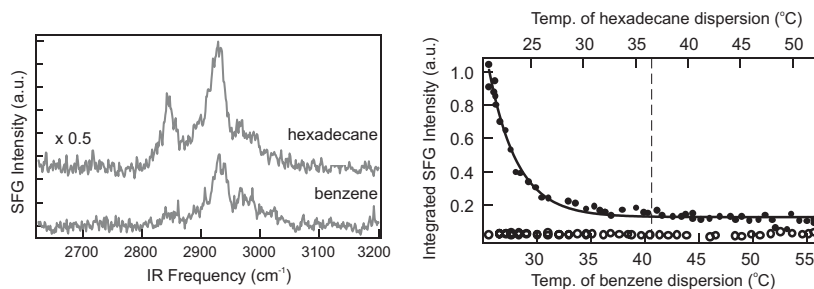**Figure 8.8:** SFG spectra (left panel) of a suspension in n-hexadecane-d_{34} (upper trace) and in benzene-d_6 (lower trace) at 50 $^{\circ}$C. The acquisition time was 200 s. Integrated SFG intensity (right panel) as a function of temperature for a 20 v% dispersion in n-hexadecane-d_{34} (upper temperature scale) and in benzene-d_6 (lower temperature scale). The solid line corresponds to an exponential fit and is a guide for the eye. The dashed line marks the cloud-point of both dispersions.

In contrast to the dramatic changes observed in hexadecane, Fig. 8.8 shows that there is no change in the SFG signal following the phase transition in benzene. This clearly demonstrates the importance of the solvent and shows that the observed molecular changes at the surface are induced by solvent-particle interactions.

8.4.4 Discussion of solvent effect

From the calorimetric measurements and the temperature dependent scattering experiments it has become clear that although the physical origin of the phase transition is identical (Van der Waals interaction between the particles) the underlying molecular mechanism is strongly influenced by the solvent and might appear very different on the molecular scale. As stated above, the difference is caused by solvent-surface interactions. For solvents that interdigitate with the surface alkyl chains the attractive interaction that appears at low temperature is caused by the formation of a crystalline layer on the surface. This changes the Van der Waals interaction such that there is a net attraction between the particles. The formation of this crystalline layer occurs a few degrees above the melting point of the solvent and can be correlated to the well-known phenomenon of surface freezing in (mixtures of closely related) n-alkanes [123, 124, 125, 126, 127]. In these systems it was observed that prior to freezing of the bulk the surface layer undergoes an order/disorder transition to form a crystalline interfacial layer.

For dispersions in solvents that do not interdigitate with the alkyl chains like benzene a crystalline layer cannot be formed. The particle-particle interaction can become attractive upon lowering the temperature only if the interaction between the alkyl chains becomes favorable compared to alkyl chain-solvent interaction. Then the alkyl chains form a disordered surface layer, with a high density. This

does not result in a changing SFG scattering signal nor does it lead to an additional significant heat effect.

8.5 Conclusions

Using sum frequency scattering we have investigated the phase transition of a colloidal suspension on the molecular level. We find that the surface of stearyl-coated silica particles in a gel state in n-hexadecane consists of an ordered, crystalline layer. This order is not confined to the first layer but gradually is lost in the solvent. Upon heating the ordered layer melts, causing the gel to break up. This melting can be associated to the phenomenon of surface freezing and is solvent dependent. It does not occur for solvents that cannot interdigitate between the surface chains. After formation of a gel it takes a few days for the first layer to become perfectly crystalline. The order starts at the surface and works it way outward.

Appendix A

Molecular orientation from SFG spectra

To find the molecular orientation from a macroscopic sum frequency generation experiment one needs to relate the macroscopically generated sum frequency field to molecular properties that depend on the symmetry of the molecules. If we describe a molecular layer on an interface as a three layer system (as depicted in Fig. A.1), we can write for the induced polarization at the interfacial region:

$$\mathbf{P}^{(2)}(\omega_0 = \omega_1 + \omega_2) = \boldsymbol{\chi}^{(2)}(\omega_0 = \omega_1 + \omega_2) : \mathbf{E}(\omega_1)\mathbf{E}(\omega_2), \qquad \text{(A.1)}$$

where $\mathbf{E}(\boldsymbol{\omega_1})$ ($\mathbf{E}(\boldsymbol{\omega_2})$) is the visible (infrared) field and $\boldsymbol{\chi}^{(2)}(\omega_0 = \omega_1 + \omega_2)$ is the second-order susceptibility.
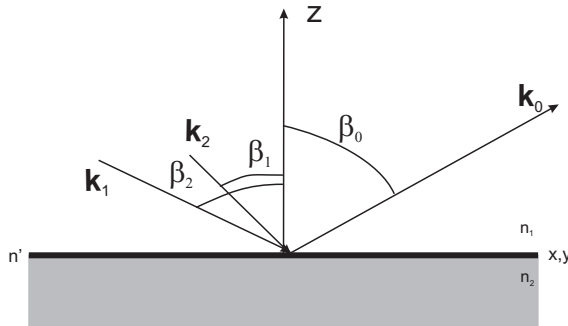

Figure A.1: Illustration of the geometry for an SFG experiment.

In the electric dipole approximation (i.e., the interaction is determined by the electric-dipole operator only) there is no contribution from the bulk media 1 and 2. The radiated electric field ($\mathbf{E_0}$) can be calculated from the Maxwell equations using the polarization (Eq. A.1) as a source term [5, 19]. From there the radiated intensity ($I = \frac{c}{2\pi}\sqrt{\epsilon}|\mathbf{E}_0|^2$) can be calculated:

$$I = \frac{8\pi^3\omega^2\sec^2\beta}{c^3 n_1(\omega_0)n_1(\omega_1)n_1(\omega_2)}|\chi_{eff}^{(2)}|^2 I_1(\omega_1)I_2(\omega_2),\qquad(A.2)$$

where $n_1(\omega_i)$ is the refractive index in medium 1 at frequency ω_i, c the speed of light in vacuum and $I_i(\omega_i)$ the intensity of the corresponding electric field. The radiated electric field is not only modified by second-order surface susceptibility, but also by the linear interactions of the electrical fields with the surrounding media. Both effects can be described using an effective surface susceptibility ($\chi_{eff}^{(2)}$). If the incoming waves have a polarization (unit)vector $\mathbf{u}_i$ and the linear modification is dictated by the Fresnel factors $\mathbf{L}(\omega_i)$, the effective surface susceptibility is given by [21]:

$$\chi_{eff}^{(2)} = (\mathbf{u}_0\cdot\mathbf{L}(\omega_0))\cdot\chi^{(2)}:(\mathbf{u}_1\cdot\mathbf{L}(\omega_1))(\mathbf{u}_2\cdot\mathbf{L}(\omega_2)).\qquad(A.3)$$

For an azimuthally isotropic interface the x and y directions are interchangeable and there are only four independent elements of the second-order nonlinear susceptibility: $\chi_{yzy}^{(2)} = \chi_{xzx}^{(2)}, \chi_{yyz}^{(2)} = \chi_{xxz}^{(2)}, \chi_{zyy}^{(2)} = \chi_{zxx}^{(2)}$ and $\chi_{zzz}^{(2)}$. These four components can be related to the experimentally accessible amplitude of the effective surface susceptibilities, measured for different polarization directions [21]:

$$
\begin{aligned}
\chi_{eff,ssp}^{(2)} =\,& L_{yy}(\omega_0)L_{yy}(\omega_1)L_{zz}(\omega_2)\sin\beta_2\chi_{yyz}^{(2)}\\
\chi_{eff,sps}^{(2)} =\,& L_{yy}(\omega_0)L_{zz}(\omega_1)L_{yy}(\omega_2)\sin\beta_1\chi_{yzy}^{(2)}\\
\chi_{eff,pss}^{(2)} =\,& L_{zz}(\omega_0)L_{yy}(\omega_1)L_{yy}(\omega_2)\sin\beta_0\chi_{zyy}^{(2)}\\
\chi_{eff,ppp}^{(2)} =\,& -L_{xx}(\omega_0)L_{xx}(\omega_1)L_{zz}(\omega_2)\cos\beta_0\cos\beta_1\sin\beta_2\chi_{xxz}^{(2)}\\
&-L_{xx}(\omega_0)L_{zz}(\omega_1)L_{xx}(\omega_2)\cos\beta_0\sin\beta_1\cos\beta_2\chi_{xzx}^{(2)}\\
&+L_{zz}(\omega_0)L_{xx}(\omega_1)L_{xx}(\omega_2)\sin\beta_0\cos\beta_1\cos\beta_2\chi_{zxx}^{(2)}\\
&+L_{zz}(\omega_0)L_{zz}(\omega_1)L_{zz}(\omega_2)\sin\beta_0\sin\beta_1\sin\beta_2\chi_{zzz}^{(2)}
\end{aligned}
\qquad(A.4)
$$

The macroscopic second-order surface susceptibility can be related to the molecular second-order hyperpolarizability $\alpha^{(2)}$, by a coordinate transformation from the molecular frame to the lab frame:

$$\chi_{ijk}^{(2)} = N_s\sum_{abc}\langle(\mathbf{i}\cdot\mathbf{a})(\mathbf{j}\cdot\mathbf{b})(\mathbf{k}\cdot\mathbf{c})\rangle\alpha_{abc}^{(2)},\qquad(A.5)$$

where N_s is the number of surface molecules, the brackets denote averaging over the molecular orientation, $\mathbf{i},\mathbf{j},\mathbf{k}$ are the lab frame unit vectors and $\mathbf{a},\mathbf{b},\mathbf{c}$ are molecular frame unit vectors.
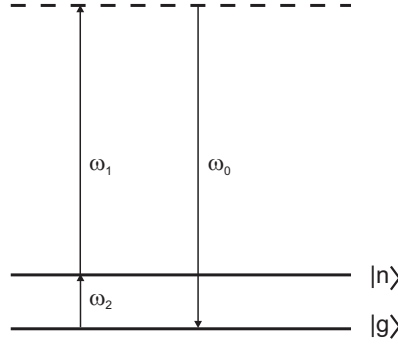
Figure A.2: Illustration of the molecular level scheme for vibrational sum frequency generation, showing the ground state $|g\rangle$, the excited vibrational state $|n\rangle$ and a virtual state.

$\alpha^{(2)}$ contains the information about the symmetry of the molecule under study and can be derived using the density operator formalism [15, 16]. For the simple case in which only one of the fields is resonant with a vibrational transition (illustrated in Fig. A.2) the hyperpolarizability becomes:

$$\alpha^{(2)}_{ijk}(\omega_0 = \omega_1 + \omega_2) =$$
$$\alpha^{(2)}_{NR} + \frac{e^3}{2\hbar^2} \sum_{n'} \frac{\langle g|r_i|n'\rangle\langle n'|r_j|n\rangle\langle n|r_k|g\rangle}{(\omega_0 - \omega_{n'g} + i\Gamma_{n'g})((\omega_{ng} - \omega_2 - i\Gamma_{ng})} =$$
$$\alpha^{(2)}_{NR} + \frac{e^3}{2\hbar^2} \sum_{n'} \frac{R_{ij}\mu_k}{(\omega_0 - \omega_{n'g} + i\Gamma_{n'g})(\omega_{ng} - \omega_2 - i\Gamma_{ng})}, \tag{A.6}$$

where $\alpha^{(2)}_{NR}$ refers to a frequency independent non-resonant contribution, $|g\rangle$ ($|n\rangle$) represents an electronic ground (vibrationally excited) state and Γ_{ng} ($\Gamma_{n'g}$) is the width of the transition from state $|n\rangle$ ($|n'\rangle$) to $|g\rangle$ The numerator in Eq. A.6 represents the product of the Raman tensor (R_{ij}) with the transition dipole moment (μ_k) of the vibrational mode. It holds the information regarding the symmetry of the molecule. When both the visible and sum frequency fields are off-resonance the expression simplifies to:

$$\alpha^{(2)}_{ijk}(\omega_0 = \omega_1 + \omega_2) = \frac{e^3}{2\hbar^2} \sum_{n'} \frac{R_{ij}\mu_k}{(\omega_{ng} - \omega_2 - i\Gamma_{ng})}, \tag{A.7}$$

which means that the vibrational modes that appear in the sum frequency spectrum are dictated by the simultaneous application of the selection rules for in-

frared and Raman spectroscopy. It also offers another way of explaining the absence of SFG signal for molecules with an inversion symmetry center: molecules that possess an inversion symmetry center are either infrared or Raman active, but can never be both at the same time [2].

To determine the orientation of a (stretched) alkyl chain we can use the symmetrical methyl stretch mode of the methyl (CH_3) end group. The amplitude of the mode for the different polarization combinations can be obtained from fits using Eq. A.2. The spectral shape of $\chi^{(2)}_{eff}$ is identical to that of $\alpha^{(2)}$. The measured amplitudes of $\chi^{(2)}_{eff,ppp}$, $\chi^{(2)}_{eff,ssp}$, $\chi^{(2)}_{eff,sps}$, $\chi^{(2)}_{eff,pss}$ can be related to the second-order surface susceptibility elements via Eqs. A.4. These elements can be related to the molecular hyperpolarizability elements uding Eqs. A.5 in combination with the symmetry properties of the symmetrical stretch vibration of the CH_3 group. The methyl group has C_{3v} symmetry and the symmetrical stretch mode has A_1 symmetry.

Table A.1: Character table of C_{3v} point group. It shows the the irreducible representations (first column), the components of the transition dipole moment and the Raman transition moment and the components of the hyperpolarizability tensor.

C_{3v}	E	$2C_3$	$3\sigma_v$			
A_1	1	1	1	c	$a^2 + b^2; c^2$	$\alpha^{(2)}_{ccc}, \alpha^{(2)}_{aac} = \alpha^{(2)}_{bbc}$
A_2	1	1	-1			
E	2	-1	0	(a,b)	(ab, bc) $(a^2 - b^2; ab)$	$\alpha^{(2)}_{aaa} = -\alpha^{(2)}_{bba} = -\alpha^{(2)}_{abb} = \alpha^{(2)}_{bab}$ $,\alpha^{(2)}_{caa} = \alpha^{(2)}_{cbb}, \alpha^{(2)}_{aca} = \alpha^{(2)}_{bcb}$

From inspection of the character table (see Table A.1), we find that there are only two independent components of the hyperpolarizability tensor. Assuming that the molecular distribution function is isotropic around the molecular axis [19, 21, 5], we can reduces Eqs. A.5 to a set of three equations:

$$\chi^{(2)}_{xxz} = \chi^{(2)}_{yyz} = \frac{1}{2}N_s\alpha[\langle\cos\theta\rangle(1+r) - \langle\cos^3\theta\rangle(1-r)] \qquad (A.8)$$

$$\chi^{(2)}_{zxx} = \chi^{(2)}_{zyy} = \chi^{(2)}_{xzx} = \chi^{(2)}_{yzy} = \frac{1}{2}N_s\alpha(\langle\cos\theta\rangle - \langle\cos^3\theta\rangle)(1-r) \qquad (A.9)$$

and

$$\chi^{(2)}_{zzz} = \frac{1}{2}N_s\alpha[r\langle\cos\theta\rangle + \langle\cos^3\theta\rangle(1-r)] \qquad (A.10)$$

Here, θ is the polar angle of the molecular axis c with respect to the lab frame axis z. The brackets again denote orientational averaging. In these expressions α is the element $\alpha^{(2)}_{ccc}$ and r is the hyperpolarzability ratio, $\alpha^{(2)}_{aac}/\alpha^{(2)}_{ccc}$. Assuming a distribution function for the angle θ we can find values for θ and r from spectral fits.

Bibliography

[1] N. W. Ashcroft and N. D. Mermin. *Solid state physics*. Saunders publishing, Philadelphia, 1976.

[2] P. W. Atkins. *Physical Chemistry*. Oxford University Press, Oxford, 1990.

[3] T. A. Delchar D. P. Woodruff. *Modern techniques of surface science*. Cambridge university press, Cambridge, 1990.

[4] G. A. Somorjai. *Chemistry in two dimensions: surfaces*. Cornell university press, New York, 1981.

[5] T. F. Heinz. *Nonlinear surface electromagnetic phenomena*, chapter 5. Elsevier, New York, 1991.

[6] X. D. Zhu, H. Suhr, and Y. R. Shen. *Phys. Rev. B.*, 35:3047, 1987.

[7] A. L. Harris, C. E. D. Chidsey, N. J. Levinos, and L. Dhar. *Chem. Phys. Lett.*, 141:350–356, 1987.

[8] J. H. Hunt, P. Guyot-Sionnest, and Y. R. Shen. *Chem. Phys. Lett.*, 133:189–192, 1987.

[9] P. Guyot-Sionnest, J. H. Hunt, and Y. R. Shen. *Phys. Rev. Lett.*, 59:1597, 1987.

[10] N. Watanabe, H. Yamamoto, A. Wada, K. Domen, C. Hirose, T. Ohtake, and N. Mino. *Spectrochim. Acta. A.*, 8-9:1529, 1994.

[11] C. D. Bain, P. B. Davies, T. H. Ong, R. N. Ward, and M. A. Brown. *Langmuir*, 7:1563–1566, 1991.

[12] T. H. Ong, P. B. Davies, and C. D. Bain. *Langmuir*, 9:1936, 1993.

[13] J. C. Owrutsky, J. P. Culver, M. Li, Y. R. Kim, M. J. Sarisky, M. S. Yeganeh, A. G. Yodh, and R. M. Hochstrasser. *J. Chem. Phys.*, 97:4421–4427, 1992.

[14] A. L. Harris, A. L. Rothberg, L. H. Dubois, N. J. Levinos, and L. Dhar. *Phys. Rev. Lett.*, 64:2086–2089, 1990.

[15] R. W. Boyd. *Nonlinear optics*. Academic Press, New York, 1992.

[16] Y. R. Shen. *The principles of nonlinear optics*. Wiley, New York, 1984.

[17] G. Ertl. *Faraday Discuss.*, 121:1, 2002.

[18] G. R. Bell, Z. X. Li, C. D. Bain, P. Fisher, and D. C. Duffy. *J. Phys. Chem. B*, 101:9461, 1998.

[19] E. W. M. van der Ham. *Sum frequency generation at interfaces: A study employing the FELIX free electron laser*. PhD thesis, Leiden University, Faculty of Mathematics and Natural Sciences, 1998.

[20] C. T. Williams, Y. Yang, and C. D. Bain. *Langmuir*, 16:2343, 2000.

[21] X. Zhuang, P. B. Miranda, D. Kim, and Y. R. Shen. *Phys. Rev. B.*, 59:12632, 1999.

[22] R. Kubo, M. Toda, and N. Hashitsume. *Statistical physics II*. Springer Verlag, Berlin, 1995.

[23] E. W. M. van der Ham, Q. H. F. Vrehen, and E. R. Eliel. *Surf. Sci.*, 386:96, 1996.

[24] L. J. Richter, T. P. Petralli-Mallow, and J. C. Stephenson. *Opt. Lett.*, 23:1594, 1998.

[25] T. Mii and H. Ueba. *Surf. Sci.*, 427:324, 1999.

[26] S. R. Hatch, R. S. Polizzotti, S. Dougal, and P. Rabinowitz. *Chem. Phys. Lett.*, 196:97–102, 1992.

[27] M. Bonn, D. N. Denzler, S. Funk, M. Wolf, S-S. Wellershof, and J. Hohlfeld. *Phys. Rev. B.*, 61:1101–1105, 2000.

[28] D. Star, T. Kikteva, and G. W. Leach. *J. Chem. Phys.*, 111:14, 1999.

[29] M. Saß, M. Lettenberger, and A. Lauberau. *Chem. Phys. Lett.*, 356:284–290, 2002.

[30] A. Le Rille, A. Tadjeddine, W. Q. Zheng, and A. Peremans. *Chem. Phys. Lett.*, 271:95, 1997.

[31] B. S. Mendoza, W. Luis Mochán, and J. A. Maytorena. *Phys. Rev. B.*, 60:14334–14340, 1999.

[32] J. Rudnick and E. A. Stern. *Phys. Rev. B.*, 4:4274–4290, 1971.

[33] A. V. Petukhov, V. L. Brudny, W. L. Mochán, J. A. Maytorena, B. S. Mendoza, and Th. Rasing. *Phys. Rev. Lett.*, 81:566, 1998.

[34] P. Guyot-Sionnest. *Phys. Rev. Lett.*, 66:1489–1492, 1991.

[35] M. van der Voort, C. W. Rella, A. F. G. van der Meer, A. V. Akimov, and J. I. Dijkhuis. *Phys. Rev. Lett.*, 84:1236–1239, 2000.

[36] G. Herzberg. *Molecular Spectra and Molecular Structure II*. D. van Nostrand company, Princeton, 1945.

[37] S. Baldelli, G. Mailhot, P. Ross, Y. R. Shen, and G. A. Somorjai. *J. Phys. Chem. B.*, 105:654, 2001.

[38] R. R Cavanagh, D. S. King, and J. C. Stephenson. *J. Phys. Chem.*, 97:786–798, 1993.

[39] H. L. Dai and W. Ho. *Laser spectroscopy and photochemistry on metal surfaces, Part II*. World Sceintific, Singapore, 1995.

[40] J. A. Prybyla, H. W. K. Tom, and G. D. Aumiller. *Phys. Rev. Lett.*, 68:503–507, 1992.

[41] M. Morin, N. J. Levinos, and A. L. Harris. *J. Chem. Phys.*, 96:3950, 1992.

[42] L. M. Struck, L. J. Richter, S. A. Buntin, R. C. Cavanagh, and J. C. Stephenson. *Phys. Rev. Lett.*, 77:4576–4579, 1996.

[43] A. Bandara, A. Kubota, K. Onda, A. Wada, S. S. Kano, K. Domen, and C. Hirose. *Surf. Sci.*, 427-428:331–336, 1999.

[44] M. Bonn, S. Funk, Ch. Hess, D. N. Denzler, C. Stampfl, M. Scheffler, M. Wolf, and G. Ertl. *Science*, 285:1042–1045, 1999.

[45] H. Petek, M. J. Weida, H. Nagano, and S. Ogawa. *Science*, 288:1402–1404, 2000.

[46] T. A. Germer, J. C. Stephenson, E. J. Heilweil, and R. R. Cavenagh. *J. Chem. Phys.*, 101:1704, 1994.

[47] C. Springer and M. Head-Gordon. *Chem. Phys.*, 205:73–89, 1996.

[48] P. Dumas, M. K. Weldon, Y. J. Chabal, and G. P. Williams. *Surf. Rev.*, 6:225–255, 1999.

[49] Y. R. Shen. *Nature*, 337:519, 1989.

[50] K. Domen, A. Bandara, J. Kubota, K. Onda, A. Wada, S. S. Kano, and C. Hirose. *Surf. Sci.*, 427-428:349–357, 1999.

[51] M. Bonn, Ch. Hess, S. Funk, J. H. Miners, B. N. J. Persson, M. Wolf, and G. Ertl. *Phys. Rev. Lett.*, 84:4653–4656, 2000.

[52] P. Jakob and B. N. J. Persson. *Phys. Rev. B.*, 56:10644, 1997.

[53] M. Bonn, Ch. Hess, J. H. Miners, T. F. Heinz, H. J. Bakker, and M. Cho. *Phys. Rev. Lett.*, 86:1566–1569, 2001.

[54] Ch. Hess, M. Wolf, S. Roke, and M. Bonn. *Surf. Sci.*, 502-503:304–312, 2002.

[55] D. G. Busch, S. Gao, R. A. Pelak, M. F. Booth, and W. Ho. *Phys. Rev. Lett.*, 75:673–676, 1995.

[56] C. J. Zhang, P. Hu, and A. Alavi. *J. Chem. Phys.*, 212:10564–10570, 2000.

[57] V. M. Kaganer, H. Möwald, and P. Dutta. *Rev. Mod. Phys.*, 71:779, 1999.

[58] C. W. McConlogue and T. K. Vanderlick. *Langmuir*, 13:7158, 1997.

[59] S. A. Kane, M. Compton, and N. Wilder. *Langmuir,* 16:8447, 2000.

[60] J. S. Salafsky and K. B. Eisenthal. *Chem. Phys. Lett.*, 319:435, 2000.

[61] J. C. Conboy, R. A. Walker, and G. L. Richmond. *Langmuir*, 13:3070, 1997.

[62] J. L. Löbau, M. Saß, W. Pohle, C. Selle, M. H. J. Koch, and K. Wolfrum. *J. Mol. Struct.*, 480-481:407, 1999.

[63] T. Petralli-Mallow, K. A. Briggman, L. J. Richter, J. C. Stephenson, and A. L. Plant. *Proc. SPIE*, 25:3859, 1999.

[64] P. Y. Bruise. *Organic Chemistry*. Prentice Hall, New Jersey, 1998.

[65] P. B. Miranda, V. Pflumnio, H. Saijo, and Y. R. Shen. *J. Am. Chem. Soc.*, 120:12092, 1998.

[66] D. Zhang, J. Gutow, and K. B. Eisenthal. *J. Phys. Chem.*, 98:13729, 1994.

[67] Y. R. Shen, M. W. Kim, Th. Rasing, T. Stehlin, and P Valint. *J. Chem. Phys.*, 89:3386, 1988.

[68] A. J. Meixner, Th. Enderle, and I. Zschokke-Gränacher. *J. Chem. Phys.*, 101:4365, 1994.

[69] T. Manaka, A. Tojima, and M. Iwamoto. *J. Chem. Phys.*, 115:9010, 2001.

[70] G. R. Bell, C. D. Bain, and R. N. Ward. *J. Chem. Soc. Farady*, 92:515, 1996.

[71] G. A. Reider and T. F. Heinz. *Photonic probes of surfaces*, chapter 9. Elsevier, Amsterdam, 1995.

[72] R. A. Walker, J. A. Gruetzmacher, and G. L. Richmond. *J. Am. Chem. Soc.*, 120:6991, 1998.

[73] E. C. Y. Yan and K. B. Eisenthal. *J. Phys. Chem. B.*, 103:6056, 1999.

[74] S. Roke, J. M. Schins, M. Müller, and M. Bonn. *Phys. Rev. Lett.*, 90:128101, 2003.

[75] N. Yang, W. E. Angerer, and A. G. Yodh. *Phys. Rev. Lett.*, 87:103902, 2001.

[76] J. Martorell, R. Vilaseca, and R. Corbalán. *Phys. Rev. A.*, 55:4520, 1997.

[77] J. I. Dadap, J. Shan, K. B. Eisenthal, and T. F. Heinz. *Phys. Rev. Lett.*, 83:4045, 1999.

[78] G. Ma and H. C. Allen. *J. Am. Chem. Soc.*, 124:9374, 2001.

[79] T. Kawai, D. J. Neivandt, and P. B. Davies. *J. Am. Chem. Soc.*, 112:12031–12032, 2000.

[80] T. S. Koffas, J. Kim, C. C. Lawrence, and G. A. Somorjai. *Langmuir*, 19:3563–3566, 2003.

[81] A. K. van Helden, J. W. Jansen, and A. Vrij. *J. Colloid Interface Sci.*, 81:354, 1981.

[82] W. Stöber, A. Vink, and R. Bohn. *J. Colloid Interface Sci.*, 26:62, 1968.

[83] H. C. van de Hulst. *Light scattering by small particles*. John Wiley and sons, New York, 1957.

[84] W. Brown. *Light scattering, principles and development*. Clarendon press, Oxford, 1996.

[85] D. E. Gray. *American Institute of Physics Handbook*. McGraw-Hill, New York, 1982.

[86] H. Goldstein, C. Poole, and J. Safko. *Classical Mechanics*. Addison Wesley, New York, 2001.

[87] J. I. Dadap, J. Shan, and T. F. Heinz. *J. Opt. Soc. Am. B*, 2004.

[88] J. P. Dewitz, J. P. Hübner, and K. H. Bennemann. *Z. Phys. D.*, 37:75–84, 1996.

[89] X. Ming Hua and J. I. Gersten. *Phys. Rev. B.*, 33:3756, 1986.

[90] C. K. Chen, T. F. Heinz, D. Ricard, and Y. R. Shen. *Phys. Rev. B.*, 27:1965, 1983.

[91] Y. Jiang, P. T. Wilson, M. C. Downer, C. W. White, and S. P. Withrow. *App. Phys. Lett.*, 78:766–768, 2001.

[92] W. L. Mochán, J. A. Maytorena, B. S. Mendoza, and V. L. Brudny. *Phys. Rev. B.*, 68:085318, 2003.

[93] J. D. Jackson. *Classical electrodynamics*. Wiley, New York, 1975.

[94] L. D. Landau and E. M. Lifshitz. *Electrodynamics of continuous media*. Pergamon press, Oxford, 1960.

[95] V. N. Gridnev. *Phys. Rev. B.*, 51:13079, 1995.

[96] A. L. Shelankov and G. E. Pikus. *Phys. Rev. B.*, 46:3326, 1992.

[97] V. N. Gridnev. *Solid State Commun.*, 100:71–75, 1996.

[98] K. Sato, A. Kodama, M. Miyamoto, A. V. Petukhov, K. Takanashi, S. Mitani, H. Fujimori, A. Kirilyuk, and Th. Rasing. *Phys. Rev. B*, 64:184427, 2001.

[99] A. V. Petukhov. *Phys. Rev. B.*, 52:16901, 1995.

[100] D. Deirmandjian. *Ann. Geophys*, 13:286, 1957.

[101] Ch. Kittel. *Introduction to solid state physics*. John Wiley and sons, New York, 1996.

[102] A. V. Petukhov, D. G. A. L. Aarts, I. P. Dolbnya, E. H. A. de Hoog, K. Kassapidou, G. J. Vroege, W. Bras, and H. N. W. Lekkerkerker. *Phys. Rev. Lett.*, 88:208301, 2002.

[103] M. M. Baksh, M. Jaros, and J. T. Groves. *Nature*, 427:139–141, 2004.

[104] V. J. Anderson and H. N. W. Lekkerkerker. *Nature*, 416:811–815, 2002.

[105] T. A. Taton, C. A. Mirkin, and R. L. Letsinger. *Science*, 289:1757, 2000.

[106] D. B. Lakutski and D. Frenkel. *Phys. Rev. Lett.*, 92:068302, 2004.

[107] D. Frenkel. *Physica A*, 313:1–31, 2002.

[108] J. W. Jansen. *Attractive interactions in sterically stabilized silica dispersions*. PhD thesis, Utrecht University, 1986.

[109] C. G. de Kruif, P. W. Rouw, W. J. Briels, M. H. G. Duits, A. Vrij, and R. P. May. *Langmuir*, 5:422–428, 1989.

[110] P. W. Rouw and C. G. de Kruif. *Phys. Rev. A.*, 39:5399–5408, 1989.

[111] P. W. Rouw, A. Vrij, and C. G. de Kruif. *Colloid Surface*, 31:299–309, 1988.

[112] T. Nicolai, C. Urban, and P. Schurtenberger. *J. Colloid Interface Sci.*, 240:419, 2001.

[113] M. Lattuada, H. Wu, and M. Morbidelli. *Langmuir*, 20:4355–4362, 2004.

[114] J. W. Jansen, C. G. de Kruif, and A. Vrij. *Chem. Phys. Lett.*, 107:450–453, 1984.

[115] A. Vrij, M. H. G. M. Penders, P. W. Rouw, C. G. de Kruif, J. K. G. Dhont, C. Smits, and H. N. W. Lekkerkerker. *Faraday Discuss.*, 90:31–40, 1990.

[116] S. Roke, W. G. Roeterdink, J. E. G. J. Wijnhoven, A. V. Petukhov, A. W. Kleyn, and M. Bonn. *Phys. Rev. Lett.*, 91:258302, 2003.

[117] S. Roke, M. Bonn, and A. V. Petukhov. *to be published in Phys. Rev. B.*, 2004.

[118] J. Buitenhuis. Warmtemetingen aan overgangen in stearylsilica dispersies. Master's thesis, Utrecht University, 1990.

[119] D. L. Dorset, H. L. Strauss, and R. G. Snyder. *J. Phys. Chem.*, 95:938, 1991.

[120] S. Ye, H. Noda, S. Morita, K. Uosaki, and M. Osawa. *Langmuir*, 19:2238–2242, 2003.

[121] M. Himmelhaus, F. Eisert, M. Buck, and M. Grunze. *J. Phys. Chem. B*, 104:577, 2000.

[122] J. W. Jansen, C. G. de Kruif, and A. Vrij. *J. Colloid Interface Sci.*, 114:481–491, 1986.

[123] E. Sirota, H. E. King Jr., G. J. Hughes, and W. K. Wan. *Phys. Rev. Lett.*, 104:492, 1992.

[124] G. A. Sefler, Q. Du, P. B. Miranda, and Y. R. Shen. *Chem. Phys. Lett.*, 235:347–354, 1995.

[125] B. M. Ocko, X. Z. Wu, E. B. Sirota, S. K. Sinha, O. Gang, and M. Deutsch 6. *Phys. Rev. E.*, 55:3164, 1997.

[126] M. S. Yeganeh. *Phys. Rev. E.*, 66:041607, 2002.

[127] E. Sloutskin, X. Z. Wu, T. B. Peterson, O. Gang, B. M. Ocko, E. B. Sirota, and M. Deutsch. *Phys. Rev. E.*, 68:031605, 2003.

Summary and outlook

Summary

In this thesis, vibrational femtosecond sum frequency generation is used to study structure and dynamics at interfaces. In the first part (Chapters 1-5) of this thesis the already well-explored reflection mode is used to study structure and dynamics with increasing complexity. In the last part (Chapters 6-8) a new type of vibrational femtosecond sum frequency generation, sum frequency scattering, is developed and used to investigate the interface of colloidal particles.

In Chapter 3, both time- and frequency-domain femtosecond sum frequency generation are used to study the C-H and C-N vibrational modes of acetonitrile (CH_3CN) molecules at the solid-liquid interface between acetonitrile and gold. Acetonitrile is adsorbed on the gold surface with the N atom towards the interface. Due to the surface roughness there are a variety of adsorption sites, leading to an inhomogeneous distribution of vibrational frequencies of the C-N stretch vibration of different molecules. This is observed very clearly in the time-domain SFG measurements, which display non-exponential decay and cannot be described with a homogeneous line broadening scenario. The frequency-domain measurements are much less sensitive to the inhomogeneity. This is somewhat surprising since in both measurement schemes the same material polarization is detected. An analysis is presented that describes both measurements simultaneously and demonstrates the partial inhomogeneous character of the C-N stretch vibration. In contrast to the C-N stretching mode, the C-H stretching modes are unaffected by the surface and display homogeneous line broadening in both the time- and frequency domain sum frequency measurements.

Chapter 4 deals with an investigation into femtosecond time-resolved vibrational sum frequency spectroscopy as a tool for studying ultrafast surface dynamics. By analyzing the visible pump-SFG probe experiments of CO on Ru(001), it is demonstrated that the presence of new spectral features does not necessarily mean that a novel (transient) chemical species has appeared on the surface. In these pump-SFG probe experiments the pump pulse modifies the vibrational response of the molecules, leading to a perturbed free induction decay of the infrared polarization. As a result, the emitted sum frequency field can display tran-

sient line shifts, even at negative delay times. The modified vibrational response is used to calculate SFG spectra. Also, the influence of the dephasing time on the apparent time resolution in these experiments is examined. Finally, a chemical reaction that takes place on the surface via a transition state (or reaction intermediate) is modeled with the aim of calculating the sum frequency intensity as a function of pump-probe delay time. These calculations show that a transition state can indeed be observed using pump-probe sum frequency generation and that its lifetime can be determined if the surface-adsorbate coupling is sufficiently fast (i.e. electron mediated).

In Chapter 5, frequency domain sum frequency generation is used in combination with fluorescence microscopy to study the behavior of phospholipid molecules (DPPC) on top of a water surface. At very high phospholipid density an ordered layer exists in which all the alkyl chains are fully stretched and oriented along the surface normal. This results in SFG spectra that are dominated by the methyl (CH_3) stretch vibrational modes. As a consequence of the local inversion symmetry around methylene (CH_2) groups, the methylene (CH_2) stretch modes are absent in the SFG spectra. With decreasing density the ordered layer breaks up into islands of high density that coexist with a low density phase. This is accompanied by a loss of local inversion symmetry and results in SFG spectra that are no longer dominated by the methyl (CH_3) stretch modes. This coexistence region exists over a range of densities and eventually transforms into the low density-liquid expanded phase. In the SFG spectra a rapid loss of intensity of the CH_3 peaks is observed, whereas the intensity of the CH_2 peaks remains constant over the entire coexistence region. The transition in the coexistence region can be modeled by calculating the density-dependent SFG intensity with a Monte Carlo model. The model indicates that an average of only four defects per chain are sufficient to reproduce the observed changes in the SFG signal.

At even lower densities, when the layer is in the liquid expanded phase, the SFG signal disappears completely. This disappearance of SFG signal is reversible and occurs over a very short range of densities. This indicates that there is a very sharp transition from a phase with spatially extended chains (the liquid expanded phase) to a new phase composed of coiled alkyl chains.

The last part of this thesis is devoted to the development and application of sum frequency generation scattering, which lifts the restriction of having to study flat interfaces. In Chapter 6, first experimental results are presented of vibrational sum frequency scattering from a suspension of sub-micron sized spherical colloidal particles. The Rayleigh-Gans-Debye scattering theory is extended from the linear scattering regime to the second-order scattering regime to extract the local molecular response from the macroscopic nonlinearly scattered spectral intensity. These results demonstrate the use of vibrational SFG to quantitatively investigate the surface molecular properties of sub-micron particles of varying sizes, dispersed in solution. Sum frequency generation scattering provides information on the order and density of alkyl chains and allows us to determine the elements of the local second-order surface susceptibility.

In Chapter 7, a more profound understanding of nonlinear optical scattering is obtained by developing a general theoretical method for deriving effective susceptibilities for nonlinear optical scattering processes of arbitrary order using the reciprocity principle. This method allows one to formulate a generalized treatment of nonlinear optical scattering and deduce selection rules independent of the precise mechanism of light-matter interaction. This approach is particularized to second-order sum frequency scattering from an inhomogeneous medium. The limiting cases of small particle scattering, refractive index matched RGD (Rayleigh-Gans-Debye) scattering, small refractive index contrast WKB (Wentzel-Kramers-Brillouin) scattering and correlated scattering are considered. Also, the RGD and WKB approximations are compared. For index contrasts of ~ 0.1 the RGD approximation suffices up to particle radii of ~ 1 μm. For larger radii the more exact WKB approximation needs to be used.

Finally, in Chapter 8 vibrational sum frequency scattering is used to study the phase behavior of a colloidal dispersion at the molecular level. The RGD scattering theory is expanded to selectively monitor the order and orientation of the molecular stearyl ($C_{18}H_{37}$) groups that terminate the surfaces of the sub-micron sized silica colloids dispersed in hexadecane. In the highly viscous gel state, at low temperatures, the alkyl chains are very well ordered and oriented. In contrast, in the low viscosity suspension at higher temperatures, the surface molecules are disordered. By combining temperature dependent SFG spectra with turbidity and calorimetric measurements, direct evidence is obtained that the surface-solvent interactions play a key role in the transition from a gel phase to a suspension. The molecular nature of gel aging is also investigated. Ordering occurs over time periods ranging from minutes to days. This ordering starts at the surface of the colloid and works its way outward along the alkyl chain.

Outlook

It is the goal of this thesis to demonstrate the use of sum frequency generation to study hidden interfaces of increasing complexity. Apart from achieving this goal by gaining new insights in how the molecules behave at these interfaces, new understanding of the technique of sum frequency generation has been obtained, both in a practical and in a theoretical sense. The work described in Chapter 3 will make it easier in the future to draw conclusions on the distribution of adsorption sites. It is also manifest that a combination of time and frequency domain experiments are necessary to draw such conclusions.

It is clear that in future work pump-SFG probe experiments can be used to investigate transition states at surfaces. The study of the phase behavior of phospholipids illustrates the potential of SFG to investigate order/disorder transitions on a molecular scale. It is recognized that it would be ideal and desirable if SFG could also be used to study the hidden interfaces of particles in solution. Subsequently, in Chapter 6 and 7 the technique of sum frequency scattering is developed

on both a theoretical and experimental level. In Chapter 8 it is demonstrated that new insights can be obtained on a molecular level on the phase transition in a colloidal dispersion. The development of sum frequency generation scattering together with an illustration of the potential of this new technique pave the way for in-situ investigations of the structure and dynamics of molecules at the interfaces of living cells, vesicles, and micelles.

Samenvatting

Nieuw licht op verborgen oppervlakken

In dit proefschrift wordt een nieuw licht geworpen op de structuur van en vibrationele dynamica aan verscheidene oppervlakken met behulp van breedbandige vibrationele somfrequentiegeneratie (SFG). In het eerste deel wordt deze techniek toegepast in de welbekende reflectie geometrie en wel op drie verschillende manieren: frequentieopgelost, tijdsopgelost en pomp-probe-somfrequentiegeneratie. In het laatste deel wordt de nog niet eerder toegepaste techniek van somfrequentieverstrooiing ontwikkeld en toegepast.

In hoofdstuk 3 wordt het verschil tussen tijds- en frequentiedomein somfrequentiegeneratie onderzocht door het adsorptiegedrag van acetonitril (CH_3CN) op een goudfilm te meten. Hoewel beide methodes volstrekt equivalent zouden moeten zijn (omdat in beide gevallen de polarisatie van het materiaal wordt gemeten), blijkt er toch een duidelijk verschil te zijn. De tijdsdomeinmetingen zijn namelijk veel gevoeliger zijn voor de omgeving van de vibratie dan de frequentiedomein metingen. Acetonitril is georiënteerd met de CN-groep naar het goud gericht. Deze nabijheid aan het ruwe goudoppervlak veroorzaakt de waargenomen inhomogeniteit in de CN-vibratie. De CH-vibratie wordt niet beïnvloed door het goudoppervlak en de opgezette infrarood-polarisatie vertoont dan ook exponentieel verval.

Pomp-probe-somfrequentiegeneratie is het onderwerp van hoofdstuk 4. In zulke pomp-probe-experimenten kan een somfrequentie-signaal bij andere frequenties dan de gebruikelijke vibratiefrequentie van het geadsorbeerde molecuul waargenomen worden. Door op numerieke wijze de pomp-SFG-probe-experimenten aan CO op Ru(001) na te bootsen, blijkt dat deze nieuwe frequenties niet horen bij nieuw gevormde chemische verbindingen. Ze zijn het gevolg van tijdelijke verschuivingen in de strekvibratiefrequentie van CO, die teweeg worden gebracht door koppeling van translatie- en rotatiebewegingen van de CO-moleculen met aangeslagen kristalroostertrillingen (fononen). Een analytisch model wordt ge-

119

bruikt om te kijken wat het effect van een veranderende vibrationele defaseringstijd, ten gevolge van de adsorbaat-oppervlak-koppeling, is op de SFG-spectra.

Hiernaast wordt gebruik gemaakt van een ander (maar vergelijkbaar) analytisch model om te onderzoeken of (en onder welke omstandigheden) het mogelijk is om overgangstoestanden van chemische reacties aan oppervlakken te aanschouwen met behulp van pomp-SFG-probe-metingen. Hieruit blijkt dat het mogelijk moet zijn om overgangstoestanden waar te nemen als de metaal-adsorbaat-koppeling voldoende snel is (dus verloopt via de elektronen en niet via de fononen) en het tijdsverschil tussen de zichtbare pomp en het SFG probe-paar kort is.

In hoofdstuk 5 wordt het gedrag van fosfolipiden (DPPC) in contact met water bestudeerd. Als de dichtheid van fosfolipiden hoog is, vormen de moleculen een geordende monolaag waarin de alkylstaarten georiënteerd zijn langs de oppervlaktenormaal. Dit wordt weerspiegeld in het SFG-spectrum door afwezigheid van de CH_2-strekvibraties. Bij afnemende dichtheid verandert de laag en ook het SFG-spectrum: Het signaal van de CH_3-strekvibraties neemt af, terwijl het signaal van de CH_2-strekvibraties constant blijft. Dit gedrag kan verklaard worden met een Monte Carlo-model waarmee het SFG-spectrum berekend kan worden als functie van de wanorde in de alkylketens.

Bij zeer lage dichtheden is er plotseling een concentratie waarbij het SFG-signaal verdwijnt. Deze (reversibele) verdwijning vindt plaats doordat er een fase gevormd wordt waarin gemiddeld inversie symmetrie bestaat. In deze nieuwe fase hebben de fosfolipiden hoogstwaarschijnlijk opgerolde alkylketens.

De vierde (in hoofdstuk 6 ontwikkelde) manier om somfrequentiegeneratie toe te passen is somfrequentieverstrooiing. In tegenstelling tot het genereren van een gereflecteerd somfrequentie-foton, biedt deze methode de mogelijkheid om gekromde oppervlakken in-situ te bestuderen. In hoofdstuk 6 worden de eerste somfrequentieverstrooiingsmetingen aan een suspensie van silicabolletjes behaard met alkylstaarten in CCl_4 gepresenteerd. Het verstrooiingspatroon kan theoretisch beschreven worden met een niet-lineair Rayleigh-Gans-Debye (RGD)-verstrooiings-model. Dit biedt eveneens de mogelijkheid om de lokale susceptibiliteit, de orde en oriëntatie van de alkylketens te bepalen.

Om een beter inzicht te krijgen in niet-lineaire verstrooiing wordt er in hoofdstuk 7 een algemene theorie ontwikkeld om (niet)-lineaire verstrooiing te beschrijven in termen van een effectieve susceptibiliteit van een willekeurig object. Deze theorie is gebaseerd op het reciprociteitsbeginsel en voorspelt de selectieregels voor verstrooiing ongeacht de licht-materie-interactie. Theoretische uitkomsten worden gegeven voor verstrooiing aan kleine deeltjes, verstrooiing in de RGD-benadering en verstrooiing aan een suspensie waarin het oplosmiddel en de deeltjes een klein verschil in brekingsindex hebben (Wentzel-Kramers-Brillouin (WKB)-benadering). Een vergelijking van de RGD- en de WKB-benadering levert op dat voor een brekingsindexcontrast van 0,1 de RGD-benadering sterk begint af te wijken van de meer exacte WKB-benadering.

Ten slotte, in hoofdstuk 8, wordt somfrequentieverstrooiing toegepast om de faseovergang in een colloïdale suspensie (bestaande uit behaarde silica deeltjes

in n-hexadecaan) op een moleculair niveau te bestuderen. Om de moleculaire oriëntatie te kunnen bepalen wordt de RGD-benadering uit hoofdstuk 6 verder ontwikkeld. In de zeer viskeuze gelfase zijn de alkylstaarten geordend. Deze orde zet zich een of meerdere lagen voort in het oplosmiddel. Bij verhitting van de gel ontstaat een suspensie waarin de oppervlakteketens zeer wanordelijk zijn en er geen netto attractie meer is tussen de deeltjes. De interactie tussen de oplosmiddelmoleculen en de oppervlaktemoleculen is cruciaal in de faseovergang. Dit wordt duidelijk aangetoond door SFG-metingen in combinatie met warmte- en turbiditeitsmetingen aan dispersies in verschillende oplosmiddelen. Ook blijkt dat gelvorming een traag proces is dat een paar dagen duurt. Bij het ouder worden van de gel ordent de oppervlaktelaag zich van binnenuit.

List of publications

This thesis is based on the following publications:

Chapter 3

S. Roke, A. W. Kleyn and M. Bonn, *Time vs. frequency domain femtosecond surface sum frequency generation*, Chem. Phys. Lett., 370, (2003), 227.

S. Roke, A. W. Kleyn and M. Bonn, *Femtosecond sum frequency generation at the metal-liquid interface*, submitted.

Chapter 4

S. Roke, A. W. Kleyn and M. Bonn, *Ultrafast surface dynamics studied with femtosecond sum frequency generation*, J. Phys. Chem. A. (Letter), 105, (2001), 1683.

Ch. Hess, M. Wolf, S. Roke and M. Bonn, *Femtosecond time-resolved vibrational SFG spectroscopy of CO/Ru(001)*, Surf. Sci., 502-503, (2002), 304.

Chapter 5

S. Roke, J. M. Schins, M. Müller and M. Bonn, *Vibrational spectroscopic investigation of the phase diagram of a biomimetic lipid monolayer*, Phys. Rev. Lett., 90, (2003), 128101.

J. M. Schins, S. Roke, M. Bonn and M. Müller, *Phase transitions in a lipid monolayer observed with vibrational sum-frequency generation*, Biophys. J., 84, (2003), 5A.

S. Roke, J. M. Schins, M. Müller and M. Bonn, *Order-disorder transition in phospholipid monolayers*, TRVS proceedings (2003).

Chapter 6

S. Roke, W. G. Roeterdink, J. E. G. J. Wijnhoven, A. V. Petukhov, A. W. Kleyn and M. Bonn, *Vibrational sum frequency Scattering from a sub-micron suspension*, Phys. Rev. Lett., 91, (2003), 258302.

Chapter 7

S. Roke, M. Bonn and A. V. Petukhov, *Nonlinear optical scattering: The concept of the effective suceptibility*, accepted for publication in Phys. Rev. B.

Chapter 8

S. Roke, A. van Blaaderen and M. Bonn *Molecular origin of a phase transition of colloids*, in preparation.

S. Roke, M. Bonn, A. van Blaaderen, *Surface-solvent interactions in a phase transition of colloids*, in preparation.

Other publications

S. Roke, J. M. Coquel and A. W. Kleyn, *The adsorption behaviour of isobutane on Pt(533): A combined RAIRS and TPD study* Chem. Phys. Lett. 323, (2000), 201.

S. Roke, J. M. Coquel and A. W. Kleyn, *Reorganization of adsorbed films by coadsorbing species*, J. Chem. Phys. 113, (2000), 6376.

A. P. Vink, M. A. de Bruin, S. Roke, and A. Meijerink, *Luminescence of exchange coupled pairs of transition metal ions*, J. Electrochem. Soc. 148, (2001), E313.

E. H. G. Backus, S. Roke, A. W Kleyn and M. Bonn, *Cascading second-order versus direct third-order nonlinear optical processes in a uniaxial crystal*, Opt. Commun. 234, (2004), 407.

Miscellaneous

S. Roke en M. Bonn, *Fosfolipiden buigen voor water*, NTvN, 69, (2003), 184.

Curriculum Vitae

Sylvie Roke was born in De Bilt on April 29, 1977. After obtaining her 'VWO diploma' at the "Athenaeum De Munnik" in Utrecht in 1995, she started studying Chemistry at Utrecht University. In 1996 she obtained the propedeuse (cum laude). In 1997 she started studying physics at Utrecht University for which the propedeuse was obtained in 1998. Two years later she obtained her Masters Degree in Physics (cum laude) and Chemistry (cum laude). During her studies she performed a short undergraduate research project in the group of Prof. dr. A. Meijerink at the Debye Institute (Utrecht University) on the topic of "Temperature dependent line-broadening experiments in spinel structures". Her main undergraduate research project was devoted to fundamental research on thin films under ultra-high vacuum conditions and performed at the FOM-Institute for Atomic- en Molecular Physics (AMOLF) in Amsterdam in the group of Prof. dr. A. W. Kleyn.

In the summer of 2000 she started her Ph. D. research (funded by the "projectruimte" of the FOM) in the group of Prof. dr. A. W. Kleyn and dr. M. Bonn. The results of that research are described in this thesis and have been presented at a number of international scientific conferences. She spent a few weeks in the group of Prof. dr. T. F. Heinz at Colombia University, New York and was awarded the L. J. Oosterhoff prize. Together with Cecile Corriol she organized the "Young Researchers school" that was held within the framework of the EU-TMR network in Les Houches, France. As a FOM employee she was a member of the personnel counsel (COR) for two years.

Nawoord

Het nawoord is een van de moeilijkste onderdelen van een proefschrift. Om inspiratie te krijgen voor het nawoord van dit proefschrift ben ik dus maar even op de SurfCat website gaan kijken. Hoewel de SurfCat-song je niet meer tegemoet komt bij de eerste klik geeft de site nog steeds een goede indruk van (onder andere) de sfeer in de groep. Er staan ook de namen van de groepsleden die in de afgelopen vier jaar voor een leuke werksfeer garant hebben gestaan: Aart, Mischa, Ellen, Euan, Wim, Michael, Emile, Otto, Mattijs, Jerôme, Kees-Jan, Rob, Johan, Mike, Andreea, Ben, Fujun, Meindert, Amalia, Ludo, Bernd, Heiner, Hella, Jacques, Dimitrios, Sonia.

De bijzondere SurfCat-sfeer werd onder andere gestimuleerd doordat we met een groot deel van de groep naar de TMR-workshops en Gordon conferenties zijn geweest. Memorabele gebeurtenissen waren voor mij het beruchte palingdiner tijdens de TMR-bijeenkomst in Oldenburg en het 'bergwandelingetje' in de White Mountains in New Hampshire. Ook de ski-avonturen in Les Houches zal ik niet snel vergeten.

De bijzondere wijze waarop gediscussieerd kon worden heb ik altijd erg gewaardeerd. Er blijken zeer directe manieren te bestaan om data en artikelen te bespreken.

Rob, jij stond altijd klaar om haastklussen te doen. Deze bestonden vaak uit het vermeubelen van eerder ontworpen onderdelen, zodat ze beter te gebruiken waren of om ze voor nieuwe experimenten in te zetten. Dit soort acties zijn altijd in strijd met jouw fijnmechanische gevoelens. Toch zijn ze voor mij erg belangrijk geweest en het heeft me een hoop tijd gescheeld. Dus bedankt! Maarten heeft ook een paar handige voorwerpen gemaakt voor de verstrooiingsmetingen. Ze waren erg bruikbaar. En dan is er natuurlijk Peter Schakel en het Peter Schakel-effect. Peter, de door jou ontworpen elektronica en software doet het altijd erg goed. Het Peter Schakel-effect bestaat eruit dat apparatuur het spontaan weer gaat doen zodra Peter binnenkomt. Het is een soort omgekeerd Pauli-effect. Frustrerend, maar toch prettig.

Wim, (Wimmie the beer commissioner) jij hebt van begin af aan de belangrijke taak van het organiseren van de groepsuitjes op je genomen. En je bent ook de enige persoon die ik ken die vaker dan ik een ongeluk heeft gehad zittend op een tweewieler. Euan 'Scotty' Hendry jij bent de web, Monty Python en voetbal-

goeroe (samen met Michael). Emile, het was leuk om na het werk te gaan eten en nog eens even op luchtige wijze de week door te nemen. Helaas konden we ons "cheapbastard"schap niet maximaal uitbuiten door op dezelfde dag te promoveren. Van Johan heb ik altijd zijn zeer directe manier van communiceren erg kunnen waarderen. Ellen, overbuurvrouw, ik heb genoten van de taart en de bieravondjes ("het moet op jongens") en gelukkig heb je ook een enorme puinhoop op je bureau. Mattijs, ook al ben je eigenlijk niet lang in Leiden geweest, je bijdrage aan het groepsmoraal is heel constructief geweest. Otto, ik vond het erg prettig dat je de tijd hebt genomen om mijn teksten te becommentariëren. Je bent een bevlogen wetenschapper met een zeer brede interesse.

For the fruitful collaborations I would like to thank Kristian Lass, Alexander Kros, Jie Shan, Tony Heinz, Michiel Müller, Juleon Schins, Sjors Wurpel, T. Pradeep and Martin Wolf. Van de mensen van de FCC uit Utrecht wil ik Henk, Judith en Andrei bedanken. Jullie zijn erg belangrijk geweest voor het laatste deel van dit proefschrift. Dankzij Henk en Judith kon ik samples gebruiken die ideaal waren voor het doen van de eerste verstrooiingsmetingen. Andrei, het was echt heel inspirerend om met jou samen te werken. Er zijn erg mooie dingen uit voortgekomen.

En dan is er, buiten de werksfeer, nog de invloed van Joke. Joke, ik ben blij dat ik van jou wijsheid, goede raad en vriendschap heb mogen genieten. Ik hoop dat we nog vaak zullen gaan fietsen. Mijn familie en vrienden wil ik bedanken voor de vriendschap, de steun, wanneer ik die nodig had, en voor de waardering die ik altijd heb genoten. Alex, jij hebt mij zoveel extra's gegeven het afgelopen jaar, dat had ik voor geen goud willen missen.
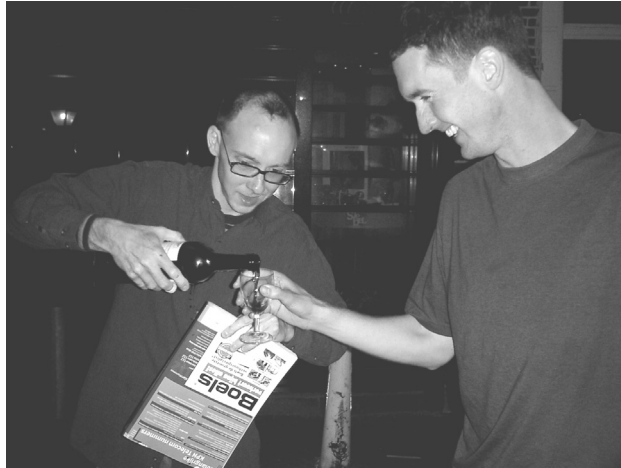
Fotogalerij

Figuur I: Kanoën tijdens een Gordon-conferentie.

Figuur II: Ellen op de ski's in Les Houches.

Figuur III: Otto heeft de fles wijn geopend gebruikmakend van een telefoonboek.

Figuur IV: De groep na een groepsuitje. We gingen wadlopen.

Figuur V: Mijn bureau. Een verborgen oppervlak.